

Copyright  
by  
Troy Christopher Messina  
2002

The Dissertation Committee for Troy Christopher Messina  
certifies that this is the approved version of the following dissertation:

**Steric Effects in the Metallic-Mirror to  
Transparent-Insulator Transition in  $\text{YH}_x$**

Committee:

---

John T. Markert, Supervisor

---

Alex de Lozanne

---

Ken Shih

---

Jack Swift

---

David Vanden Bout

**Steric Effects in the Metallic-Mirror to  
Transparent-Insulator Transition in  $\text{YH}_x$**

by

**Troy Christopher Messina, B.S., M.A.**

**DISSERTATION**

Presented to the Faculty of the Graduate School of

The University of Texas at Austin

in Partial Fulfillment

of the Requirements

for the Degree of

**DOCTOR OF PHILOSOPHY**

THE UNIVERSITY OF TEXAS AT AUSTIN

December 2002

dedicated to Mom, Dad, Todd, and Jodi, the wizards behind the curtain

## Acknowledgments

I would like to thank Dr. John Markert, an amazing scientist, an outstanding advisor and teacher, and a wonderful friend. I only wish I had known I could call him “John” sooner. I also must thank my coworkers because, at least most of them, made life in the lab enjoyable. I thank Michelle Chabot for the random way she ran her day-to-day life and her assistance with late night, last minute data collecting. Gergana Drandova gave me many inspiring conversations about culture, computers, and Metallica. Yong Lee seems to know something about everything which I have a question. Lizz Judge, if nothing else, knew EVERY completely obscure crossword answer. Casey Miller reminded me (twice) not to date physics students; fortunately, for Casey, the third time is the charm. Congratulations, stud!!! Also, without Casey, many of the results of this dissertation would not exist! Sean Rabun faithfully tested unused equipment to see what worked and what didn’t. Natalie Sidarous was always diligent in the lab even when everyone else chose to be social. Thanks to everyone in the de Lozanne and Erskine labs who gave me advice when I was lost. A special recognition goes to Alan Schroeder, Jesse Martinez, Harold Williams, John England, and all of the others on the 3rd floor of RLM that make things work. The University of Texas is so incredibly fortunate to have such a competent team. The last physics acknowledgement goes to Ronald Griessen and his team of researchers in Amsterdam, Holland for discovering the topic of my dissertation and assisting me during my tenure at UT. Their expert knowledge often shed light on very dark

situations.

Outside of physics... My closest friend and wife, Jodi, thank you for believing in me, having patience, and offering to spend the rest of your life with me. I have to “shout out” to the five greatest friends in the world, Tommy, Brian (B.J.), Bryan (NYC), Skaughtt, and dAVE. I wouldn’t have made it here without you guys. Next, thanks to my brother, Todd, a.k.a. Julian, who kept me clothed in hand-me-downs and protected me from bullies all my life. Next to last, thanks go to all of my musical compadres in Megalo, Chester, and 3 Penny Opera who have helped me continue my other passion.

This last acknowledgement deserves his own paragraph. One might find this humorous since my wife, family, and friends were lumped into a single paragraph. However, if it weren’t for Jack Clifford I would never have been able to build the experiments that brought me to the point of writing this dissertation. Jack’s assistance went far beyond a consultant in the machine shop. Jack is an incredible friend who I will miss dearly when I leave UT.

...

# Steric Effects in the Metallic-Mirror to Transparent-Insulator Transition in $\text{YH}_x$

Publication No. \_\_\_\_\_

Troy Christopher Messina, Ph.D.  
The University of Texas at Austin, 2002

Supervisor: John T. Markert

We have exploited the switchable mirror transition, from metallic mirror to transparent insulator, in  $\text{YH}_x$  to study steric effects due to scandium (Sc) substitution into the Y lattice. The reduction of lattice dimension upon Y replacement with Sc lends insight into the dynamics of this dramatic phase transition. Electron-beam evaporation was used to deposit 100 nm thick films of  $\text{Y}_{1-x}\text{Sc}_x$  alloys for  $0.00 \leq x \leq 1.00$ . The films are capped with a protective, 10 nm overlayer of palladium (Pd) to prevent oxidation and to catalyze hydrogen absorption. Despite a significant decrease in the unit cell volume of approximately 30%, optical spectral transmission and resistivity measurements reveal that a transition persists far into the alloy phase diagram. The optical transmittance behavior smoothly transitions from trihydride behavior to dihydride behavior with a total decrease in optical transmittance by a factor of 12. Electrical resistivity measurements indicate a similar reduction in the metal to insulator transition with Sc concentration. In addition, large disorder

of  $\rho_{do} \approx 120 \mu\Omega\cdot\text{cm}$  is introduced due to alloying. Details of structural analysis, spectroscopy, and electrical transport are discussed.



# Table of Contents

<b>Acknowledgments</b>	<b>v</b>
<b>Abstract</b>	<b>vii</b>
<b>List of Tables</b>	<b>xi</b>
<b>List of Figures</b>	<b>xii</b>
<b>Chapter 1. Introduction and Overview</b>	<b>1</b>
1.1 The Dawn of a New Experiment . . . . .	1
1.2 Switchable Mirrors . . . . .	3
1.3 Previous Work . . . . .	5
1.4 This Work . . . . .	8
<b>Chapter 2. Experimental</b>	<b>14</b>
2.1 Sample Preparation . . . . .	14
2.2 X-ray Diffraction . . . . .	19
2.3 Optical Spectroscopy . . . . .	20
2.4 AC Electrical Resistivity . . . . .	26
2.5 Block Diagrams . . . . .	30
<b>Chapter 3. Structural Analysis</b>	<b>34</b>
3.1 As-Deposited Films . . . . .	34
3.2 Dihydride Films . . . . .	37
<b>Chapter 4. Results and Analysis</b>	<b>40</b>
4.1 Introduction . . . . .	40
4.2 Optical Spectroscopy Results . . . . .	41
4.3 Electrical Resistivity . . . . .	54
4.3.1 Room Temperature Measurements . . . . .	54

4.3.2	Temperature-Dependent Measurements . . . . .	60
4.4	Discussion . . . . .	68
<b>Chapter 5.</b>	<b>Summary and Future Investigations</b>	<b>75</b>
<b>Appendices</b>		<b>77</b>
<b>Appendix A.</b>	<b>Vacuum and Film Deposition</b>	<b>78</b>
A.1	Growing a Film . . . . .	78
A.2	Some Suggested Modifications . . . . .	80
<b>Appendix B.</b>	<b>LabVIEW VIs</b>	<b>81</b>
B.1	Room Temperature VI . . . . .	81
B.2	Temperature Dependent VI . . . . .	84
<b>Appendix C.</b>	<b>Nuclear Magnetic Resonance Force Microscopy</b>	<b>92</b>
C.1	NMR–FM Overview . . . . .	92
C.2	Oscillators . . . . .	99
C.3	Micro–Magnets . . . . .	100
C.4	Magnet-on-Oscillator Characterization . . . . .	103
<b>Appendix D.</b>	<b>Some Pictures</b>	<b>107</b>
<b>Bibliography</b>		<b>113</b>
<b>Vita</b>		<b>126</b>

## List of Tables

4.1	Fit parameters from the Lambert-Beer model of the transmission edge for $\text{Y}_{1-z}\text{Sc}_z\text{H}_{3-\delta}$ . . . . .	55
C.1	Quality factors, spring constants, and minimal detectable forces for oscillators prior to magnet deposition. . . . .	99
C.2	Comparison of calculated and measured forces from micro-magnets on cantilevers. . . . .	105

## List of Figures

1.1	An optically switching yttrium film. Before hydrogen is introduced, the film reflects the American flag. After hydrogen has time to infuse, the film becomes visibly more transparent, and one can see objects behind the substrate (the longhorn). . . . .	2
1.2	Dissociation of H <sub>2</sub> at the surface of a metal film capped with Pd. . . . .	4
1.3	Hydrogen loading phenomena for a 100 nm Y film capped with 10 nm of Pd. On the left axis is the normalized transmittance at 700 nm. On the right axis is the resistivity. The scale at the bottom gives approximately the YH <sub>x</sub> phases corresponding to the graphical data. The arbitrary timescale is roughly in seconds. . . . .	5
1.4	Hydride structure and phase diagram for Y. There are three distinct phases: α (hcp monohydride), β (fcc dihydride), and γ (hcp trihydride). . . . .	7
1.5	Hexagonal lattice with corresponding tetrahedral (a) and octahedral (b) sites. . . . .	9
1.6	Face-centered cubic lattice with corresponding tetrahedral (a) and octahedral (b) sites. . . . .	10
1.7	Hydride structure and phase diagram for Sc. There are two distinct phases: α (fcc monohydride) and β (fcc dihydride). . . . .	12
1.8	Phase diagram for the Y <sub>1-z</sub> Sc <sub>z</sub> alloy system. The diagram indicates a solid solution is possible of all alloys of Y-Sc. . . . .	13
2.1	Vacuum chamber used for metal-hydride film growth: 1a-b) Leybold crystal growth monitors, 2) rotating substrate/shutter feedthrough, 3-4) e-beam evaporators, 5) leak valve, 6) e-beam evaporator power supply, 7) turbo and roughing pump station, 8) substrate viewport. . . . .	16
2.2	Pendant-drop electron beam evaporator. The rectangular section on the left image is blown up in the image on the right. 1) Sample rod, 2) filament, 3) linear-motion sample manipulator, 4) external electrical connections. . . . .	17
2.3	Diagram for Bragg scattering and diffraction of x-rays from parallel layers of a material. The bolded lines identify the path difference of the two outgoing rays. . . . .	19
2.4	Bausch and Lomb Optical Spectrometer: (1) customized sample insert tube, (2) wavelength selector (340–960 nm), (3) switch box for in-line and van der Pauw resistivity, (4) film mounting apparatus for 4-point resistivity and simultaneous optical transmission measurements during hydrogen loading. . . . .	21

2.5	Schematic of the Bausch & Lomb Spectronic 20 rotating reflection grating.	22
2.6	White light incident on the blaze angle reflection grating is split into constituent colors, which one can select on the spectrometer based on the angle of the reflection grating. . . . .	23
2.7	Current-to-voltage circuit diagram for the photodiode measuring optical transmission in the Bausch and Lomb spectrometer. The graph shows a typical photodiode response as a function of incident wavelength. The solid line is the baseline due to dark current. . . . .	25
2.8	Contact configuration of the room temperature resistivity probe. . . . .	27
2.9	In-line 4-point contact geometry for ac resistivity measurements. The entire sample represents a 1–2 mm wide strip from a $1 \times 1 \text{ cm}^2$ film. In this configuration, $\rho = Rhw/l$ . . . . .	28
2.10	The van der Pauw technique for 4-contact ac resistivity measurements. . .	29
2.11	Sample mount for temperature-dependent in-line 4-contact resistivity measurements on films. . . . .	29
2.12	Block diagram of the room temperature optical spectroscopy and resistivity measurement system. Transmission spectroscopy (340–960 nm wavelengths) was measured simultaneously with electrical resistivity. Phototransmission induces a current in a photodiode, which was converted to voltage and measured with a Keithley 195 DMM. In-line 4-point resistivity was measured with an LR-400 ac resistance bridge. All measurements were recorded using Labview v.6. . . . .	31
2.13	Block diagram of the temperature dependent resistivity measurement system. In-line 4-point resistivity was measured with an LR-400 ac resistance bridge and output to a Keithley 195A DMM. Temperature was monitored with a calibrated RuO thermometer connected in a 4-contact geometry to a Keithley 195 DMM. All measurements are recorded using LabVIEW v.6.	32
3.1	Expected and measured x-ray diffraction patterns for the as-deposited films.	35
3.2	Unit cell lattice parameters, $a$ and $c$ , as a function of Sc concentration, $z$ , for the hcp as-deposited films. The trend is nearly linear, as expected, with some deviations due to hydrogen incorporation during film growth and small grain size. . . . .	37
3.3	Expected and measured x-ray diffraction patterns for the dihydride concentration films. . . . .	38
3.4	Unit cell lattice parameter, $a$ , as a function of Sc concentration, $z$ , for the fcc dihydride films. . . . .	39
4.1	Optical transmittance spectra as a function of hydrogen loading time (in arbitrary units) starting from as-deposited films of Y and $\text{Y}_{0.90}\text{Sc}_{0.10}$ . The optical switching capability is approximately equivalent for both samples. The full loading time scale is typically 1–2 hours. . . . .	42

4.2	Optical transmittance spectra as a function of hydrogen loading time (in arbitrary units) starting from as-deposited films $Y_{0.80}Sc_{0.20}$ and Sc. The vertical axis is scaled to that of the $z = 0.00$ and $z = 0.10$ samples. The loss of optical switching capability is evident. The full loading time scale is typically 1–2 hours. . . . .	43
4.3	Optical transmittance as a function of hydrogen loading time (in arbitrary units) starting from unloaded ( $x \approx 2$ ) films of $YH_x$ and $Y_{0.90}Sc_{0.10}H_x$ . The full loading time scale is typically 1–2 hours. . . . .	45
4.4	Optical transmittance spectra as a function of hydrogen loading time (in arbitrary units) starting from unloaded films (near $x = 2$ ) of $Y_{0.80}Sc_{0.20}H_x$ and $ScH_x$ . The full loading time scale is typically 1–2 hours. . . . .	46
4.5	Optical transmittance spectra as a function of hydrogen loading time (in arbitrary units) starting from an as-deposited film of $Y_{0.60}Sc_{0.40}$ . This alloy exhibits phase separation upon hydrogenation. The spectrum, therefore, has a trihydride-like appearance with maximal transmittance at $\lambda = 960$ nm due to $YH_3$ formation. The full loading time scale is typically 1–2 hours. . . . .	47
4.6	Optical transmittance spectra as a function of hydrogen loading time (in arbitrary units) starting from as-deposited (top) and unloaded (bottom) films of $Y_{0.50}Sc_{0.50}H_x$ . The unloaded film is expected to have $x \approx 2$ . The full loading time scale is typically 1–2 hours. . . . .	48
4.7	Transmittance and ac resistivity as a function of hydrogen loading time. The loading time is arbitrary and has not been scaled in any way. The hydrogen loading time ranged from 10 minutes to 2 hours. The transmittance is plotted for the wavelength of maximum dihydride transmittance. Dihydride transmittance appears as a small peak or a shoulder on the transmittance curve and is indicated by the vertical arrows. . . . .	50
4.8	Transmittance at $\lambda = 820$ nm ( $\hbar\omega = 1.51$ eV) as a function of Sc concentration $z$ . The amount of transmittance for fully loaded films approaches that of unloaded films (near $x = 2$ ) with increasing $z$ indicating a loss of octahedral site occupancy for trihydride formation. The lines are shown to guide the eye. The scatter in the data may be due to atomic disorder effects or phase separation. . . . .	51
4.9	(a) Fully hydrogen loaded and (b) unloaded (near $x = 2$ ) film optical spectra showing transmittance maxima dependence on alloy composition. . . . .	52
4.10	Energy of maximum transmittance (for the range $1.29 \leq \hbar\omega \leq 3.65$ eV) as a function of Sc concentration, $z$ . The transparency energy of the fully loaded films approaches that of the unloaded films (near $x = 2$ ) as $z$ increases. The lines are shown to guide the eye. The scatter in the data may be due to atomic disorder effects. . . . .	53
4.11	Lambert-Beer fits to the transmission edge. . . . .	55

4.12	Room temperature resistivity of several alloys as a function of hydrogen loading time in arbitrary units. The data has been scaled so that the dihydride minimum is at the same time. The transition from the dihydride minimum to trihydride maximum reduces with concentration until, in scandium the resistivity stays in the dihydride minimum. . . . .	57
4.13	Modeling of disorder in room temperature electrical resistivity from Eqn. 4.1.	59
4.14	Temperature dependence of the ac resistivity for dihydrides of several alloys. All show metallic behavior with the exception of $Y_{0.90}Sc_{0.10}$ . . . . .	61
4.15	Temperature dependence of the ac resistivity for fully hydrogenated (295 K; 1 atm $H_2$ ) films of the same alloys as Fig. 4.14. $YH_{3-\delta}$ and $Y_{0.90}Sc_{0.10}H_{3-\delta}$ indicate insulating behavior at low temperatures with an up-turned resistivity. A transition occurs from $z = 0.10$ and $z = 0.20$ supporting the spectroscopy results. . . . .	62
4.16	Temperature dependence of the resistivity over the range 4–150 K. The top graph shows that, for 50–150 K, $YH_{3-\delta}$ is most linear when plotted as $\rho$ vs. $\ln(T)$ , while in the bottom plot, $Y_{0.90}Sc_{0.10}H_{3-\delta}$ and $Y_{0.80}Sc_{0.20}H_{2+\delta}$ show linear behavior only at lower temperatures (4–20 K) when plotted as $\ln(\rho)$ vs. $T^{-1/4}$ , indicating a variable range hopping model. . . . .	63
4.17	Temperature dependence of alloys with $z > 0.20$ . Qualitatively the data is similar for all alloys with $z \geq 0.20$ . The low temperature up-turn is best modeled with a Mott transition ( $T^{-1/4}$ ). . . . .	65
4.18	Scandium resistivity for 4–50 K. The data is plotted as $\rho \propto \ln(T)$ on top and $\ln(\rho) \propto T^{-1/4}$ on bottom. The best agreement is with the Mott model.	66
4.19	Films of $YH_{3-\delta}$ showing a temperature induced shunt and a hydrogen content induced shunt. These resistivities are calculated assuming a film thickness of 110 nm. The resistivity near 4 K is equivalent to that of palladium when calculated for a 10 nm film. . . . .	67
4.20	A plot of the fraction of octahedral sites that have $n$ scandium nearest neighbors as a function of scandium concentration. The dashed lines indicate the region where the metallic-mirror to transparent-insulator transition is largely quenched. . . . .	69
4.21	Expected maximum hydrogen content as calculated from data observations and the combinatorics of Fig. 4.20. . . . .	71
4.22	Revisiting the data of Fig. 4.8, the fully loaded transmittance as a function of scandium content has been fit in proportion to the hydrogen content predicted by restricting octahedral occupancy to sites with $n = 0$ or $n = 0$ and 1 nearest-neighbor scandiums. . . . .	72
4.23	Phase diagrams for the 3-element system with the maximal hydrogen contents calculated from the model discussed in the text. a) assumes $n = 0$ and b) $n = 0$ and 1. . . . .	73

B.1	Room temperature spectrometry and resistivity LabVIEW VI front panel.	82
B.2	The opening sequence of the room temperature VI. This sequence sets up the timer and opens a file with column headers for writing data. The time and file information are sent into a while loop that runs until the <i>stop</i> button is clicked. The while loop contains sequential frames which do all of the other operations.	83
B.3	The second frame of the room temperature VI. The values for resistance and transmittance voltages are formatted and converted to strings.	85
B.4	Final frame of the VI. The characters for the time, transmittance (GPIB 16 voltage) and resistance (GPIB 25 voltage) are written to the file.	86
B.5	Temperature dependent resistivity LabVIEW VI front panel.	87
B.6	A similar startup algorithm to initialize the time and start the file with column headers. This VI also opens thermometer calibration files and creates interpolation matrices to convert RuO resistance to a temperature.	88
B.7	The RuO resistance is interpolated, and the temperature and sample resistance are formatted and converted to strings.	89
B.8	This frame reads the two DMMs almost identical to the previous VI.	90
C.1	Nuclear Magnetic Resonance Force Microscope (NMRFM) schematic shown in the magnet-on-oscillator geometry.	93
C.2	Interferometry of a diode laser reflecting from a fiber optic cleave and a mechanical oscillator surface.	94
C.3	Fiber optic interferometry circuit developed by Tobias Graf and Michelle Chabot.	95
C.4	Contour plot of magnetic field gradient for a micron-sized magnet with 1 $\mu\text{m}$ diameter and 0.1 $\mu\text{m}$ thickness. The lines are drawn to indicate a 3 $\mu\text{m}$ distance from the magnet face where the field gradient for this magnet aspect ratio is 100 $\text{G}/\mu\text{m}$ , as desired.	97
C.5	Magnetic field gradient as a function of distance from the surface of a micron-sized magnet with 1 $\mu\text{m}$ diameter and 0.1 $\mu\text{m}$ thickness. The lines indicate that a distance of 3 $\mu\text{m}$ from the surface provides a field gradient of 100 $\text{G}/\mu\text{m}$ .	98
C.6	Ideal spatial relationship between magnetic field gradient contours and sample film being measured.	98
C.7	Commercial and micro-machined oscillators used for magnet characterization.	100
C.8	SEM image of Nanoprobe cantilever with an approximately $(30 \mu\text{m})^2$ magnet of 83 nm cobalt capped with 12 nm gold.	101
C.9	SEM image of Ultralever cantilever with a cobalt magnet 4 $\mu\text{m}$ in diameter, 60 nm thick capped with 8 nm of gold.	101



C.10 SEM image of Ultralever cantilever with a cobalt magnet a $2\ \mu\text{m}$ in diameter, 60 nm thick capped with 12 nm of gold. . . . .	102
C.11 Measurement of magnetic saturation perpendicular to the plane of a $0.06\ \mu\text{m}$ cobalt film. . . . .	103
C.12 NMR-FM probe modified with a coil around the optical fiber to measure micro-magnets on oscillators. . . . .	104
D.1 Troy speaking at the Metal Hydrides conference (MH2002) in Annecy, France.	108
D.2 Troy marrying Jodi at his parents' house in Rockwall, Texas, April 7, 2001.	109
D.3 Troy showing off his super-cool boron tattoo. . . . .	110
D.4 Troy bangin' the skins at Steamboat with former band Megalo. . . . .	111
D.5 Signature page for this dissertation. . . . .	112

# Chapter 1

## Introduction and Overview

*“When I was just a little bitty baby, my daddy sat me down on his knee, and he said to me, ‘Son, you’ve gotta work real hard; you’ve gotta work all day; you’ve gotta work those fingers right down to the bone’.”*

*- Don’t Even Hoig Around by Ten Hands*

### 1.1 The Dawn of a New Experiment

The title may be misleading. I do not intend to imply that experiments on metal-hydride systems or, more specifically, on switchable mirror systems is a new endeavor. However, the University of Texas is the first research institution in the United States to attempt to elucidate the physics behind the metallic-mirror to transparent-insulator transition that occurs in some rare-earth metals due to hydrogen absorption. In addition, this is the first dissertation to be completed on the topic here at UT. This being so, the research required development of many new experimental facilities including an ultra-high vacuum (UHV) film deposition chamber, thin film structure and transport characterization techniques, and optical spectroscopy. In light of the the novelty of these experiments on the local level, Chapter 2 is dedicated to describing these experiments.



Figure 1.1: An optically switching yttrium film. Before hydrogen is introduced, the film reflects the American flag. After hydrogen has time to infuse, the film becomes visibly more transparent, and one can see objects behind the substrate (the longhorn).

Studies of metal-hydride systems date back at least as far as 1866 when Graham discovered that palladium absorbs large amounts of hydrogen [1]. It was only a short time later that the utilities of hydrogen storage in metals were realized. For example, metals can be used for rechargeable batteries where hydrogen is reloaded into an electrode from a hydrogen-rich electrolyte. Similar applications already exist using lithium and hydrogen. Such batteries can be found in laptop computers and mobile telephones. Even Duracell has a patented metal-hydride technology! This technology has also found itself a home in the automotive industry as well. The “drive” for lower emissions has spotlighted hydrogen as a fuel source, however, it is necessary to store the hydrogen safely as well as densely. Metal-hydride systems provide both safety and a storage density greater than that of liquid hydrogen.

## 1.2 Switchable Mirrors

More in line with these studies, hydrogen is able to create an optical gap in some rare-earth metals such as yttrium and lanthanum. Reversible transitions between the metallic-mirror and optically transparent-insulator states are possible by changing the metal's hydrogen content over a small range. With such dramatic switching properties, it may be possible to create energy efficiency devices such as "smart windows" which act as a mirror to deflect sunlight or as a transparent window to allow natural lighting. These characteristics can be seen in the 100 nm yttrium film pictured in Fig. 1.1. Prior to exposure to hydrogen the film reflects an object in front of it (the American flag), and after exposure, one can see an object behind the substrate (the longhorn). The residual reflecting properties seen after hydrogenation are due mostly to the protective capping layer of palladium. The existence of this quick and reversible optical transition was discovered in yttrium and lanthanum in 1996 by the group of Ronald Griessen at the Vrije University of Amsterdam [2]. The discovery occurred while looking into dirty, atomic, metallic hydrogen in a high pressure diamond anvil cell at low temperatures. However, the earliest signs of this behavior were actually seen as early as 1977 in the accompanying metal-insulator transition and in band structure studies [52, 53, 48, 41]. Studies on bulk materials described the transition as one from shiny metal, at the dihydride phase ( $MH_2$ ;  $M = \text{metal}$ ), to a dark, unstable powder, in the trihydride ( $MH_3$ ) [17]. Due to this instability, combined with a lack of film growth capabilities, only more recent experiments on thin films have observed the drastic change in optical and electrical properties between these two states, simultaneously. Furthermore, the transition can

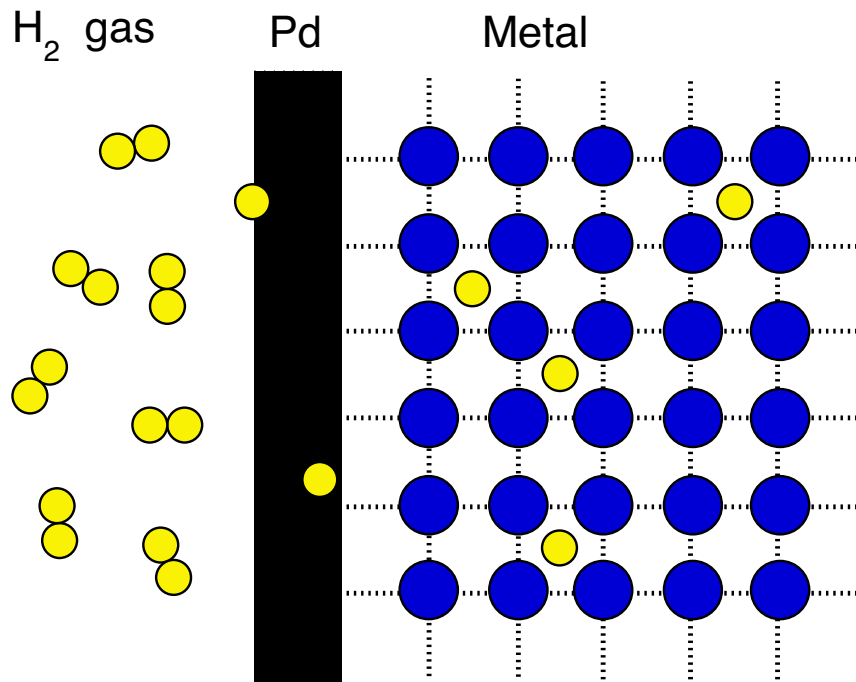


Figure 1.2: Dissociation of H<sub>2</sub> at the surface of a metal film capped with Pd.

occur at room temperature in one atmosphere of hydrogen ( $1.0 \times 10^5$  Pa), provided the film is protected from oxidation by a thin layer of palladium (Pd) [2]. In addition, palladium is found to enhance hydrogen absorption by assisting the dissociation of molecular hydrogen at the film interface. See Fig. 1.2 for a schematic of this process.

In Fig. 1.3 the various phases of  $\text{YH}_x$  can be seen based on changing optical and electrical behavior. The system has a solid-solution  $\alpha$ -phase ( $0.00 \leq x \leq 0.21$ ) where resistivity increases slightly due to an increase in scattering centers created by the hydrogen interstitials and the optical transmittance varies negligibly. Upon further hydrogenation, the system enters the dihydride  $\beta$ -phase ( $1.83 \leq x \leq 2.09$ ) where hydrogen forms a sublattice of tetrahedral interstices. In this phase, the re-

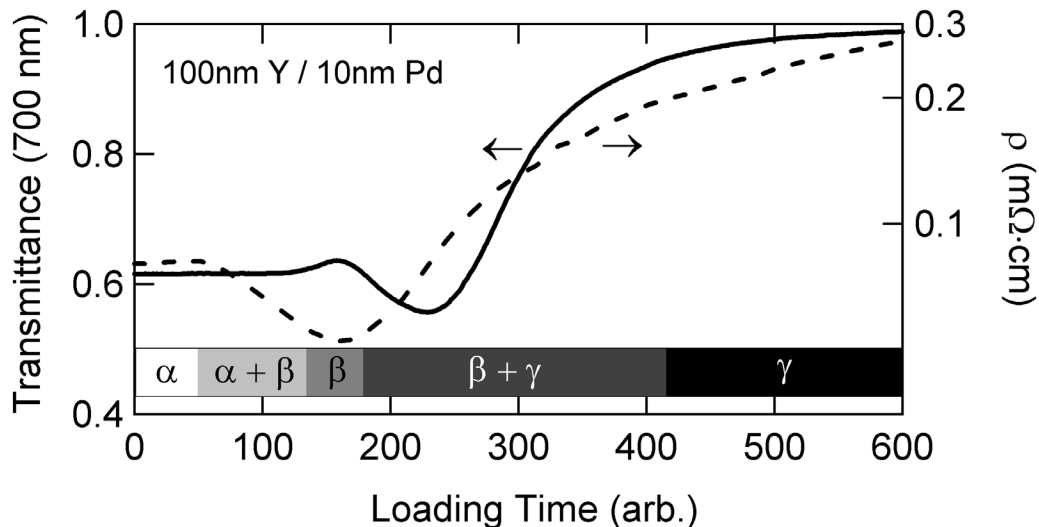


Figure 1.3: Hydrogen loading phenomena for a 100 nm Y film capped with 10 nm of Pd. On the left axis is the normalized transmittance at 700 nm. On the right axis is the resistivity. The scale at the bottom gives approximately the  $YH_x$  phases corresponding to the graphical data. The arbitrary timescale is roughly in seconds.

sistivity decreases and there is a small transmittance window near 700 nm. For  $x \geq 2.85$ , the system finally enters the trihydride  $\gamma$ -phase where both optical transmittance and resistivity increase dramatically. Between each pair of these three phases are coexistence regions of the adjoining phases. An approximate correspondence to the data for the phases is also shown in Fig. 1.3. The specifics of the different phases are discussed in more detail in section 1.3.

### 1.3 Previous Work

The rare-earth hydrides  $YH_x$ ,  $LaH_x$ , and their alloy system,  $La_{1-z}Y_zH_x$ , have been extensively studied by Griessen et al. at the Vrije University in Amsterdam [6, and references therein]. These systems attracted much interest because

of their inherent differences in structure throughout the hydride phase diagram. Yttrium, from its pure metal to its  $\alpha$ -phase ( $\text{YH}_1$ ) has a hexagonal (hcp) lattice structure. The  $\alpha$  phase finds H atoms distributed upon tetrahedral interstitial sites. Further hydrogenation reveals the  $\beta$ -phase ( $\text{YH}_2$ ) where the lattice becomes face-centered-cubic (fcc) and H atoms have nearly fully occupied the two tetrahedral sites per metal atom with some very small fractional filling of octahedral sites, although this is energetically much less favorable. Finally, in the trihydride  $\gamma$ -phase ( $\text{YH}_3$ ), the lattice returns to a hcp structure with a larger unit cell than the previous hcp structure. In this phase, the H atoms fill both the tetrahedral and the octahedral interstitial sites. Lanthanum, on the other hand, begins as an hcp structure and becomes fcc for the  $\beta$  and  $\gamma$  phases. As in yttrium, hydrogen atoms fill the same respective locations throughout the phase diagram. Figure 1.4 shows the metal-hydride phase diagram with lattice structure noted for each phase for yttrium [76]. The hcp and fcc lattice structures are shown in Figs. 1.5 and 1.6, respectively. The basis for tetrahedral (a) and octahedral (b) hydrogen atoms is indicated by the thick dashed lines.

In the  $\text{La}_{1-z}\text{Y}_z$  alloy system, the lattice behavior is similar to that of La for  $0 \leq z \leq 0.67$ , and like that of Y when  $z > 0.67$ . The switching time remains more or less constant throughout the La-Y system at about 10–40 seconds in the first loading. However, the switching time is  $5.0 \pm 3.1$  times shorter for the second and subsequent hydrogen loads probably due to pre-existing distortions in the lattice created by the irreversible  $\alpha$ - $\beta$  transition of the first loading. These results are interesting as they suggest that crystal structure plays very little role in the metallic-mirror to

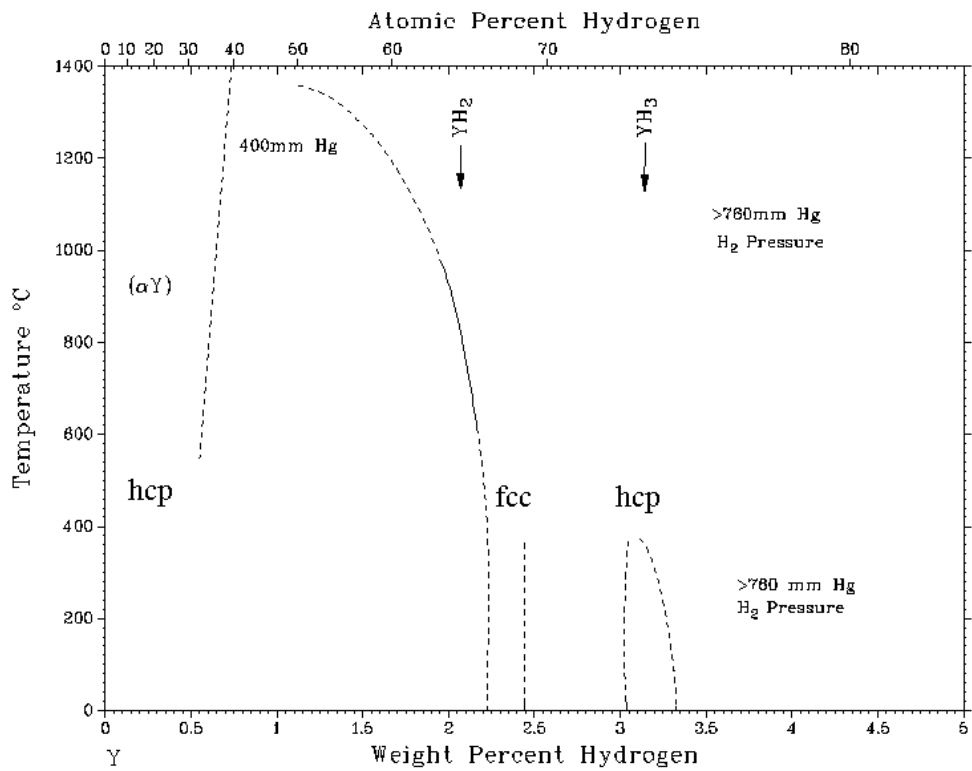


Figure 1.4: Hydride structure and phase diagram for Y. There are three distinct phases:  $\alpha$  (hcp monohydride),  $\beta$  (fcc dihydride), and  $\gamma$  (hcp trihydride).



transparent-insulator transition.

Theoretical calculations for  $\text{YH}_3$  and  $\text{LaH}_3$  predicted metallic behavior until as late as 1997. It was not until the optical switching was discovered that the differences between experiment and theory were taken seriously. In more recent explanations, theory has taken two paths. The first line of reasoning explains changes in band structure by small displacements of atoms. Ab initio, self-consistent, LDA calculations show that these small displacements from the  $\text{HoD}_3$  structure result in a lower energy and a small band gap due to band hybridization [21]. More recent total energy calculations using GW methods suggest a  $\text{HoD}_3$  structure with an optical gap of 3 eV agreeing with experiment [27]; however, these methods do not account for the ionic behavior of  $\text{YH}_3$  observed experimentally [28]. In the second theoretical approach, strong electron correlations on hydrogen sites have been considered within the LDA framework. Here, hydrogen is treated as  $\text{H}^-$  as observed experimentally. The correlated electrons tend to avoid one another which induces valence band narrowing and a gap between valence and conduction band [23].

#### 1.4 This Work

Because there is, as yet, so little understood about this phase transition, we have chosen to look further into the role of structure. By substituting scandium (Sc) into the yttrium lattice one can investigate the dependence of the transition on lattice dimensions. The smaller lattice of Sc allows a maximum of two H atoms per Sc atom as shown in Fig. 1.7 [76]. These phases extend to room temperature in thin films, and therefore, there is no octahedral filling. All rare-earth metals which

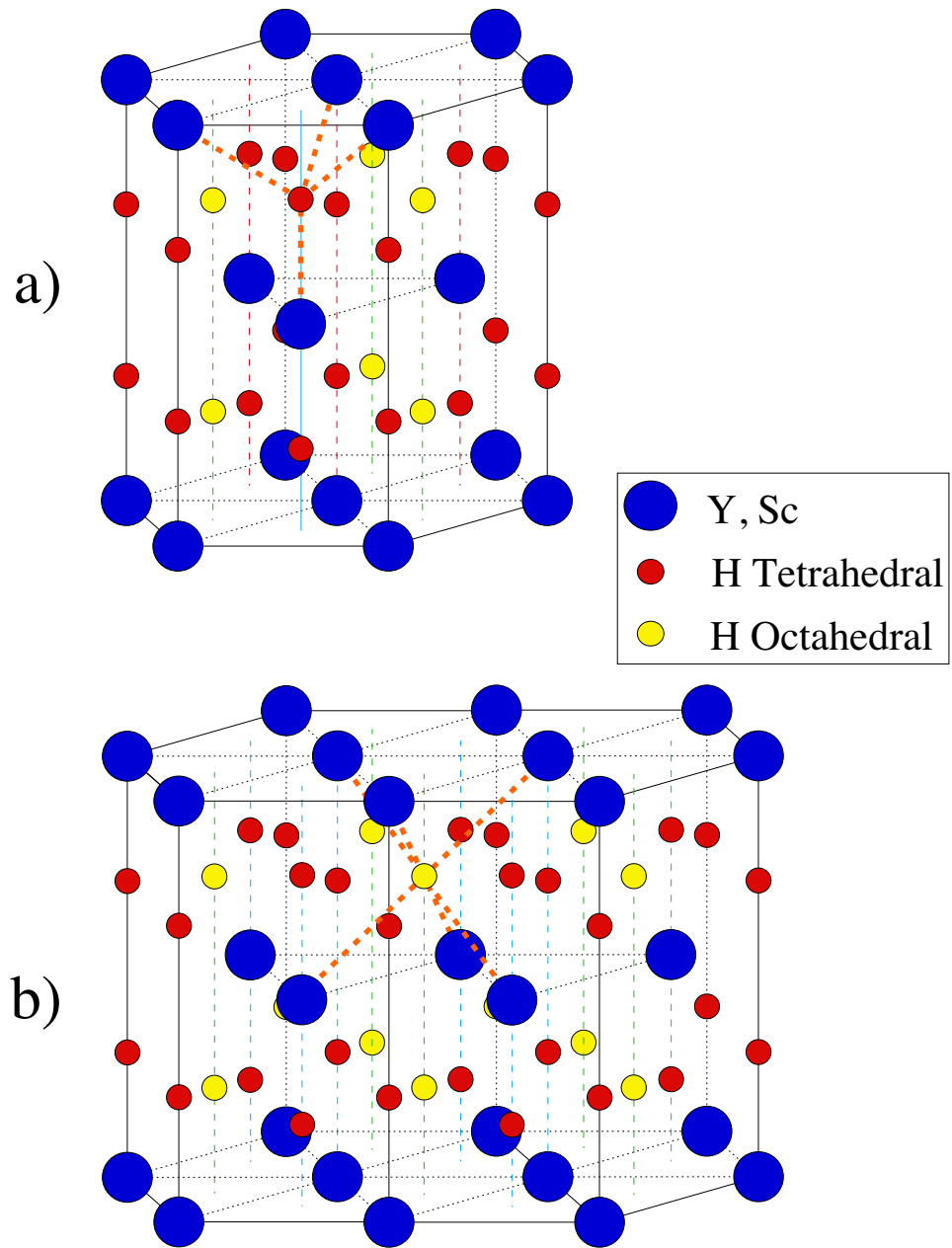


Figure 1.5: Hexagonal lattice with corresponding tetrahedral (a) and octahedral (b) sites.

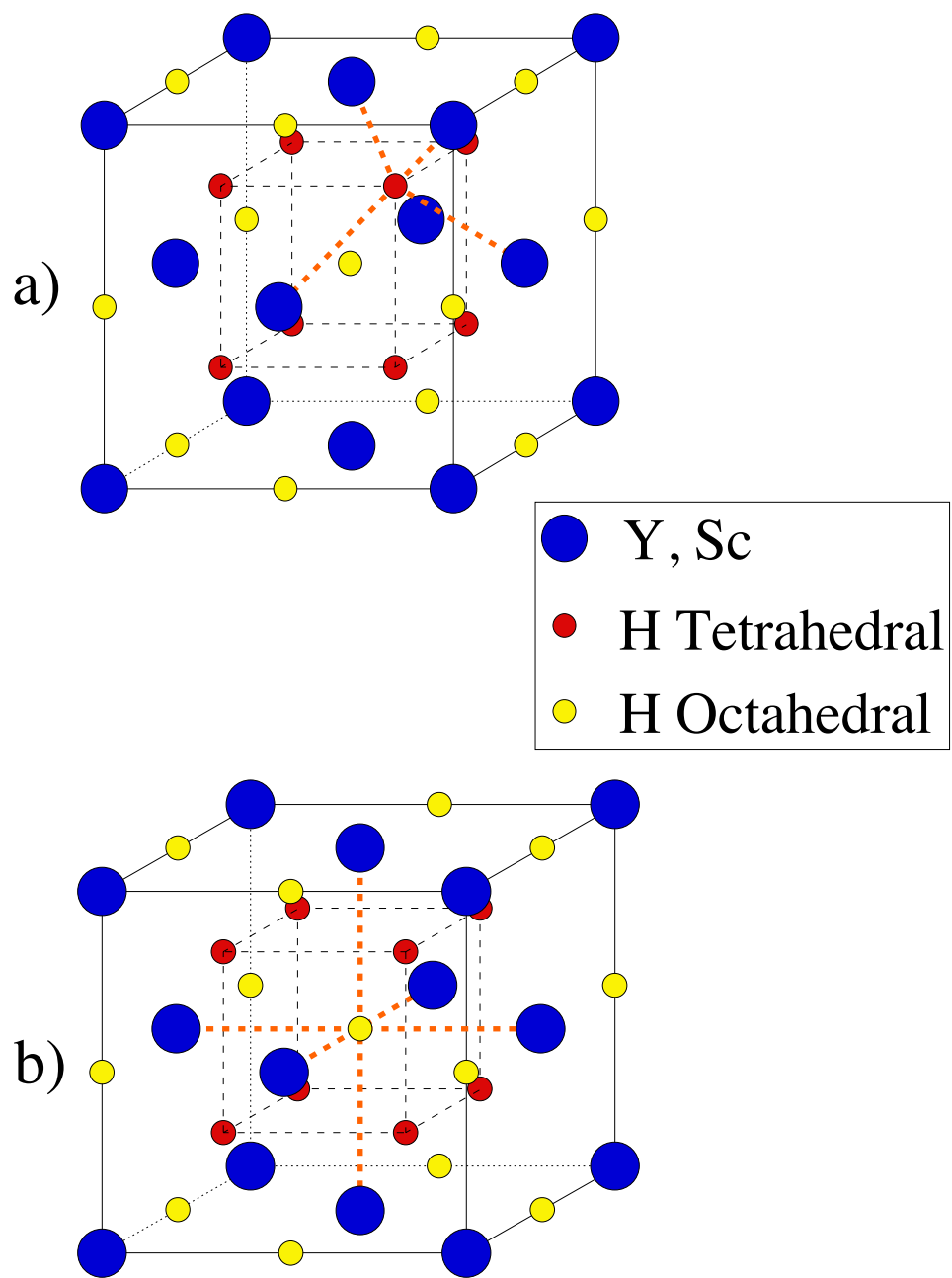


Figure 1.6: Face-centered cubic lattice with corresponding tetrahedral (a) and octahedral (b) sites.

exhibit the transition of interest from a trihydride. It was believed substitution of Sc could lead to a structural instability when the lattice is just large enough to store three H atoms per metal atom. In such strained situations many exotic behaviors are seen. Indeed, we have found rather interesting results for this alloy system. Figure 1.8 shows that the entire alloy phase diagram from pure Y to pure Sc forms at relatively low temperature [76]. Previous research on bulk  $Y_{1-z}Sc_zH_x$  properties indicate hydrogen absorption beyond a dihydride composition for alloys of  $z \leq 0.4$  near  $240^\circ\text{C}$  [7]. Our results indicate hydrogen concentrations in excess of dihydride occur for all alloys at room temperature and one atmosphere of hydrogen for thin films. Also, we observe the most dramatic changes in the transition near  $z = 0.20$ . We discuss these observations in terms of the local structure around interstitial sites in the alloy.

The poorly understood dynamics of the optical switching properties in Y and La thin films have initiated this study. Although the technical prospects for these materials are interesting and should be investigated, the aim of this dissertation is to aid the understanding of the physics behind the metallic-mirror to transparent-insulator transition. We have primarily studied the optical and electrical behavior of the  $Y_{1-z}Sc_zH_x$  system. These properties are discussed extensively in Chap. 4 after a short comment on the structural analysis from x-ray diffraction in Chap. 3. A summary and a brief mention of possible future directions for this work appear in Chap. 5.

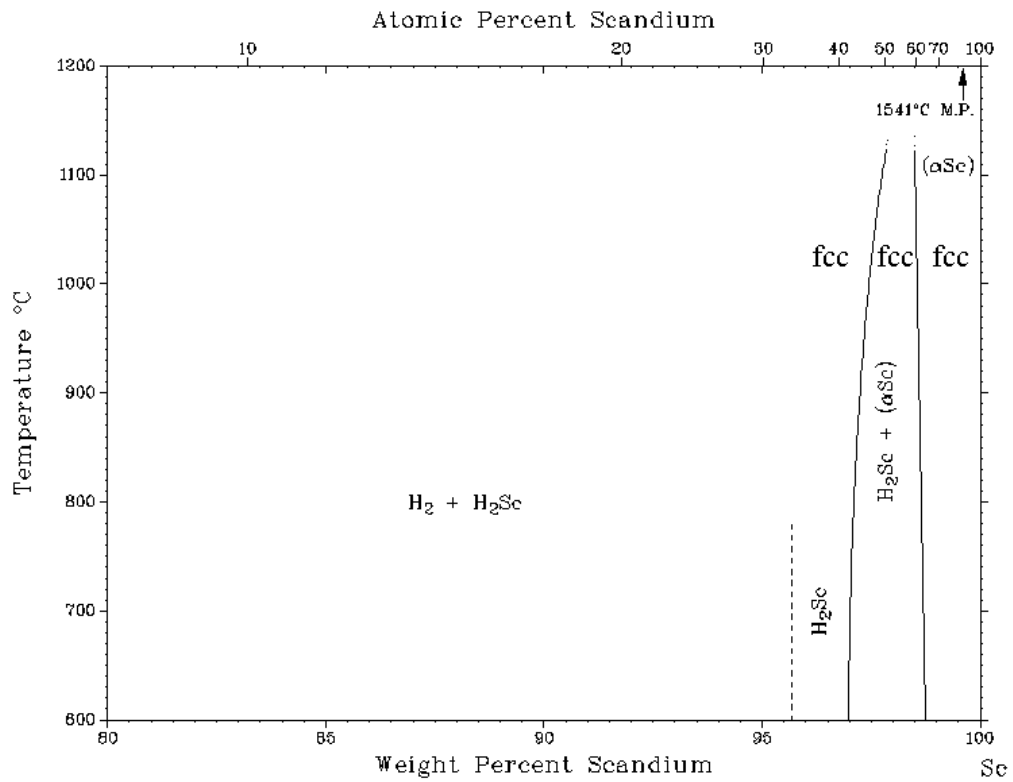


Figure 1.7: Hydride structure and phase diagram for Sc. There are two distinct phases:  $\alpha$  (fcc monohydride) and  $\beta$  (fcc dihydride).

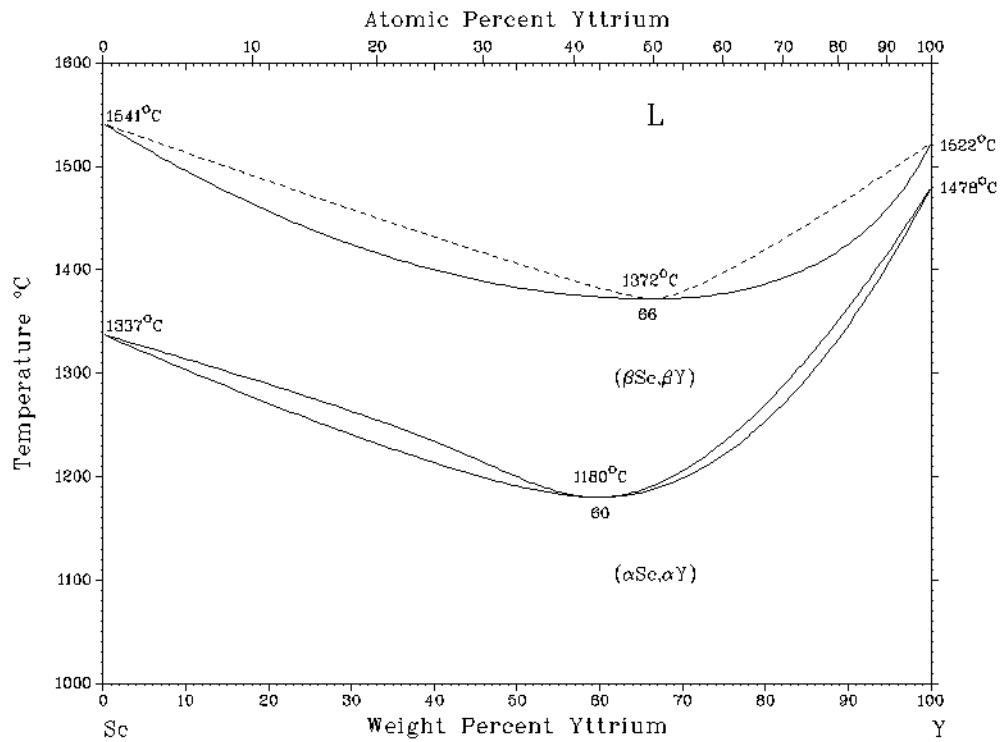


Figure 1.8: Phase diagram for the  $Y_{1-z}Sc_z$  alloy system. The diagram indicates a solid solution is possible of all alloys of Y-Sc.

## Chapter 2

### Experimental

*“Ross: So, I just finished this fascinating book. By the year 2030, there’ll be computers that can carry out the same amount of functions as an actual human brain. So, theoretically, you could download your thoughts and memories into this computer and live forever as a machine.*

*Chandler: And I just realized I can sleep with my eyes open.”*

*- from Friends on NBC*

Various elements of our main experimental techniques are described in this chapter. Included are sections about sample preparation and characterization using x-ray diffraction (XRD), optical spectrometry, and ac electrical resistivity ( $\rho(x)$  and  $\rho(T)$ ).

#### 2.1 Sample Preparation

The thin film sample preparation for this metal-hydride work was performed in two stages. The active layer metals and alloys were cast into 0.125” diameter rods from stoichiometric combinations of 99.9% (or better) yttrium (Y) and scandium (Sc). To do this, the metals were first arc-melted on a water-cooled copper hearth

in an under-pressure of ultra-high purity argon ( $\approx 125$  torr below atmosphere). The actual argon pressure used depended on the fluidity of the alloy melt. For high surface tension alloys, higher pressures made pulling the melt into a copper mold easier. The inert argon environment was gettered to remove oxygen using (99.9% purity) zirconium sponge. To ensure homogeneity, the samples were turned over and arc melted 3–5 times. The alloy lumps were weighed to ensure that loss of constituents is less than 0.1%. Palladium (Pd) of 99.95% purity is purchased commercially in 2 mm diameter rods. The Y-Sc alloys and the palladium were then cast into rods, also by arc-melting. When these rods became too short for use in the e-beam evaporators, arc-melting was used to combine several scrap pieces into one useful rod.

The alloys and Pd were electron-beam evaporated in vacuum ( $\approx 10^{-8}$  torr) using two pendant-drop-type evaporators. The vacuum chamber used was constructed by the author and is shown in the photo of Fig. 2.1. A tutorial on film growth can be found in Appendix A. Figure 2.2 is a photograph of one of the e-beam evaporators. A close-up of the metal to be evaporated and the tungsten filament which produces the electron beam are shown on the right. Leybold Inficon crystal growth monitors were used to monitor film deposition rates and total thickness. The monitors were calibrated using a reference table supplied by Leybold which lists density and  $Z$ -number for each element. The alloy densities and  $Z$ -numbers were calculated from the parent elements based on the molar ratios. It is suggested for future film growth to obtain ellipsometric, low-angle x-ray scattering, profilmetric, or some other measurement to verify the film thickness. All films were grown on



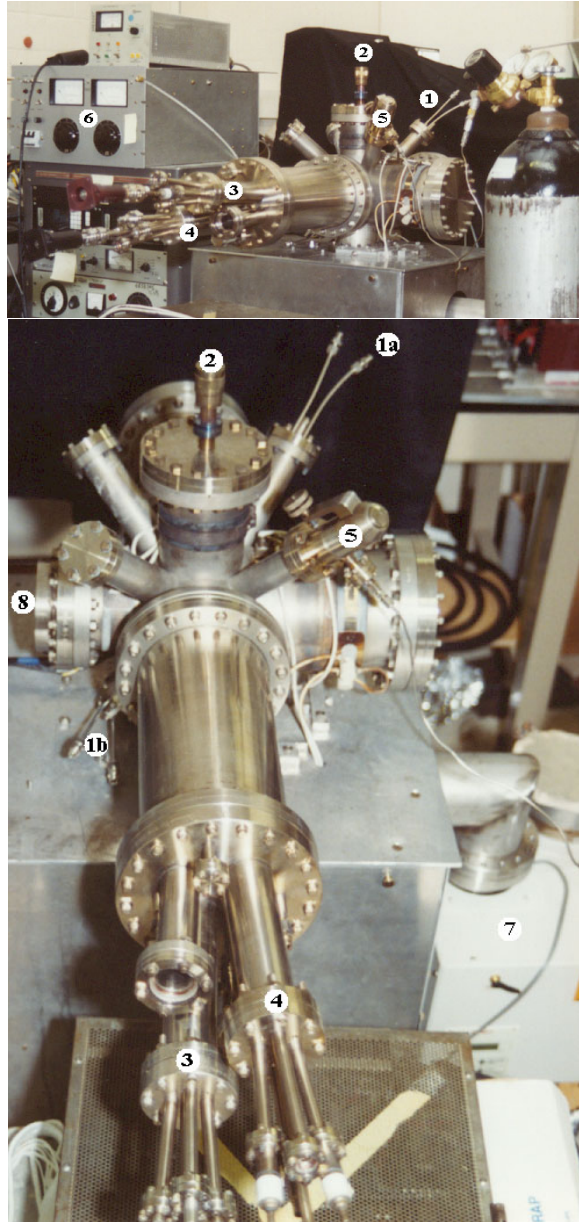


Figure 2.1: Vacuum chamber used for metal-hydride film growth: 1a-b) Leybold crystal growth monitors, 2) rotating substrate/shutter feedthrough, 3-4) e-beam evaporators, 5) leak valve, 6) e-beam evaporator power supply, 7) turbo and roughing pump station, 8) substrate viewport.

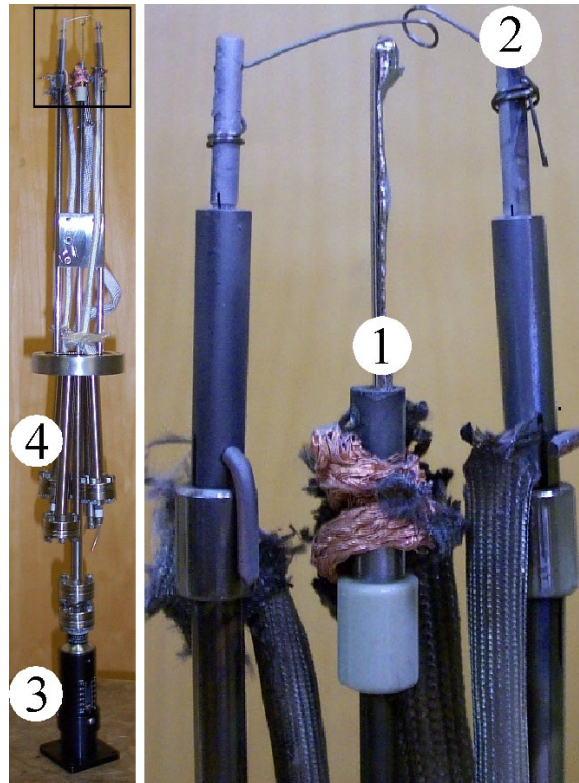


Figure 2.2: Pendant-drop electron beam evaporator. The rectangular section on the left image is blown up in the image on the right. 1) Sample rod, 2) filament, 3) linear-motion sample manipulator, 4) external electrical connections.

$1 \times 1 \text{ cm}^2$  glass microscope slides and amorphous quartz. No substrate heating was used during film growth. Typical chamber temperatures were  $23\text{--}30^\circ\text{C}$ . The alloy active layers were grown to  $100 \pm 5 \text{ nm}$ , as verified by the growth monitors. The protective palladium layers were deposited as  $10 \pm 1 \text{ nm}$ .

The substrates were cut from the larger pieces using a diamond saw and acetone for cutting fluid. The saw tends to leave rough edges, which were polished smooth by the diamond blade edge in order to make mounting easier in the

spectrometer and low-temperature resistivity probe. Systematic studies have been performed to achieve the best substrate cleaning procedure [6]. In this study, it was found that rubbing with fingers is superior to cotton-wool swabs. Ultrasonic cleaning did not lower particle densities, and, surprisingly, acetone contaminates substrate surfaces regardless of its initial purity. Conversations with Ben Shoulders of the Chemistry Department at the University of Texas at Austin suggest that acetone contains polymers that are easily broken causing them to adhere to surfaces such as substrates and vacuum chamber interiors. These polymers behave like dirt, and, therefore, acetone should not be used for cleaning substrates or vacuum components. The following procedure has been adopted for these studies and resulted in long-lasting films which were resistant to peeling.

1. Wash hands with soap.
2. Rub the substrate with Glass Plus<sup>TM</sup> glass cleaner for 30 seconds with bare fingers.
3. Remove excess glass cleaner with n-propanol
4. Soak substrates for 10 seconds in n-propanol and rub with bare fingers until they feel squeaky clean.
5. Spin the substrates dry in a modified coffee grinder spinner.

For film evaporation, the substrates were mounted to a rotating substrate holder with double-sided tape. This method of adhesion is not the optimal method; however, silver epoxy, Torr Seal, and two-part epoxy all resulted in substrate breakage

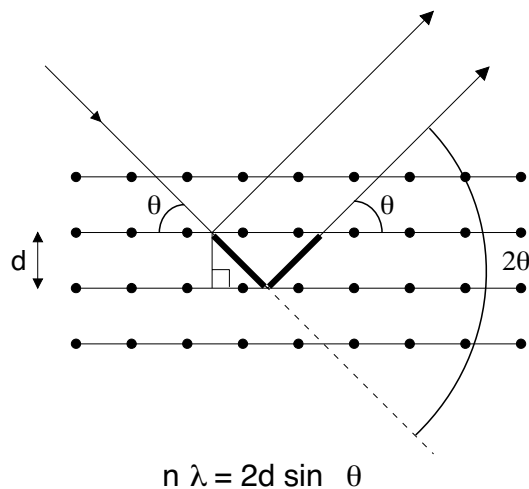


Figure 2.3: Diagram for Bragg scattering and diffraction of x-rays from parallel layers of a material. The bolded lines identify the path difference of the two outgoing rays.

upon removal, regardless of the amount of epoxy used. The tape residue was also easily removed with methanol after deposition, unlike the epoxies. Superglue should never be used in vacuum!

## 2.2 X-ray Diffraction

Crystallinity and lattice structure were studied using x-ray diffraction. A schematic of x-ray scattering is shown in Fig. 2.3. Crystallites in the metal films elastically scatter x-rays. The detected x-rays will have phase differences dependent upon scattering specifics leading to the Bragg scattering condition for constructive interference,  $n\lambda = 2d \sin \theta$ . This creates an angle-dependent interference pattern with information about lattice spacing and unit cell structure. Because of the polycrystallinity, all crystal orientations are expected to appear in the diffraction pattern.

The samples are scanned over the range  $2\theta = 10^\circ\text{--}70^\circ$  at  $0.05^\circ$  increments. Each angle is integrated for 3–7 seconds. The machines used were Philips (model PW 1720) RIGAKU diffractometers which produce x-rays with  $\lambda = 1.540562 \text{ \AA}$  (Cu  $K_{\alpha 2}$  line). MDI Datascan software was used to control the goniometer (also manufactured by Philips). Powder diffraction references for Y,  $\text{YH}_2$ ,  $\text{YH}_3$ , Sc, ScH,  $\text{ScH}_2$ , and Pd were obtained from MDI Jade pattern analysis software [26].

### 2.3 Optical Spectroscopy

Optical spectra were measured using a Bausch and Lomb Spectronic 20 spectral analyzer shown in Fig. 2.4. This type of spectrometer used a rotating reflection grating to split light into specific wavelengths as shown in Fig. 2.5. The spectral bandwidth incident on the sample was 20 nm. The diffraction grating was the blazed angle variety which consists of stepped edges with angle  $\gamma$  to the normal. Without the blazed angles the interference peaks would be described by the standard diffraction grating equation

$$a \sin \theta_m = m\lambda, \quad (2.1)$$

for normal incidence, line spacing,  $a$ , and  $\theta_m$  is the angle to the  $m^{\text{th}}$  order peak. If the incoming light is at an oblique angle,  $\theta_i$ , this equation is generalized to

$$a(\sin \theta_m - \sin \theta_i) = m\lambda. \quad (2.2)$$

It follows when  $\theta_m = \theta_i$ , the zeroth order peak is observed, however, this is the same angle for all wavelengths. Therefore, a large amount of reflected intensity is wasted in an unresolvable region. Use of a blazed angle grating, however, circumvents this

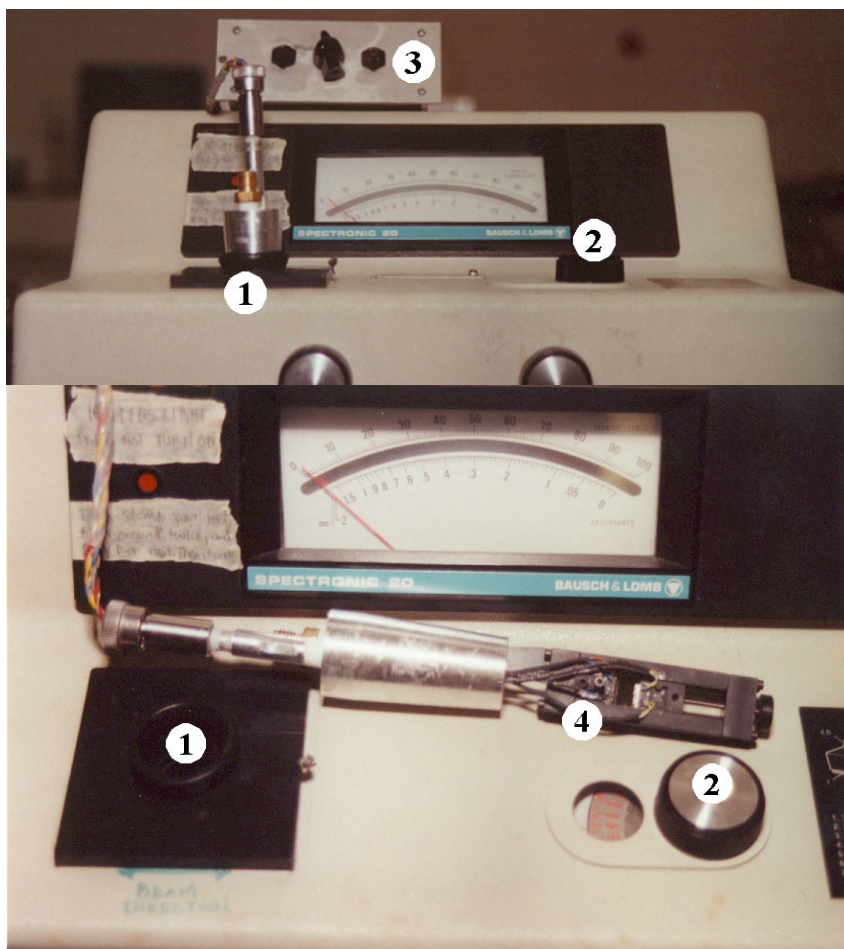


Figure 2.4: Bausch and Lomb Optical Spectrometer: (1) customized sample insert tube, (2) wavelength selector (340–960 nm), (3) switch box for in-line and van der Pauw resistivity, (4) film mounting apparatus for 4-point resistivity and simultaneous optical transmission measurements during hydrogen loading.

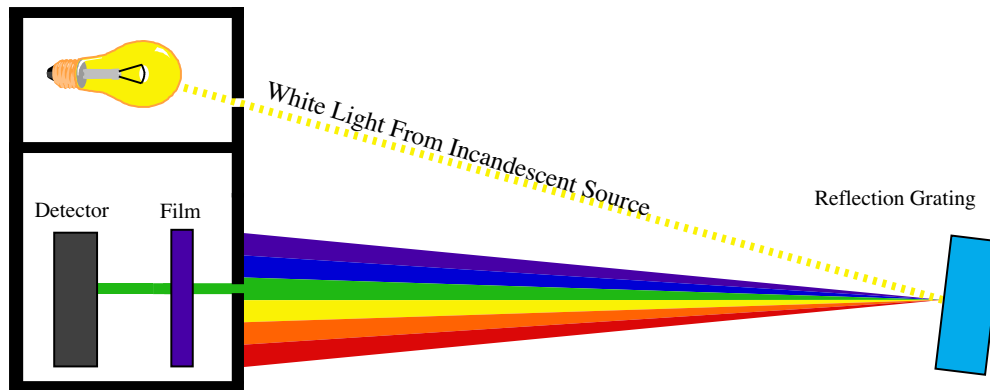


Figure 2.5: Schematic of the Bausch & Lomb Spectronic 20 rotating reflection grating.

issue. The blazed angles make it possible to shift reflected light energy away from the specular  $0^{th}$  order peak. Referring to Fig. 2.6, specular reflection occurs for  $\theta_i - \theta_r = 2\gamma$ . Now, light incident at an angle normal to the grating implies  $\theta_r = -2\gamma$  (negative because both incident and reflected rays are on the same side of the grating normal). The specular energy now corresponds to a nonzero order peak, or  $\theta_m = -2\gamma$ , and the grating now satisfies

$$a \sin(-2\gamma) = m\lambda, \quad (2.3)$$

for the desired  $\lambda$  and  $m$ . For more details on this type of spectrometer, see, for example, Hecht [73].

The Spectronic 20 measures relative transmission intensity between wavelengths of 340 and 960 nm. The original design included a vacuum tube photodetector. It was outdated, and degradation had made it insensitive to the intensities transmitted through our unhydrated films. The vacuum tube was replaced with a normal response, silicon photodiode (Edmund Scientific stock #:A54-035) with a

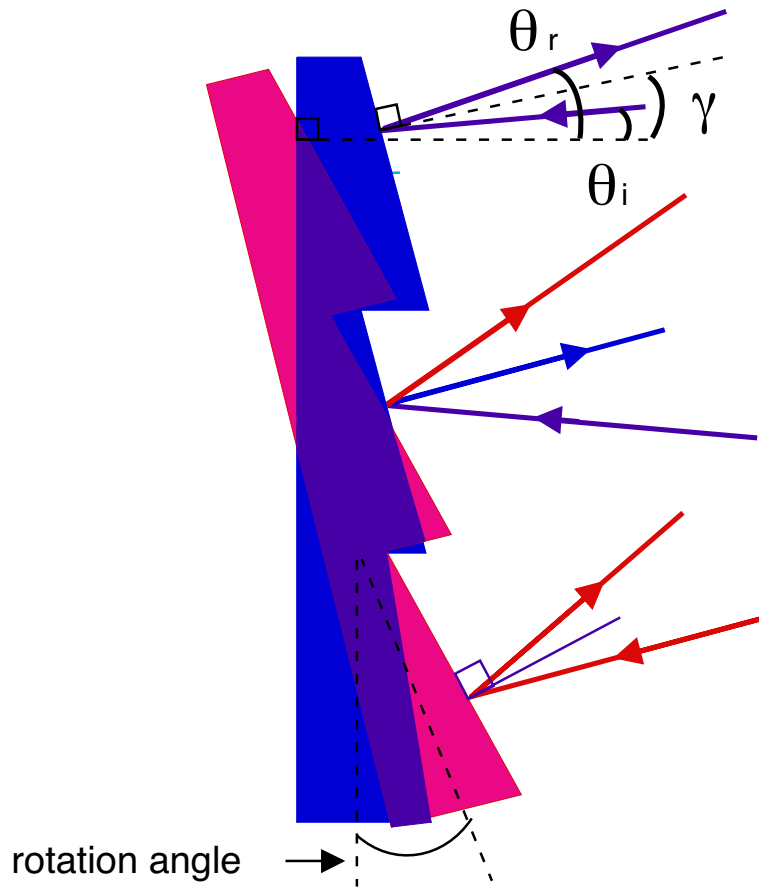


Figure 2.6: White light incident on the blaze angle reflection grating is split into constituent colors, which one can select on the spectrometer based on the angle of the reflection grating.



44 mm<sup>2</sup> square sensor area. Current induced in the photodiode due to light transmission was converted to voltage using a simple current-to-voltage conversion circuit (see Fig. 2.7). A large resistor is necessary to make the voltage drop appreciable. A 1 M $\Omega$  variable resistor was used to tune the circuit such that the full intensity of the spectrometer bulb would not saturate the photodiode current. Replacing the original photodetector removed the capability to “zero” the dark current. The plot in Fig. 2.7 shows a typical photodiode response curve with the minimum detectable signal plotted as a solid line. All transmittance values are calculated using a response spectra measured at the time of hydrogen loading and the noise level. The response spectra are measured with the sample probe completely removed from the spectrometer. Response spectra measured with the sample probe in place do not vary significantly from those without it or those with a quartz substrate in the beamline. Transmittance is reported as

$$T(\omega) = \frac{I_T(\omega)}{I_o(\omega)}, \quad (2.4)$$

where  $I_T(\omega)$  and  $I_o(\omega)$  are the measured transmission during hydrogenation and the diode response, respectively. Both spectra have the baseline noise subtracted from them.

The sample space tube was changed to a larger diameter in order to insert a Delrin sample holder and to enable gas flow through the spectrometer. The sample holder is capable of making four-contact resistivity measurements in several different contact configurations discussed in the following section. The larger sample tube of the spectrometer was able to be filled with partial pressure hydrogen concentrations

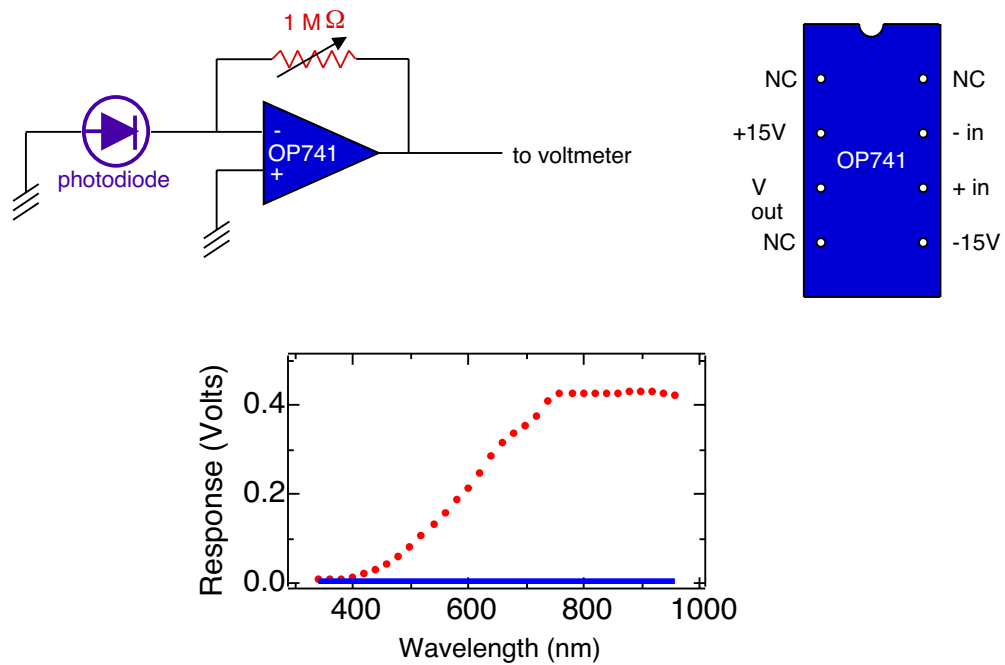


Figure 2.7: Current-to-voltage circuit diagram for the photodiode measuring optical transmission in the Bausch and Lomb spectrometer. The graph shows a typical photodiode response as a function of incident wavelength. The solid line is the baseline due to dark current.

to 0.75 torr ( $\approx 1$  mbar or 0.1% hydrogen:argon). This flow control was important for slowing the hydrogen absorption, and thus, the optical switching rate, so that many optical spectra could be recorded throughout the transition. Typically, the total switching time was on the order of 2 hours. The gas flow control was performed using an MKS Baratron mass flow controller. Hydrogen loading is performed in 1 atm of mixtures of hydrogen in argon with typical flow rates of 10-50 sccm.

## 2.4 AC Electrical Resistivity

The room temperature resistivity probe was machined from delrin and designed to measure resistivity in an in-line 4-point configuration or by the van der Pauw method (see Fig. 2.8). Selection between these two configurations was made by a rotary switch box. The in-line 4-point method (Fig. 2.9) was used exclusively due to speed and simplicity. In this geometry, resistivity can be calculated directly from the resistance measured and the geometry of the pins as

$$\rho = \frac{RA}{l}, \quad (2.5)$$

where  $R$  is the measured resistance,  $A$  is the cross-sectional film area ( $w \times h$ ) through which current flows, and  $l$  is the distance between the voltage contacts. Error from this technique is inherent due to the assumption that  $l \gg w$  and difficulty measuring the sample dimensions. The van der Pauw method requires switching between two orthogonal configurations shown in Fig. 2.10. Resistivity is calculated as

$$\rho = \frac{\pi h}{\ln 2} \frac{R_0 + R_{90}}{2} f\left(\frac{R_0}{R_{90}}\right), \quad (2.6)$$

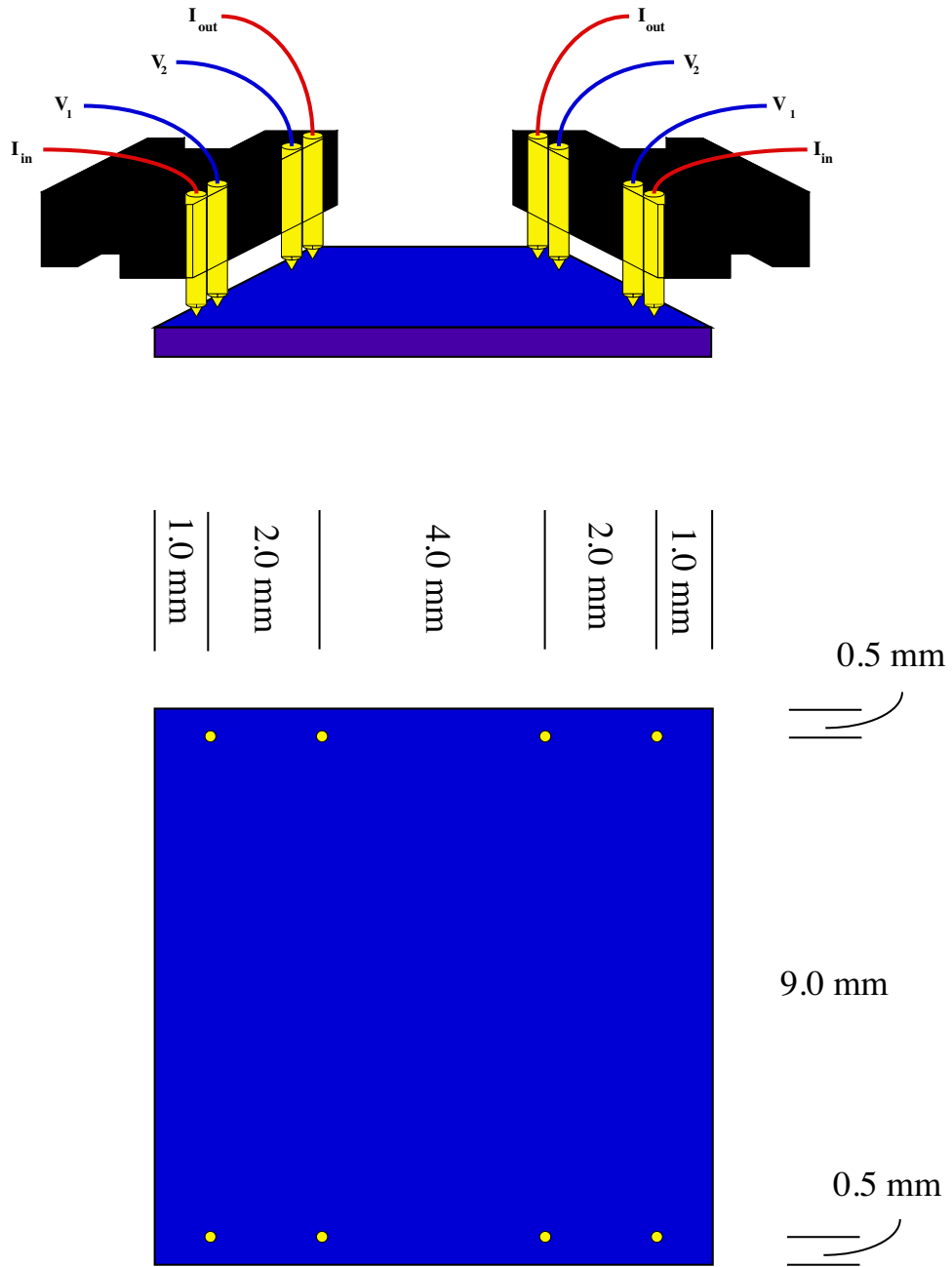


Figure 2.8: Contact configuration of the room temperature resistivity probe.

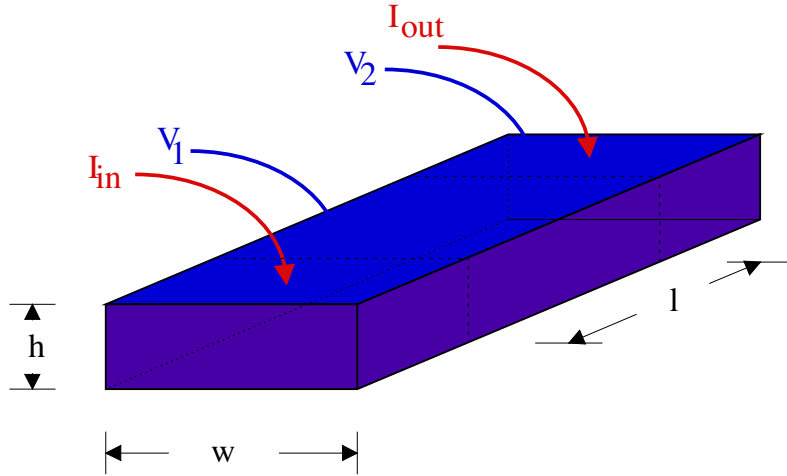


Figure 2.9: In-line 4-point contact geometry for ac resistivity measurements. The entire sample represents a 1–2 mm wide strip from a  $1 \times 1 \text{ cm}^2$  film. In this configuration,  $\rho = Rhw/l$ .

where  $f(R_0/R_{90}) \approx 1$  for isotropic materials, such as polycrystalline films. This technique has smaller error and is roughly independent of the sample geometry, however, it is more difficult to estimate and requires some analysis due to the function  $f$ .

The sample contacts were gold-coated pogo sticks mounted into the sample holder with spacings shown in Fig. 2.8. The films were sectioned using a diamond-tipped scribe such that a 1–2 mm width area of the film was used for resistivity and the other 8–9 mm was used for spectroscopy. Contact resistances were monitored and kept below  $1 \Omega$ . A Linear Research LR-400 ac resistance bridge was used to record resistance of the films. Use of an ac resistance bridge eliminates effects due to temperature gradients and high contact resistances.

Temperature-dependent resistivity measurements were subsequently made

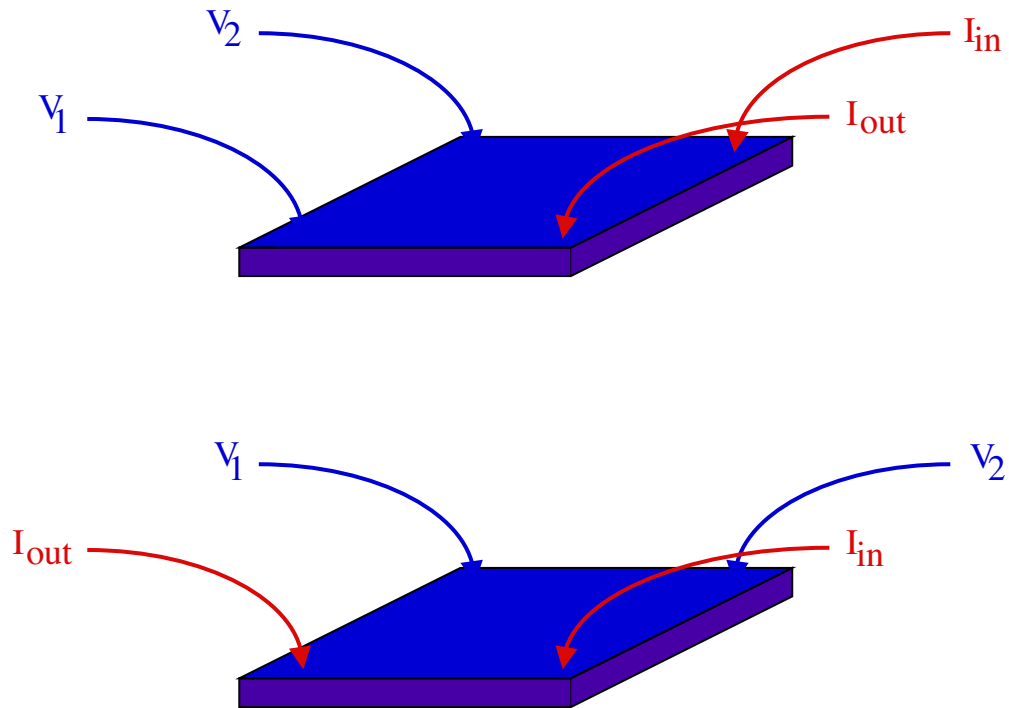


Figure 2.10: The van der Pauw technique for 4-contact ac resistivity measurements.

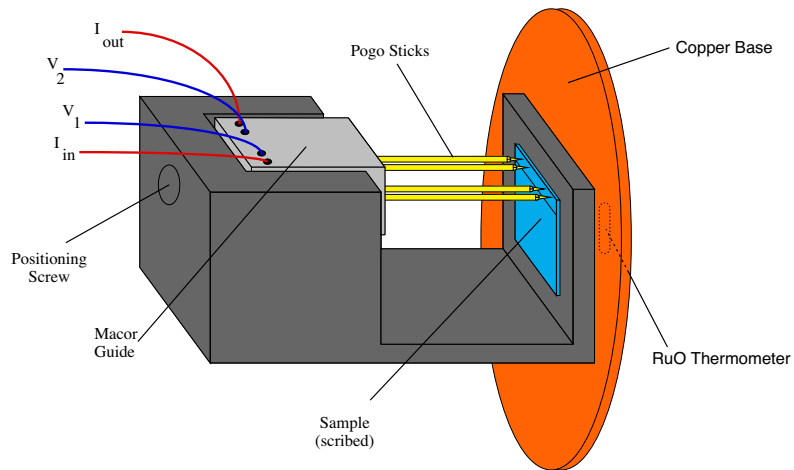


Figure 2.11: Sample mount for temperature-dependent in-line 4-contact resistivity measurements on films.

independent of spectroscopic measurements. The sample holder was designed from brass to mount to a copper base. This is shown in Fig. 2.11. Gold coated pogo sticks were again used for sample contact. In this probe, the voltage contact spacing was 0.635". A set screw was used to guide a piece of macor and compress the pogo sticks to make contact with copper wires inserted into the macor. A calibrated RuO thermometer (2–300 K range) was mounted to the copper base with cry-con grease for good thermal conductivity. The copper base was attached to the probe stick with gold coated pin-socket connections. Some metal surfaces were coated with cry-con grease to ensure thermal conductivity. The probe design made simultaneous measurement of four samples possible; however, the film mount was only made to hold one sample per temperature run. The probe and Cryolab liquid helium dewar were connected to a pumping station and gas manifold. It was possible to evacuate or flow helium to the dewar and probe. The probe could also be pumped or filled with hydrogen, separately.

## 2.5 Block Diagrams

The room temperature measurements were designed for simplicity. All of measurements were recorded using commercial software, LabVIEW v.6. The virtual instrument (VI) programs are discussed in Appendix B. LabVIEW was interfaced via GPIB connections from a Macintosh G4 to two Keithley 195(A) digital multimeters. One multimeter was connected to the LR400  $\pm 2$  VDC output for monitoring resistance of the sample. This output scales with the range selected on the LR400 front panel. The second multimeter was connected to the voltage output of the

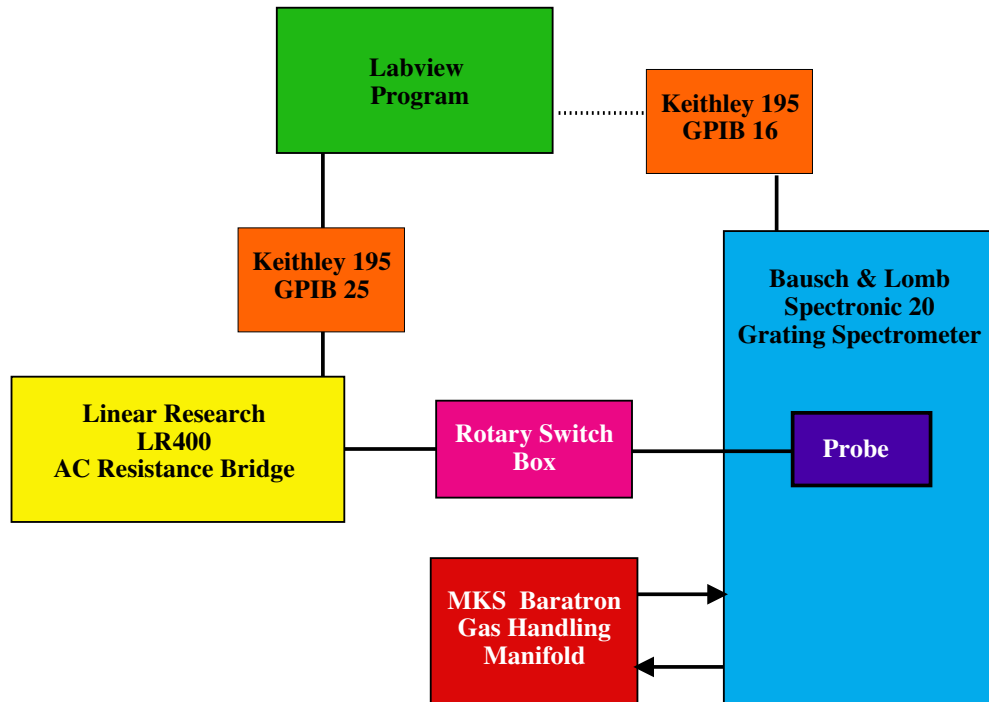


Figure 2.12: Block diagram of the room temperature optical spectroscopy and resistivity measurement system. Transmission spectroscopy (340–960 nm wavelengths) was measured simultaneously with electrical resistivity. Phototransmission induces a current in a photodiode, which was converted to voltage and measured with a Keithley 195 DMM. In-line 4-point resistivity was measured with an LR-400 ac resistance bridge. All measurements were recorded using Labview v.6.



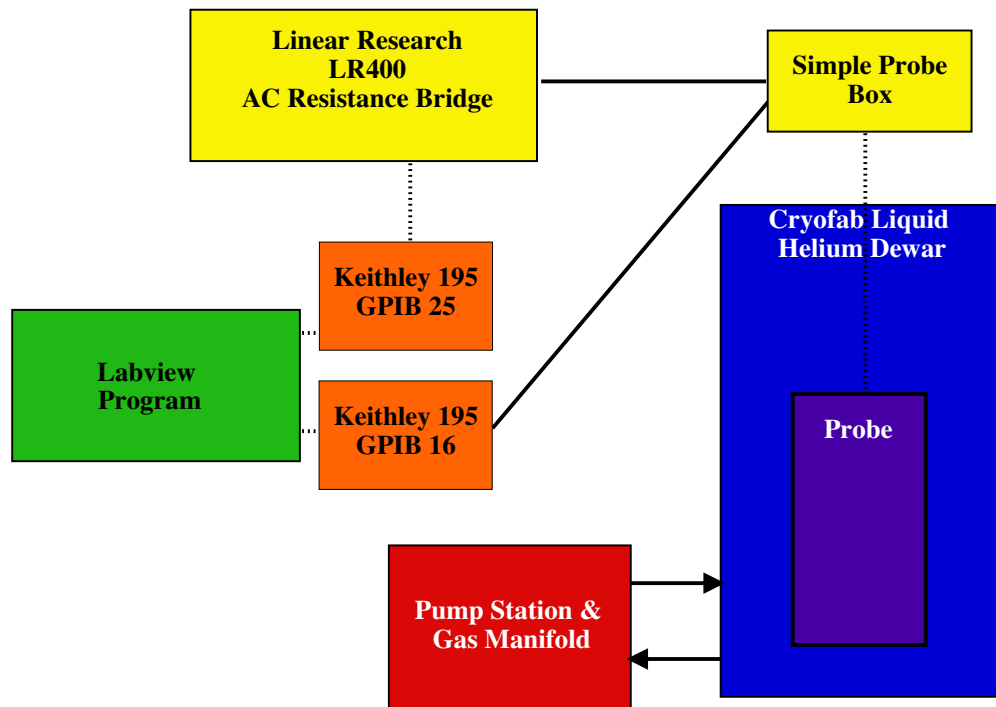


Figure 2.13: Block diagram of the temperature dependent resistivity measurement system. In-line 4-point resistivity was measured with an LR-400 ac resistance bridge and output to a Keithley 195A DMM. Temperature was monitored with a calibrated RuO thermometer connected in a 4-contact geometry to a Keithley 195 DMM. All measurements are recorded using LabVIEW v.6.

current-to-voltage circuit of Fig. 2.7. The rotary switch box (discussed in the previous section) was used to select between the possible resistivity pin configurations. Gas flow connections were made with brass and stainless steel Swagelock or VCR fittings. Plastic and stainless steel gas conduits directed gas through the spectrometer. Figure 2.12 shows the block diagram of the room temperature experiment.

For temperature dependent resistivity measurements, a similar LabVIEW VI was created (also discussed in Appendix B). One multimeter monitored film

resistance, while the second measured the RuO thermometer resistance. The thermometer resistance was converted to temperature within the VI. Both the dewar and the probe were connected to a pumping station and gas flow manifold.

## Chapter 3

### Structural Analysis

*“Well, we talk about physics, the properties of physics...”*

*- Brian in The Breakfast Club*

This study is based on lattice size effects on the switchable mirror transition in yttrium. X-ray diffraction, as discussed in the previous chapter, is a powerful tool for detailing both structure and lattice dimensions upon substitution of Sc into the Y lattice. The following is an analysis of x-ray diffraction for both the as-deposited (not hydrided) and unloaded (dihydride) films.

#### 3.1 As-Deposited Films

In a perfect world, where delta functions truly exist, the Bragg condition would result in sharp, delta-function peaks at angles of constructive interference. Figure 3.1, shows the expected diffraction patterns for hcp Y, hcp Sc, and fcc Pd. Also shown in Fig. 3.1 is the measured diffraction pattern for three as-deposited alloys. The low intensities are typical of polycrystalline thin films. A broad amorphous peak near  $20^\circ$  has been removed from the data. Immediately obvious is the partial c-axis ordering in our films. In most alloys, the only observable peaks are the (100), (002), and (101); in the measured data, the (100) and (002) peaks can

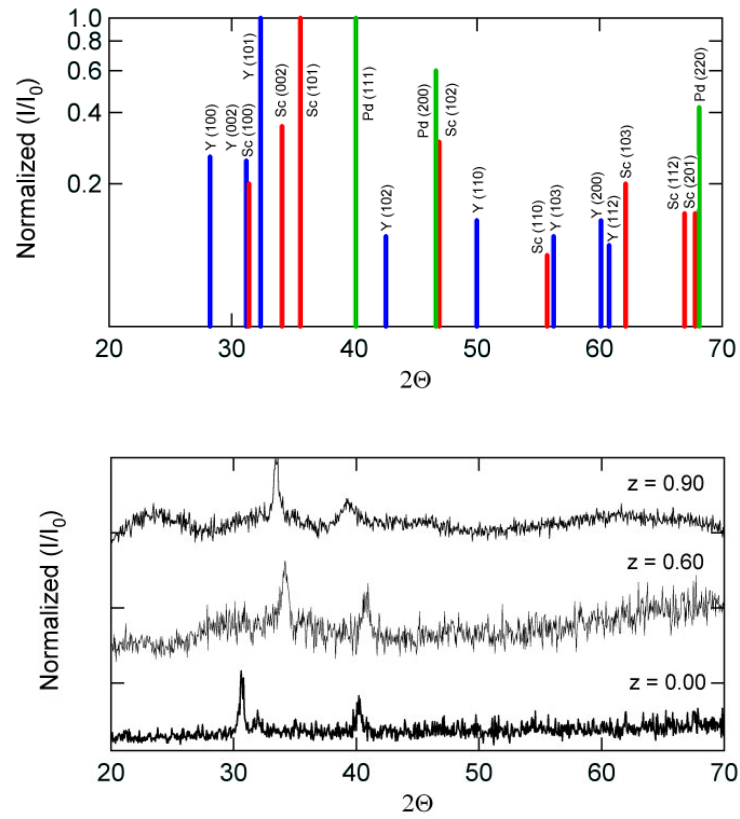


Figure 3.1: Expected and measured x-ray diffraction patterns for the as-deposited films.

be observed near  $28^\circ$  and just above  $30^\circ$ , respectively. The (101) reflection is found as a shoulder on the right of the (002) peak. The peak near  $2\theta = 40^\circ$  corresponds to Pd (111). From these, we obtain the alloy composition dependence of the lattice constants  $a$  and  $c$ , shown in Fig. 3.2. The trend is a nearly linear decrease in both lattice parameters with increasing  $z$ . The resulting total decrease in cell volume ( $V_{cell} = 3\sqrt{3}a^2c/2$ ) is  $\sim 38\%$  from  $z = 0$  to  $z = 1$ .

For  $z \leq 0.20$ , we find larger cell parameters than expected. This is due to hydrogen incorporation during evaporation. By linearly fitting literature values of  $a$  and  $c$  of  $YH_x$  for  $0 \leq x \leq 0.3$ , we calculate an initial hydrogen concentration of  $x = 0.30 \pm 0.05$  [15]. This value is larger than 0.21, the maximum H concentration for the solid-solution  $\alpha$ -phase, which implies existence of a mixed phase of hexagonal  $YH_\epsilon$  (with  $\delta \leq 0.21$ ) and cubic  $YH_{2-\delta}$ . In addition, the hydrogen incorporation varies with each alloy which leads to the deviation from the expected linear behavior. Electron diffraction studies by Curzon and Singh report that films with thickness less than or equal to 100 nm have significant dihydride formation when prepared in  $\approx 10^{-7}$  torr. The hydrogen concentration decreases as a function of film thickness [48].

For  $z > 0.20$ , the resulting lattice is smaller than expected possibly due to the presence of the cubic ScH phase. The Sc hcp (100) and (002) reflections have close angular correspondence to the fcc (111) and (100) ones, respectively. These films, grown on room temperature substrates, have very small grains. For example, an angular width of  $\sim 1^\circ$  corresponds to a particle size of  $0.1 \mu\text{m}$  [75]. This, coupled with the high hydrogen content, causes the XRD peak widths to be on the order of

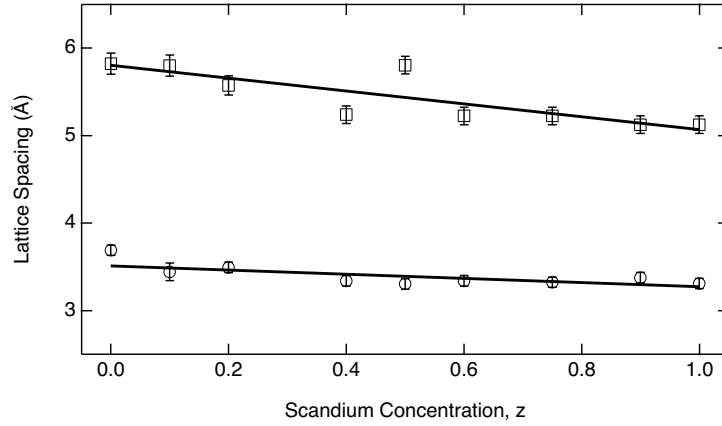


Figure 3.2: Unit cell lattice parameters,  $a$  and  $c$ , as a function of Sc concentration,  $z$ , for the hcp as-deposited films. The trend is nearly linear, as expected, with some deviations due to hydrogen incorporation during film growth and small grain size.

the separation of the peaks of these two phases ( $1-2^\circ$ ). This causes unidentifiable overlap of the two phases.

### 3.2 Dihydride Films

Films which have been loaded one or more times were also evaluated. The expected and measured XRD patterns for polycrystalline fcc  $\text{YH}_2$ , fcc  $\text{ScH}_2$ , and fcc Pd are shown in Fig. 3.3. As expected, the predominant peak is the fcc (111), which corresponds to the hcp (001) in the unhydrided Y and Sc metals. The measured unit cell parameter,  $a$ , is  $5.197 \text{ \AA}$  for  $\text{YH}_2$  and  $4.768 \text{ \AA}$  for  $\text{ScH}_2$ . These values are within 1% of the expected values [26]. One would then predict the alloy lattice parameters to fall on a line between these two values. The data in Fig. 3.4 indicate smaller than expected values for  $a$  in the range  $0.20 \leq z \leq 0.60$ . The arrow on the  $z = 0.60$  data of Fig. 3.3 indicates a small peak corresponding to  $\text{YH}_2$  (111).

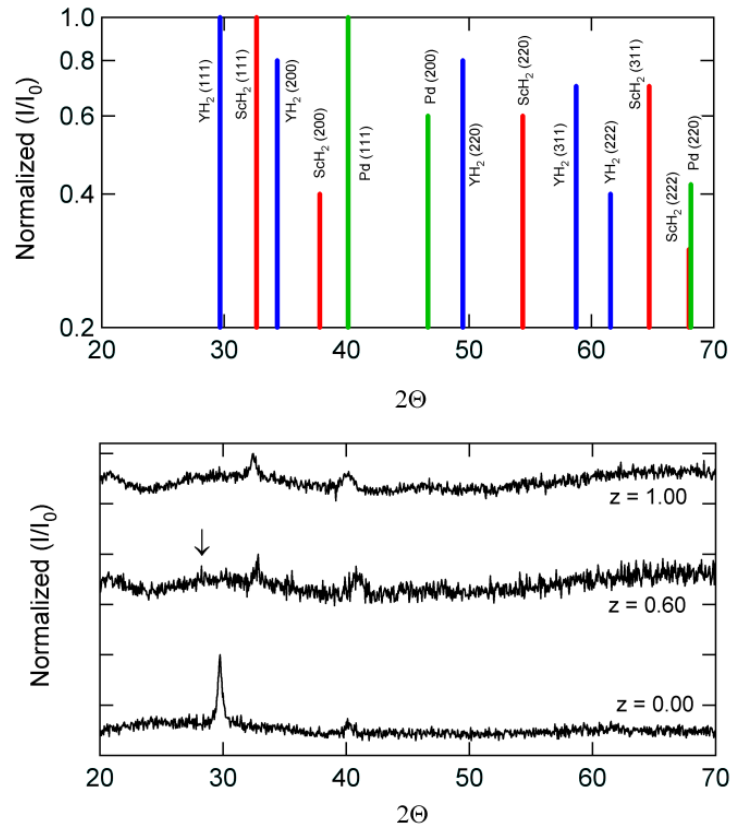


Figure 3.3: Expected and measured x-ray diffraction patterns for the dihydride concentration films.

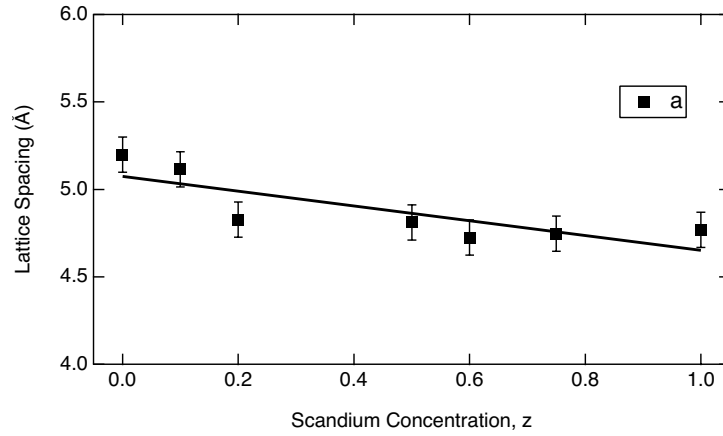


Figure 3.4: Unit cell lattice parameter,  $a$ , as a function of Sc concentration,  $z$ , for the fcc dihydride films.

This is likely due to phase separation. In the data, before the amorphous peak is subtracted, the ratio of the two (111) peaks is approximately 2:3, indicating total phase separation. Similar phase separation has been observed in alloys of Y-Mg when the alloy mixture is near 1:1. Like the Y-Mg system, optical switching still occurs, however, the shutter effect discussed in Chap. 4, is not seen in these alloys. It is possible that all alloys with  $0.20 \leq z \leq 0.60$  experience some phase separation after hydrogenation. Total phase separation can be ruled out, however the signal to noise is too small to identify partial separation.



## Chapter 4

### Results and Analysis

*“Fats, man, let me tell you my story man...”*

*- Gary in Weird Science*

#### 4.1 Introduction

The reflecting metal to transparent insulator transition is dependent on formation of a trihydride phase in rare-earth metals. The transition occurs between the dihydride and trihydride concentrations [2]. It has been observed that trihydride-forming alloys (e.g.,  $\text{La}_{1-z}\text{Y}_z$ ) undergo different switching mechanisms than combinations of trihydride- and dihydride-forming metals (e.g.,  $\text{Mg}_{0.50}\text{Y}_{0.50}$ ), where the latter phase separate [24, 29, 31]. In the  $\text{Mg}_z\text{Y}_{1-z}\text{H}_x$  system, disproportionation creates a mixture of  $\text{YH}_2$  and metallic Mg. Further hydrogenation forms insulating  $\text{MgH}_2$  and  $\text{YH}_3$ . The magnesium behaves as a microscopic shutter, enhancing reflectivity in the metallic state and increasing the optical gap in the transparent state. The result is a switchable mirror with large hydride transmittance over the entire optical spectrum.

Scandium also maximally forms a dihydride. For this reason, Sc does not undergo a phase transition from a metallic-mirror to a transparent-insulator. How-

ever, yttrium and scandium are chemically very similar with  $d^1s^2$  valence electrons, as reflected in the bulk phase diagram of Chap. 1. Optical transmission spectroscopy of the  $Y_{1-z}Sc_zH_x$  alloys reveals that the optical gap seen in  $YH_{3-\delta}$  is strongly suppressed for scandium concentrations of 20% and greater. For alloys with greater than twenty percent Sc, dihydride transmittance is observed as in the  $YH_x$  and  $La_{1-z}Y_zH_x$  systems [2, 24]. Electrical properties also exhibit a transition from insulating to metallic as a function of Sc concentration. In addition there is an interesting metal-insulator transition observed between  $z = 0.00$  and  $z = 0.10$ .

In this chapter details of the optical transmittance and electrical resistivity are discussed. Disproportionation, discussed in the previous chapter, elucidates some of the observed behavior.

## 4.2 Optical Spectroscopy Results

We have performed optical transmittance spectroscopy on the alloy system  $Y_{1-z}Sc_zH_x$  over the range 340–960 nm as a function of hydrogen content,  $x$ . Measurements on the alloys with  $z \leq 0.10$  show dramatic optical switching properties commensurate with previous results for  $YH_x$  [4]. Figure 4.1 exhibits optical spectra (uncorrected for the Pd overlayer) as a function of hydrogen loading time for  $YH_x$  and  $Y_{0.90}Sc_{0.10}H_x$ . The first hydrogen loading results in a transmittance for  $YH_x$  and  $Y_{0.90}Sc_{0.10}H_x$  of 0.11 and 0.14, respectively. Although the maximum transmittance for  $z = 0.10$  is slightly larger than for  $z = 0.00$ , the  $z = 0.10$  alloy has some transmittance before hydrogen is introduced. This low-hydrogen content transmittance is echoed in the resistivity data and will be discussed more thoroughly

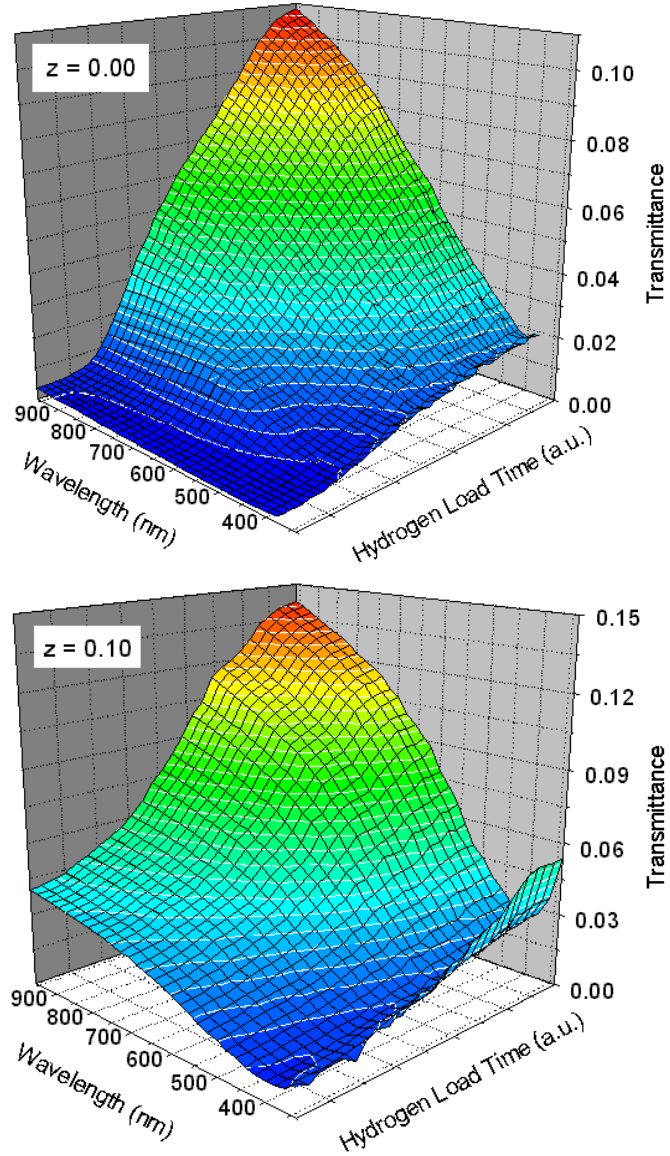


Figure 4.1: Optical transmittance spectra as a function of hydrogen loading time (in arbitrary units) starting from as-deposited films of Y and  $Y_{0.90}Sc_{0.10}$ . The optical switching capability is approximately equivalent for both samples. The full loading time scale is typically 1–2 hours.

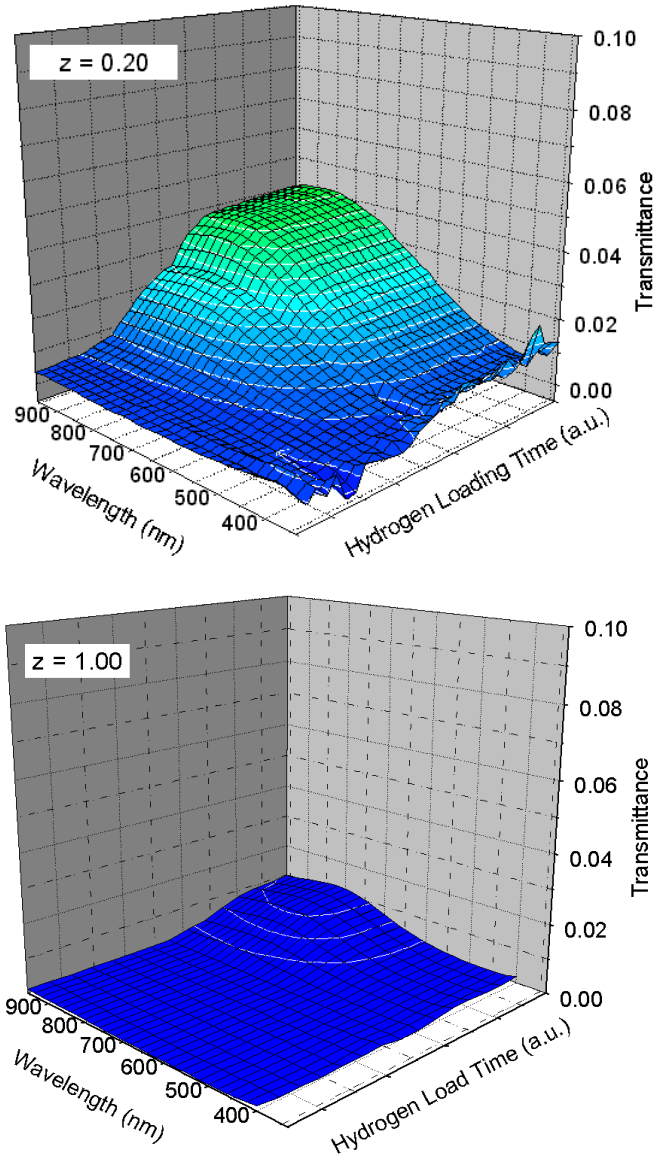


Figure 4.2: Optical transmittance spectra as a function of hydrogen loading time (in arbitrary units) starting from as-deposited films  $Y_{0.80}Sc_{0.20}$  and Sc. The vertical axis is scaled to that of the  $z = 0.00$  and  $z = 0.10$  samples. The loss of optical switching capability is evident. The full loading time scale is typically 1–2 hours.

later. The *change* in transmittance from as-deposited to fully hydrogenated is approximately the same for both of these alloys,  $\Delta T \approx 0.10$ . We find that for  $z \geq 0.20$  (Fig. 4.2) the trihydride transmittance is heavily suppressed. The reduction in fully loaded transmittance is a factor of 3 for  $z = 0.20$  and a factor of 10 for  $z = 1.00$ .

Because the real interest is in the optical transition region, it is fortunate that these alloys form stable dihydrides. The films are allowed to desorb hydrogen in flowing argon or in air for approximately 24 hours after the initial hydrogen loading; the resulting material is a stable phase very near the dihydride state ( $Y_{1-z}Sc_zH_{2\pm\delta}$ ). This state can be verified by observing the well-known dihydride transmission peak seen in the initial spectrum near  $\lambda = 700$  nm [2, 4]. Interestingly, the  $z = 0.10$  exhibits no dihydride transmittance maximum; however, the film does exhibit reversible switching properties similar to yttrium. If one looks at the change in transmittance between the dihydride and fully hydrogenated state, the loss of optical switching is even more apparent than in as-deposited spectra. The spectra in Fig. 4.3 are for the  $z = 0.00$  and  $z = 0.10$  alloys. The change in transmittance between dihydride and trihydride is a factor of 6 in the  $z = 0.00$  film and a factor of 2.3 in the  $z = 0.10$  film. We believe the  $z = 0.10$  films form a stable hydride with  $x > 2$ , explaining the lack of dihydride transparency peak. It can be seen in Fig. 4.4 that the transmittance increase for  $x > 2$  in the  $z = 0.20$  and  $z = 1.00$  films is 2.3 and 1.7, respectively. Other alloys with  $z \geq 0.20$  exhibit qualitatively similar transmittance spectra to those of Figs. 4.2 and 4.4. For films with  $z = 0.40$  (Fig. 4.5), the transmittance is trihydride-like, with a maximum at the highest measured wavelength ( $\lambda = 960$  nm). This is consistent the phase separation seen in

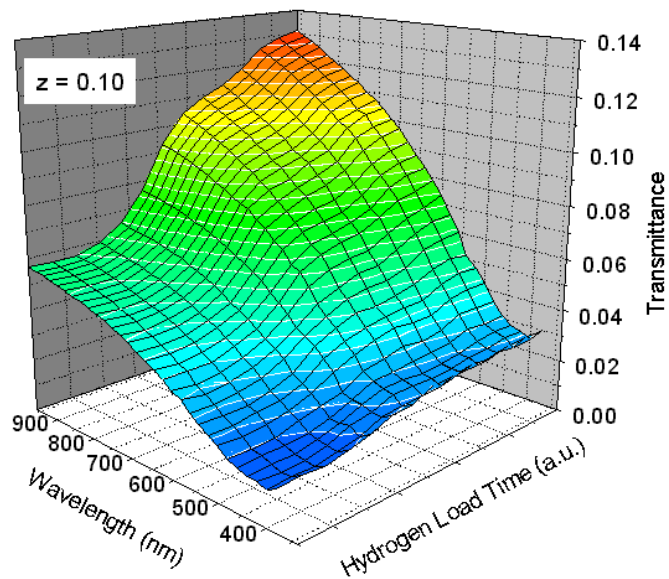
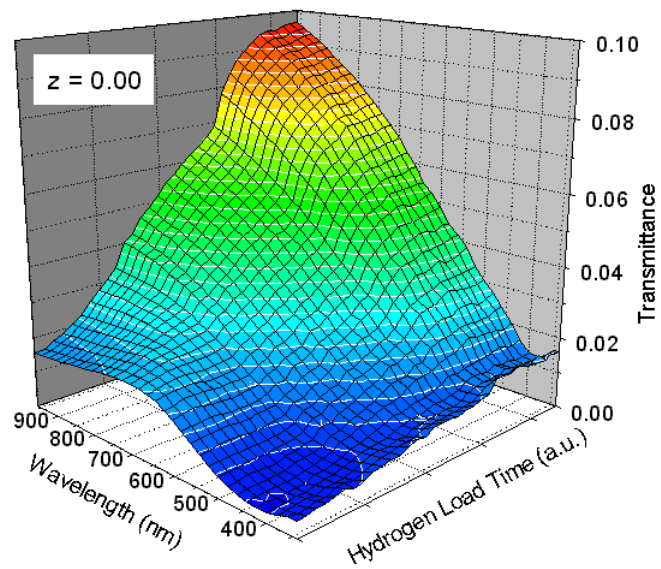


Figure 4.3: Optical transmittance as a function of hydrogen loading time (in arbitrary units) starting from unloaded ( $x \approx 2$ ) films of  $\text{YH}_x$  and  $\text{Y}_{0.90}\text{Sc}_{0.10}\text{H}_x$ . The full loading time scale is typically 1–2 hours.

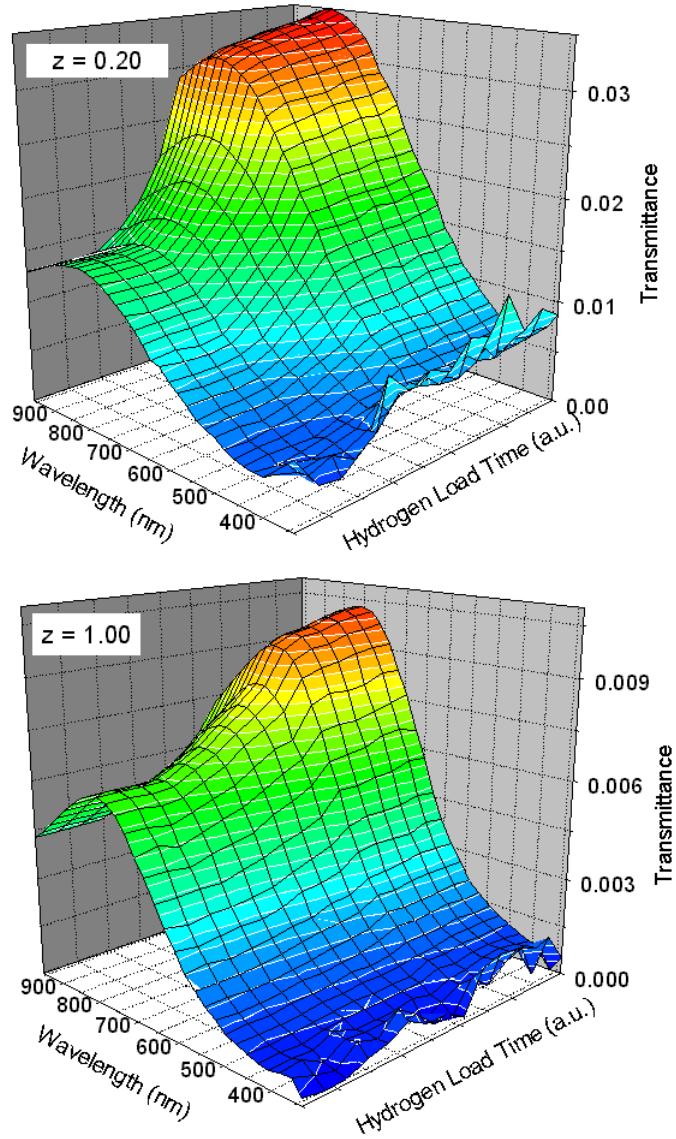


Figure 4.4: Optical transmittance spectra as a function of hydrogen loading time (in arbitrary units) starting from unloaded films (near  $x = 2$ ) of  $Y_{0.80}Sc_{0.20}H_x$  and  $ScH_x$ . The full loading time scale is typically 1–2 hours.

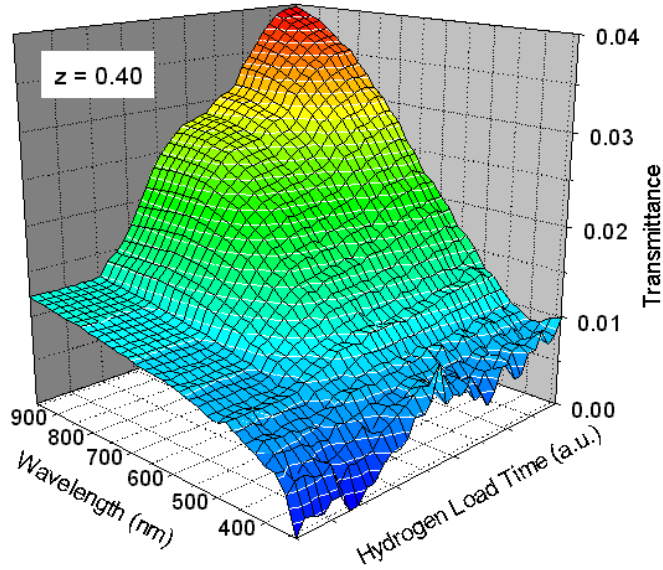


Figure 4.5: Optical transmittance spectra as a function of hydrogen loading time (in arbitrary units) starting from an as-deposited film of  $Y_{0.60}Sc_{0.40}$ . This alloy exhibits phase separation upon hydrogenation. The spectrum, therefore, has a trihydride-like appearance with maximal transmittance at  $\lambda = 960$  nm due to  $YH_3$  formation. The full loading time scale is typically 1–2 hours.

XRD data. Furthermore, we observe an increase in the transmittance for  $z = 0.40$  and  $z = 0.50$ , that is likely due to phase separated yttrium (which is able to form a trihydride).

Figure 4.6 shows hydrogen loading spectra for as-deposited and unloaded (near  $x = 2$ ) films of  $Y_{0.50}Sc_{0.50}$ . The different hydrogen concentration behavior of ( $x \approx 0.3$  and  $x \approx 2.0$ ) at the beginning of the loadings is evident.

The dihydride resistivity minimum has been mentioned in the *Introduction* and is further discussed in the next section. This minimum has been used as a concentration marker to identify the dihydride transmittance maxima for all of the



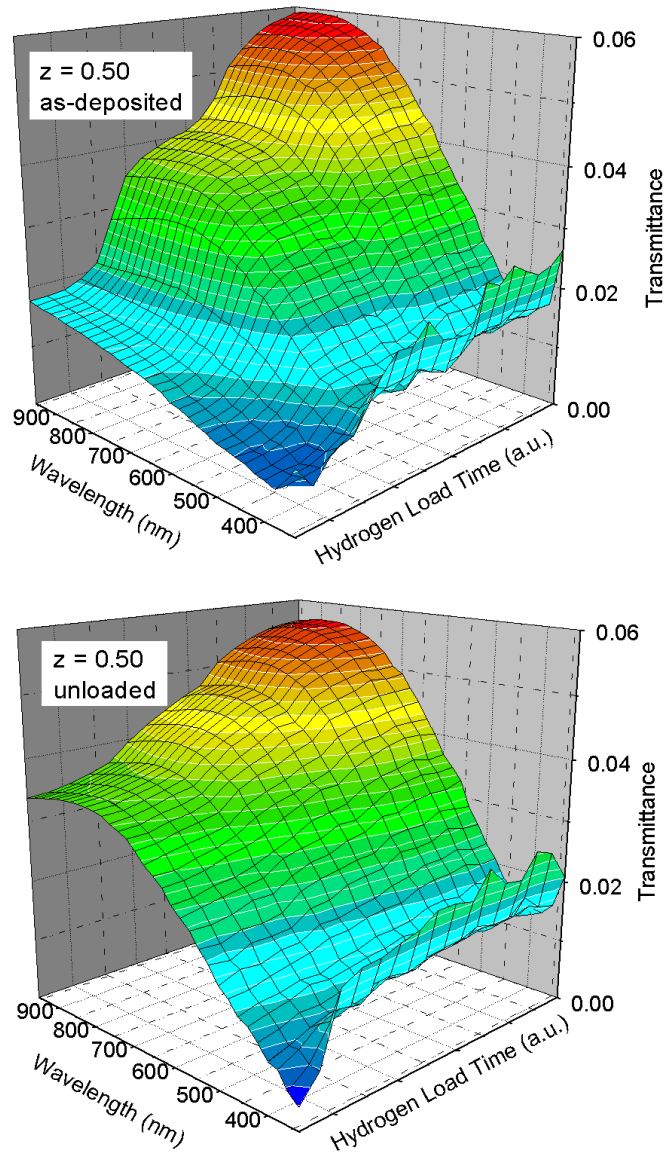


Figure 4.6: Optical transmittance spectra as a function of hydrogen loading time (in arbitrary units) starting from as-deposited (top) and unloaded (bottom) films of  $Y_{0.50}Sc_{0.50}H_x$ . The unloaded film is expected to have  $x \approx 2$ . The full loading time scale is typically 1–2 hours.

alloys. In Fig. 4.7, we have plotted the resistivity and transmittance as a function of hydrogen loading time for several alloys. The transmittance is shown for the wavelength of maximum dihydride transmittance. The dihydride transmittance peak generally appears as an individual peak or a shoulder on the transmittance curve. It is indicated by a vertical arrow in the graphs. In this set of plots, alloys with  $z > 0.50$ , show little or no increase in transmittance beyond the dihydride peak indicated, suggestive that hydride formation is maximally  $x = 2$  for these alloys. However, the resistivity increases beyond the dihydride minimum for all alloys with  $z \leq 0.90$ , which suggests that a fractional amount of hydrogen is able to incorporate beyond  $x = 2$ . We compare the transmittance at the  $\lambda = 820$  nm ( $\hbar\omega = 1.51$  eV) for unloaded and fully loaded films of various alloys in Fig. 4.8. The value for  $\lambda$  was chosen because it is the median value of the dihydride transmittance maxima. The difference between loaded and unloaded transmittance for Y is  $\Delta T(\omega) = 0.067$ , where as for  $\text{Y}_{0.80}\text{Sc}_{0.20}$ ,  $\Delta T(\omega) = 0.025$ , and Sc,  $\Delta T(\omega) = 0.0056$ . In this plot a converging trend towards dihydride levels of transmittance is apparent. The scatter in the data may be due to atomic disorder (discussed in the following section) or phase separation.

To make more evident the suppression of optical transmittance, the spectra of fully loaded films for various  $\text{Y}_{1-z}\text{Sc}_z\text{H}_x$  alloys are displayed in Fig. 4.9a and the dihydride spectra are shown in Fig. 4.9b. In Fig. 4.9a, the large decrease in optical transmittance for  $z \geq 0.20$  is apparent, as well as the change in qualitative behavior from trihydride to dihydride with increasing scandium concentration. Similar to what is seen for  $\text{La}_{1-z}\text{Y}_z$  alloys, Fig. 4.9b shows a significant quenching of the dihy-

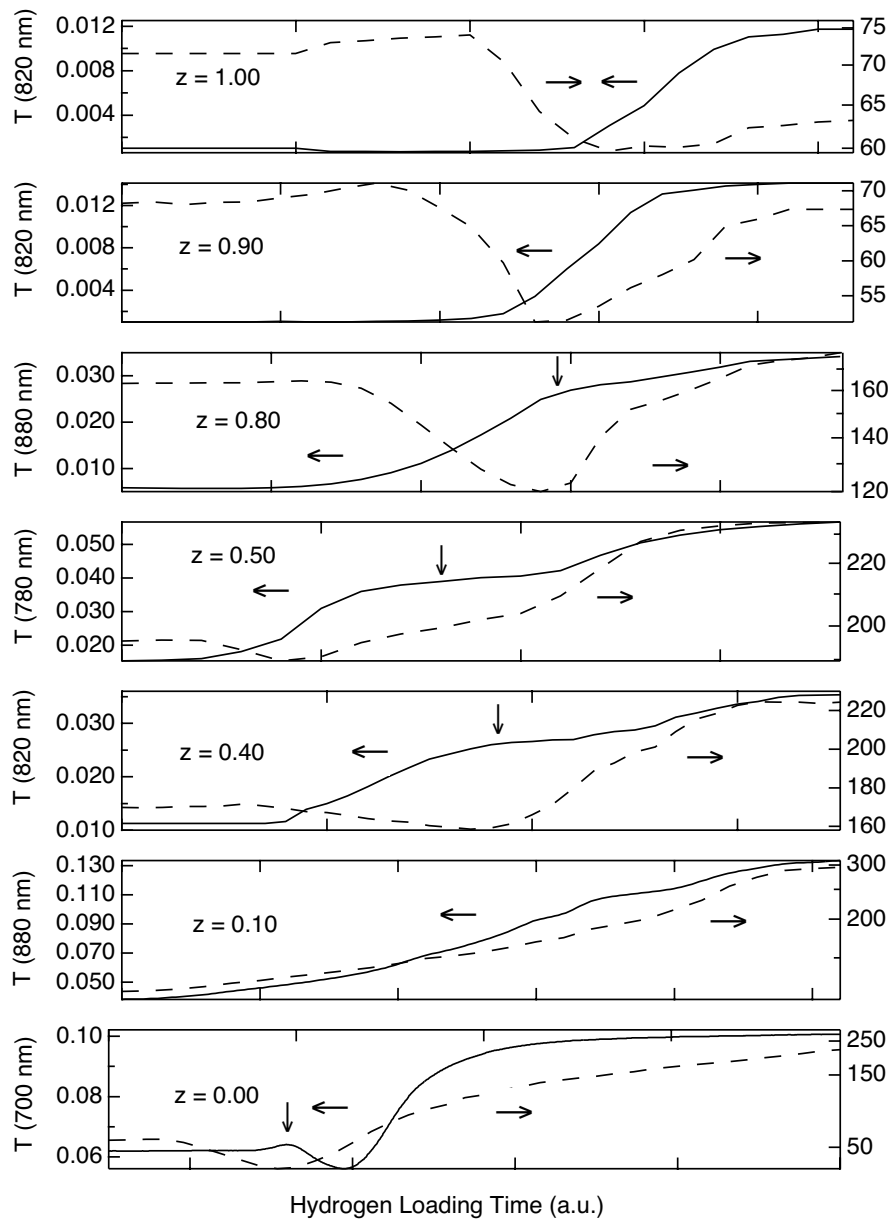


Figure 4.7: Transmittance and ac resistivity as a function of hydrogen loading time. The loading time is arbitrary and has not been scaled in any way. The hydrogen loading time ranged from 10 minutes to 2 hours. The transmittance is plotted for the wavelength of maximum dihydride transmittance. Dihydride transmittance appears as a small peak or a shoulder on the transmittance curve and is indicated by the vertical arrows.

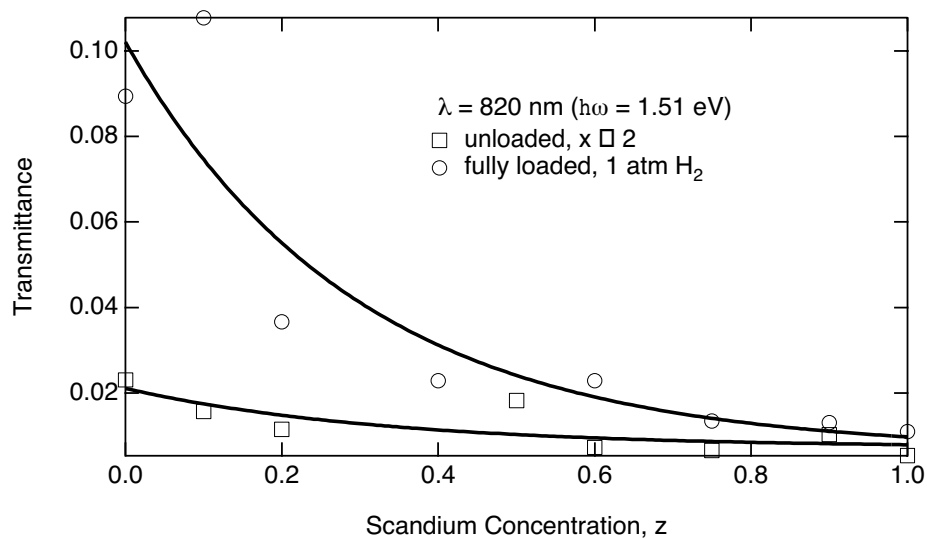


Figure 4.8: Transmittance at  $\lambda = 820 \text{ nm}$  ( $\hbar\omega = 1.51 \text{ eV}$ ) as a function of Sc concentration  $z$ . The amount of transmittance for fully loaded films approaches that of unloaded films (near  $x = 2$ ) with increasing  $z$  indicating a loss of octahedral site occupancy for trihydride formation. The lines are shown to guide the eye. The scatter in the data may be due to atomic disorder effects or phase separation.

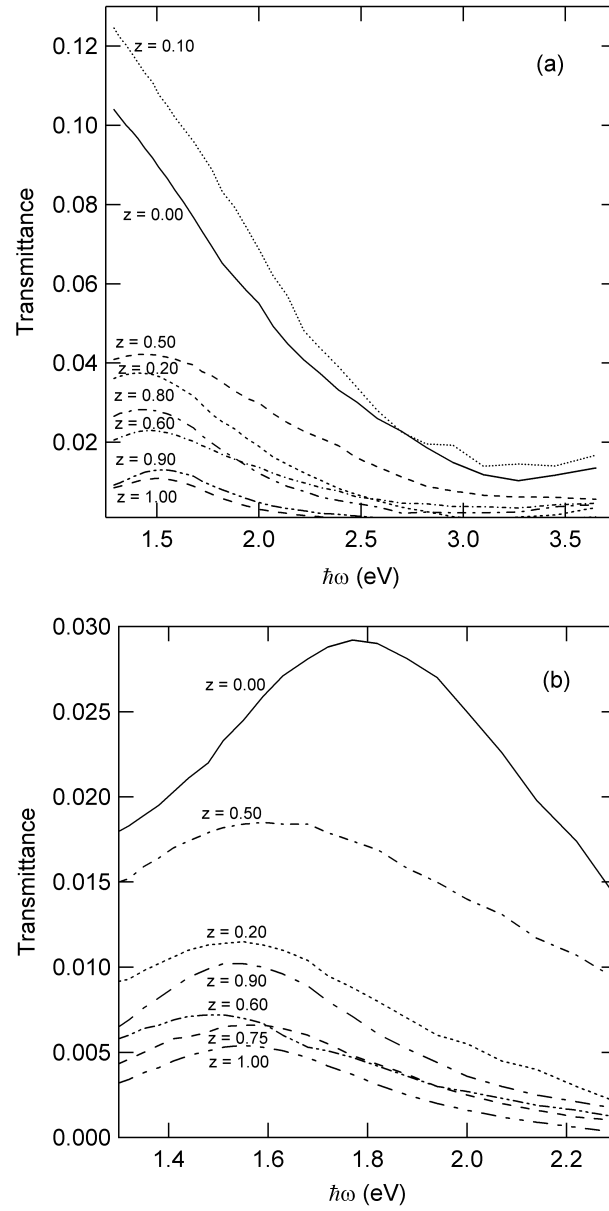


Figure 4.9: (a) Fully hydrogen loaded and (b) unloaded (near  $x = 2$ ) film optical spectra showing transmittance maxima dependence on alloy composition.

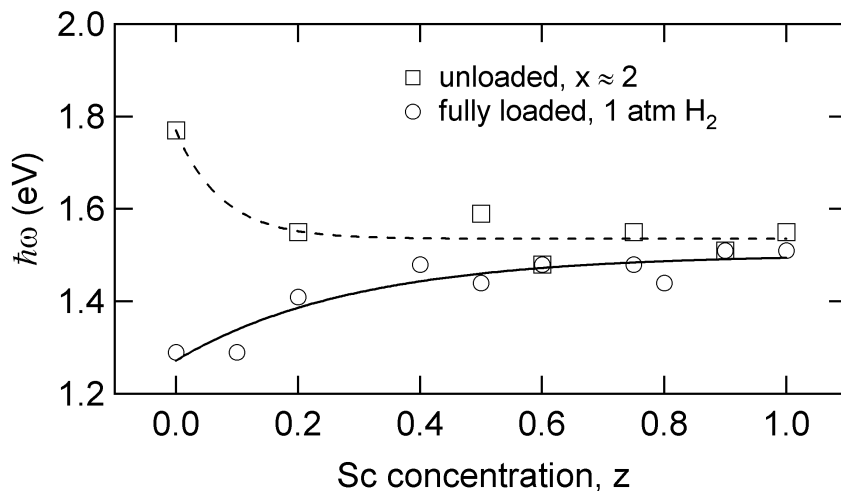


Figure 4.10: Energy of maximum transmittance (for the range  $1.29 \leq \hbar\omega \leq 3.65$  eV) as a function of Sc concentration,  $z$ . The transparency energy of the fully loaded films approaches that of the unloaded films (near  $x = 2$ ) as  $z$  increases. The lines are shown to guide the eye. The scatter in the data may be due to atomic disorder effects.

trihydride transparency window as well as a shift to lower energies as a function scandium content. Comparing the energy of maximum transmittance in Fig. 4.10, one sees that the behavior of the fully loaded films approaches that of the unloaded ( $x \approx 2$ ) films for increasing  $z$ . This convergence occurs primarily above  $z = 0.20$ , where trihydride formation is no longer possible. Interestingly, the unit cell volume we calculate from XRD lattice parameters for  $z = 0.20$  is  $V_{cell} = 3\sqrt{3}a^2c/2 = 176.63 \text{ \AA}^3$ , which is equal to that of Lu, the largest dihydride-maximally-forming rare-earth.

From Fig. 4.9, one can linearly extrapolate the transmission edge to zero transmittance to get an idea of the optical gap energy. This would result in an estimation of 2.7–2.9 eV for  $z = 0.00$  and 0.10. To calculate a more accurate number, analysis can be made using the absorption coefficient,  $\alpha(\omega)$ , derived by

Lambert and Beer, where frequency-dependent transmittance is

$$T(\omega) = T_o \exp[-\alpha(\omega)d]. \quad (4.1)$$

The rare-earth film thickness is denoted  $d$ , and  $T_o$  is a parameter which contains absorptions of the Pd and substrate layers and reflections due to interfaces. If the bands are parabolic, then,  $\alpha(\omega)$  has the form [61]

$$\alpha(\omega) = C \frac{(\hbar\omega - E_g)^\nu}{k_B T} \quad (4.2)$$

where  $C$  is a fit parameter and  $\nu = 2$  for an allowed, indirect gap [60]. Values for  $\nu$  that would indicate an allowed, direct gap (1/2), forbidden, direct gap (3/2), and forbidden, indirect gap (3) did not result in good fits to the data. Results from fits are plotted in Fig. 4.11 and parameters of the fits are shown in Table 4.1. The optical gap is approximately the same for  $z = 0.00$  and  $z = 0.10$ , with a value of 3.3 eV. The value for the gap decreases for alloys with  $0.20 \leq z \leq 0.40$ . In the region of disproportionation, the gap again increases due to the contribution from  $\text{YH}_3$ . For alloys with  $z > 0.60$ , the gap energy again decreases. The value for the optical gap in  $\text{YH}_3$  is approximately 15% larger than the value found by van Gogh [6]. This difference may be attributable to differences in film thicknesses, grain structure, or spectroscopic sensitivity.

## 4.3 Electrical Resistivity

### 4.3.1 Room Temperature Measurements

Room temperature resistivity measurements made simultaneously with spectroscopic measurements reveal a concentration-dependent transition. Resistivity for

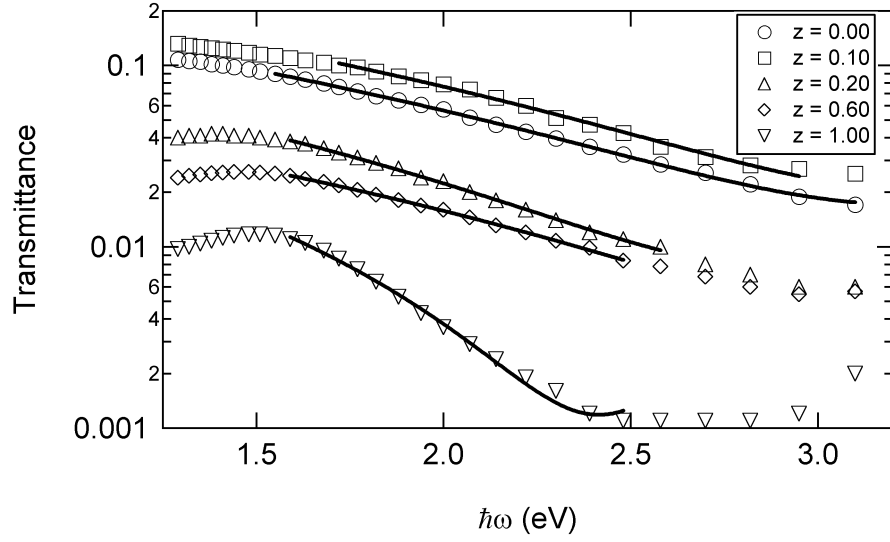


Figure 4.11: Lambert-Beer fits to the transmission edge.

**Optical Transmission Edge Fit Parameters**

$z$	$T_o$	$C$	$E_g$ (eV)	$\chi^2$
0.00	$1.71 \pm 0.06 \times 10^{-2}$	$-6.34 \pm 0.16 \times 10^{-5}$	$3.25 \pm 0.03$	$6.02 \times 10^{-6}$
0.10	$2.00 \pm 0.04 \times 10^{-2}$	$-8.07 \pm 0.92 \times 10^{-4}$	$3.32 \pm 0.12$	$4.59 \times 10^{-5}$
0.20	$7.71 \pm 0.80 \times 10^{-3}$	$-4.50 \pm 0.30 \times 10^{-4}$	$2.90 \pm 0.06$	$2.04 \times 10^{-6}$
0.60	$3.81 \pm 0.92 \times 10^{-3}$	$-1.84 \pm 0.15 \times 10^{-4}$	$3.28 \pm 0.10$	$2.91 \times 10^{-7}$
1.00	$1.19 \pm 0.11 \times 10^{-3}$	$-3.72 \pm 0.20 \times 10^{-4}$	$2.42 \pm 0.02$	$4.68 \times 10^{-7}$

Table 4.1: Fit parameters from the Lambert-Beer model of the transmission edge for  $Y_{1-z}Sc_zH_{3-\delta}$ .



several alloys is plotted in Fig. 4.12. Assuming the two-layer films act as parallel resistors of rare-earth and palladium,  $R_{RE/Pd} = R_{RE} \cdot R_{Pd} / (R_{RE} + R_{Pd})$ , we are able to extract the rare-earth layer resistivity. We measured the resistivity of Pd to be 27–29  $\mu\Omega\cdot\text{cm}$ , for all hydrogen concentrations. The resistivity calculated for yttrium is  $\rho \approx 73 \mu\Omega\cdot\text{cm}$ , and for Sc,  $\rho \approx 91 \mu\Omega\cdot\text{cm}$ . These values are larger than bulk literature values likely due to lattice defects, small grain size, and the deposition-incorporated hydrogen mentioned previously. For yttrium, bulk resistivity has been reported as 59  $\mu\Omega\cdot\text{cm}$  [54], and scandium bulk resistivity is 52–70  $\mu\Omega\cdot\text{cm}$ , depending on purity [54, 44]. As the scandium content is increased the metal to insulator transition that occurs between the dihydride and fully hydrogenated phases decreases until, in scandium, the resistivity remains at the dihydride minimum. This is to be expected, since yttrium was previously known to have a metal to insulator transition for this range, while scandium maximally incorporates only two hydrogen per scandium atom. Due to the similarities in electronic structure with yttrium, one would expect  $\text{ScH}_2$  to be more metallic than pure Sc. Our measurements and literature support this expectation [17, 43, 44]. Again assuming the parallel resistance model for our two-layer system, the resistivity of the active, rare-earth layer when fully hydrogenated ( $x \approx 3$ ) of  $z = 0.00$  and  $z = 0.10$  is estimated to be 500–1000  $\mu\Omega\cdot\text{cm}$ . This is an increase of up to an order of magnitude in resistivity. The hydrogen loading time (x-axis) for the measurements in Fig. 4.12 have been scaled such that the dihydride minimum is at the same time.

In addition to the scandium dependent transition to more metallic behavior, large disorder effects due to alloying have been found in the electrical transport

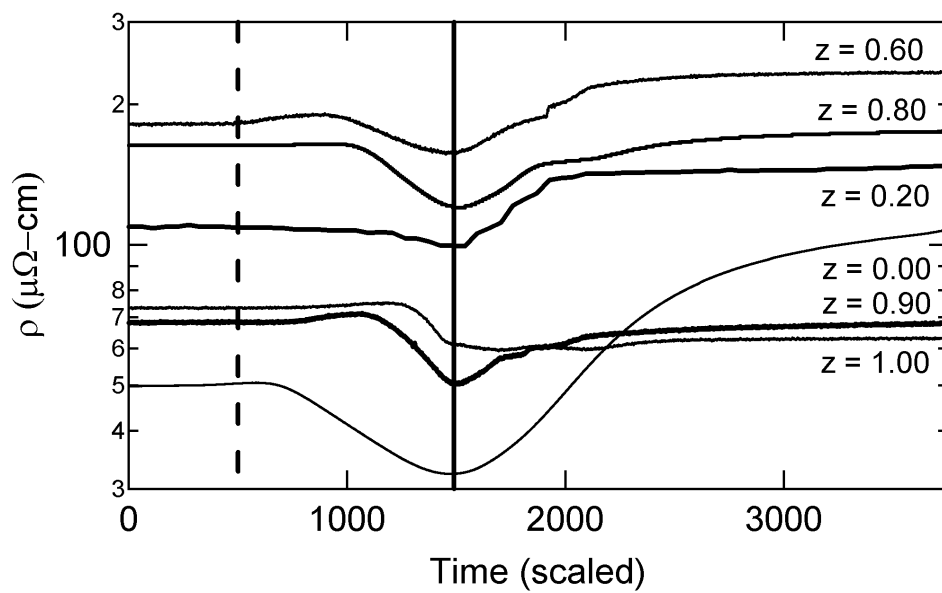


Figure 4.12: Room temperature resistivity of several alloys as a function of hydrogen loading time in arbitrary units. The data has been scaled so that the dihydride minimum is at the same time. The transition from the dihydride minimum to trihydride maximum reduces with concentration until, in scandium the resistivity stays in the dihydride minimum.

properties. This is observed for most metal-alloy systems with large differences in atomic radii, and has been reported for  $\text{La}_{1-z}\text{Y}_z$  also [25]. The disorder can be modeled as

$$\rho(z) = [\rho_Y + (\rho_{Sc} - \rho_Y) \cdot z] + 4\rho_{do} \cdot z(1 - z), \quad (4.3)$$

where  $\rho_Y$  and  $\rho_{Sc}$  are the measured yttrium, scandium resistivities, and  $\rho_{do}$  is the contribution due to alloy disorder effects. These values are uncorrected for the palladium capping layer. Figure 4.13, plots the measured room temperature resistivity values for as-deposited and dihydride resistivities as marked by the vertical lines in Fig. 4.12. As shown, we find that the disorder fits this equation well with a maximum near the middle of the alloy phase diagram. The disorder scattering contributes  $121.6 \mu\Omega\cdot\text{cm}$  for  $x = 0$  and  $112.4 \mu\Omega\cdot\text{cm}$  for  $x = 2$ . These values are approximately twice that of the parent metals indicating that phonon scattering may be comparable to conduction-electron scattering by impurities. However, since the fit to the disorder equation is good, effects which typically obscure disorder effects, such as concentration inhomogeneities, oxidation effects, and film thickness variations can be ruled out. Curzon and Singh showed that oxide contamination due to film thickness is overcome for films with thickness  $d > 90 \text{ nm}$  [49]. There is always an exception to the rule as shown by the  $z = 0.10$  alloy. The as-deposited alloy fits reasonably to the disorder; however, the unloaded film, expected to be dihydride, exhibits resistivity much greater than one would expect from the disorder function. Although it is possible that this is a result of grain structure inherent to this admixture, we believe this is further support of stable hydride formation beyond dihydride i.e.,  $x > 2$ .

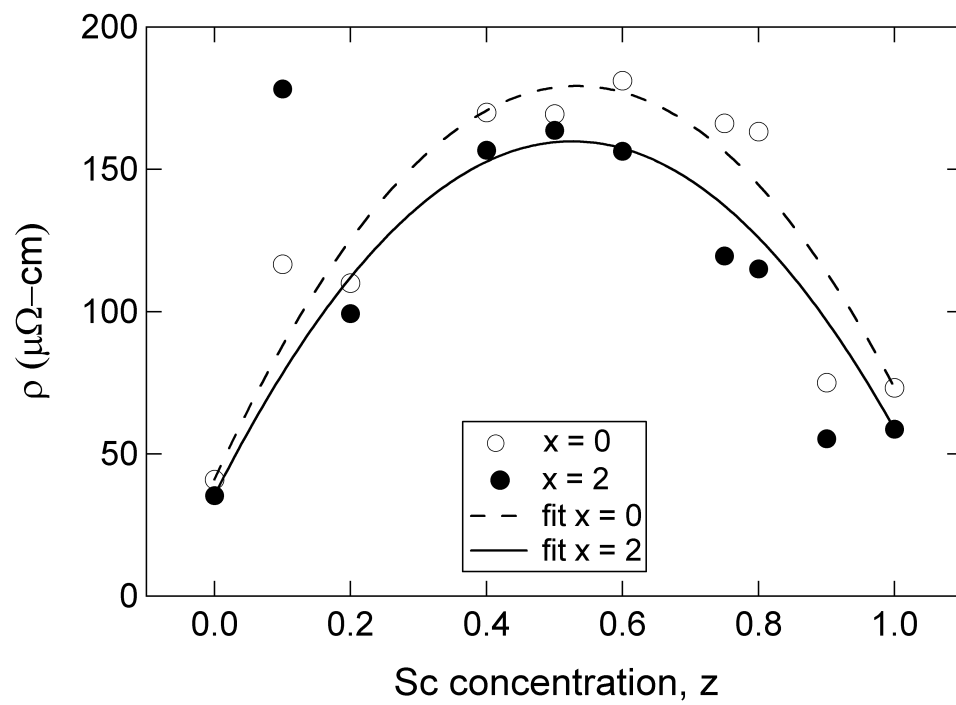


Figure 4.13: Modeling of disorder in room temperature electrical resistivity from Eqn. 4.1.

One can determine whether surface effects due to film thickness should be observed. These contributions typically occur for films of thickness on the order of the electron mean free path,  $d \approx \lambda_{mfp}$ . The electron mean free path is  $\lambda_{mfp} = v_F \tau$ . The Fermi energies for yttrium and scandium are taken from the band structure models of Altmann and Bradley [55]. These values are  $\epsilon_F(\text{Y}) = 4.58$  eV and  $\epsilon_F(\text{Sc}) = 5.98$  eV. Scandium fermi surface calculations have also been reported by Fleming and Loucks [56] with a value of  $\epsilon_F(\text{Sc}) = 5.66$  eV. Then, the Fermi velocities may be estimated to be,  $v_F(\text{Y}) = 1.3 \times 10^6$  m/s and  $v_F(\text{Sc}) = 1.5 \times 10^6$  m/s. From our resistivities, we estimate  $\tau$  using the Drude model and obtain  $\tau = m/ne^2\rho = 1.6 \times 10^{-15}$  s for yttrium and  $\tau = 9.1 \times 10^{-16}$  s for scandium. From these values we compute a mean free path of  $\lambda_{mfp} = 2.0$  nm in yttrium and  $\lambda_{mfp} = 1.3$  nm in scandium. Therefore, our films have  $d \gg \lambda_{mfp}$ , and surface effects are not expected to have an affect on resistivity measurements. This is in agreement with findings for the La-Y system [6].

Finally, because the fit to the disorder model is good, and the mean free path of electrons is much smaller than the film dimensions, we can conclude that the alloy resistivities are dominated by impurity scattering with length scales on the order of several atomic lengths.

### 4.3.2 Temperature-Dependent Measurements

To get a better understanding of the electrical behavior discussed in the previous section, we have measured the temperature dependent ac resistivity for the temperature range 4–295 K. Results for the unloaded, nearly dihydride concen-

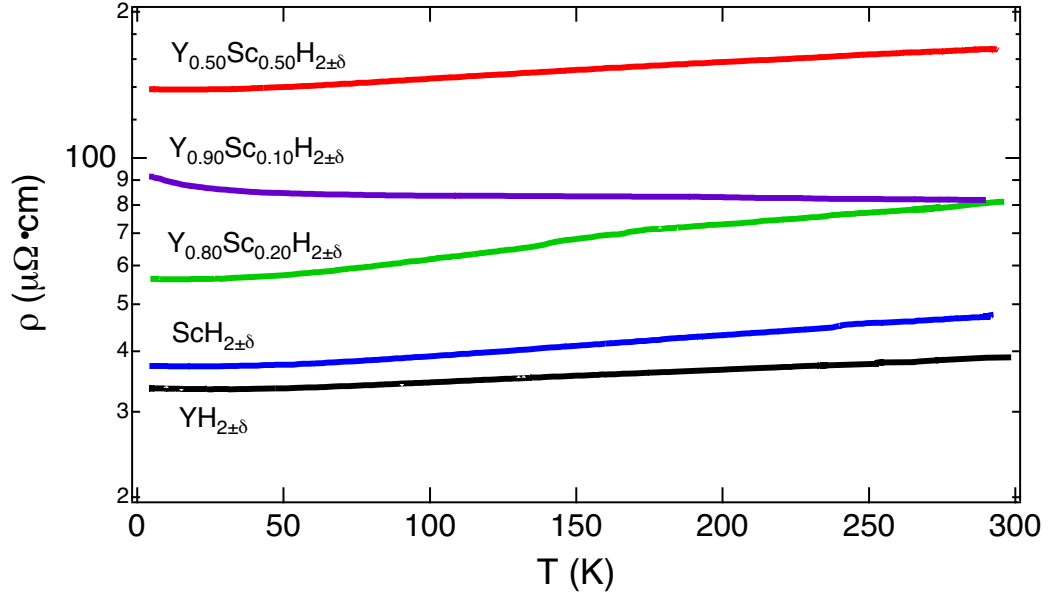


Figure 4.14: Temperature dependence of the ac resistivity for dihydrides of several alloys. All show metallic behavior with the exception of  $\text{Y}_{0.90}\text{Sc}_{0.10}$ .

trations of several alloys are shown in Fig. 4.14. It is important to note that the 10 nm of palladium deposited to protect the rare-earths is thick enough to form a continuous film, rather than islands. Therefore, the temperature dependence has a metallic contribution from the palladium. Previously, it was mentioned that  $\text{ScH}_2$  is expected to be metallic based on literature and measurements made in this study. Figure 4.14 shows metallic behavior for this film. In fact, all alloys measured exhibited metallic behavior in the nearly dihydride composition with the exception of  $z = 0.10$ . Interestingly, the  $z = 0.10$  alloy was insulating for all hydrogen concentrations measured. This is consistent with the spectroscopic data, which showed some transmittance for this alloy regardless of hydrogen content.

Temperature dependent resistivity was also measured on the fully hydro-

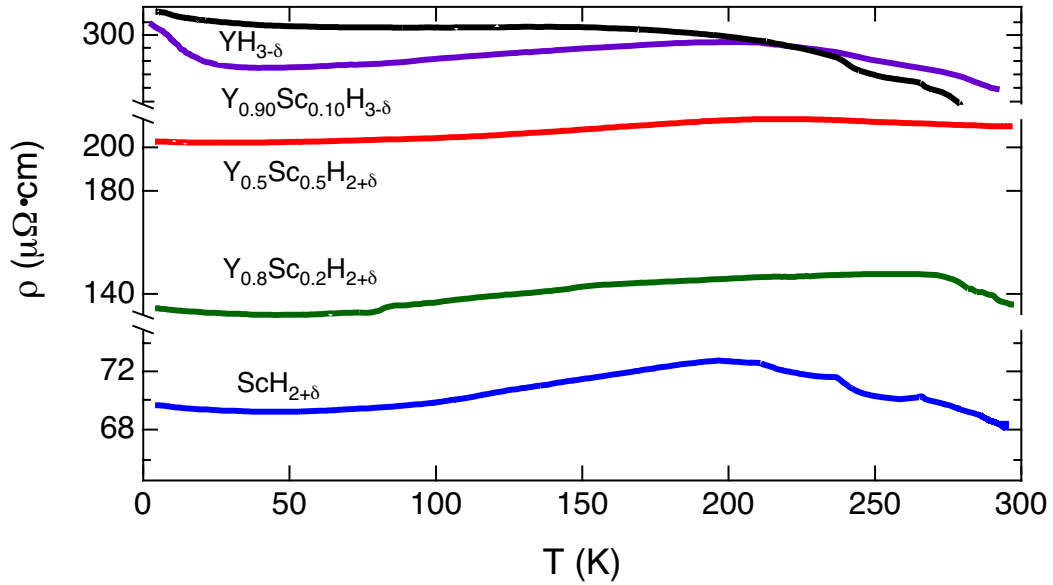


Figure 4.15: Temperature dependence of the ac resistivity for fully hydrogenated (295 K; 1 atm  $H_2$ ) films of the same alloys as Fig. 4.14.  $YH_{3-\delta}$  and  $Y_{0.90}Sc_{0.10}H_{3-\delta}$  indicate insulating behavior at low temperatures with an up-turned resistivity. A transition occurs from  $z = 0.10$  and  $z = 0.20$  supporting the spectroscopy results.

generated films. The films are first loaded in one atmosphere of hydrogen at room temperature (295 K) until the resistivity saturates to a constant value. Figure 4.15 plots data for  $z = 0.00, 0.10, 0.20, 0.50,$  and  $1.00$ . For all alloys measured, we find that the resistivity behaves as seen in the literature on bulk La and Y thin films above 150 K. Between 300 and 150 K, the resistivity transitions through a maximum. This has been attributed to localization of octahedral hydrogen vacancies acting as a donor-like defect band [53]. Above this transition temperature, the resistivity is characterized by thermally activated transport, roughly linear in  $T$ . Below the transition region, there is an alloy concentration dependence found. For  $z = 0.00$ , the range of 50–150 K is best fit by  $\rho \propto \ln(T)$ . Figure 4.16 is plotted to show this

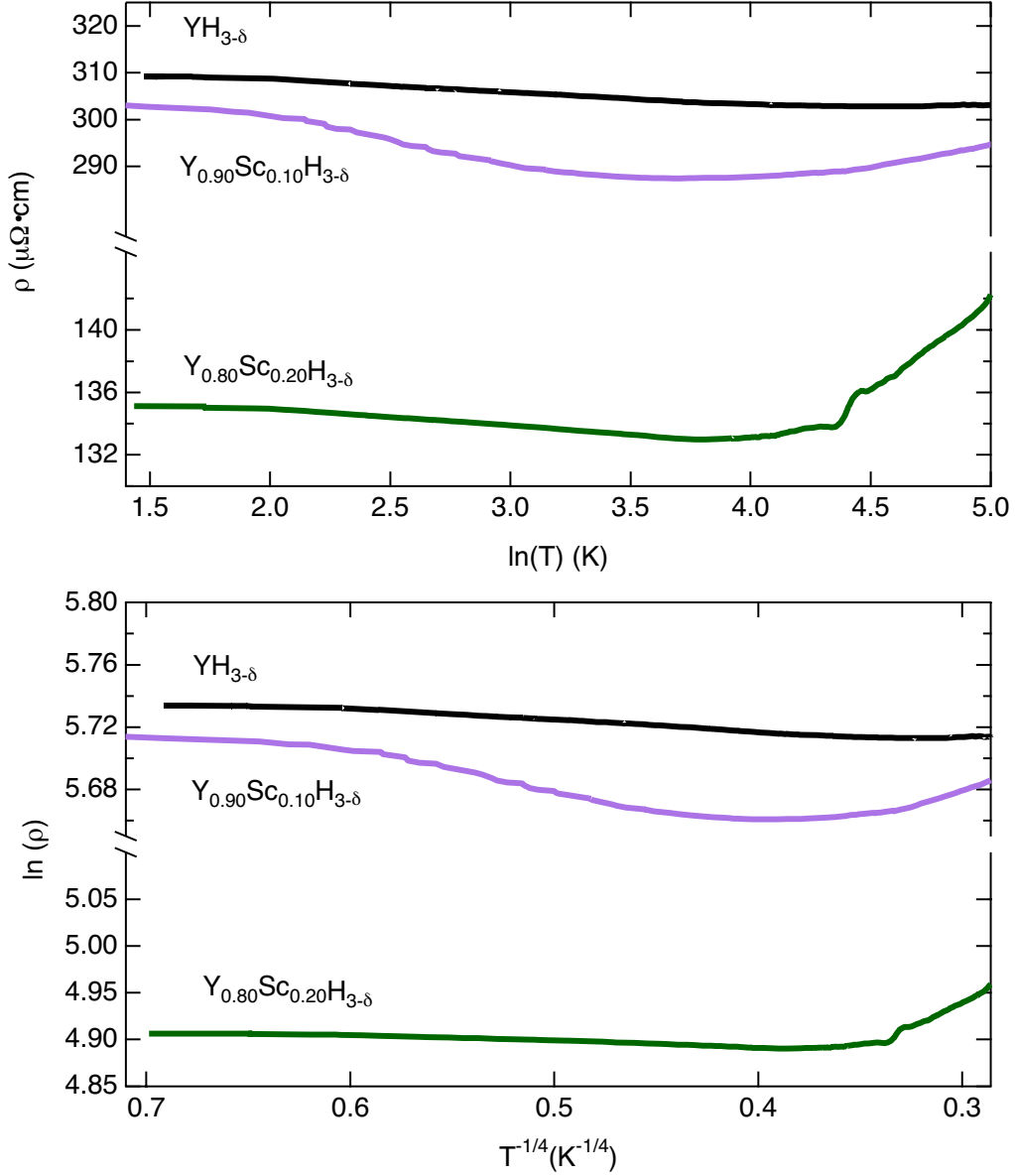


Figure 4.16: Temperature dependence of the resistivity over the range 4–150 K. The top graph shows that, for 50–150 K,  $\text{YH}_{3-\delta}$  is most linear when plotted as  $\rho$  vs.  $\ln(T)$ , while in the bottom plot,  $\text{Y}_{0.90}\text{Sc}_{0.10}\text{H}_{3-\delta}$  and  $\text{Y}_{0.80}\text{Sc}_{0.20}\text{H}_{2+\delta}$  show linear behavior only at lower temperatures (4–20 K) when plotted as  $\ln(\rho)$  vs.  $T^{-1/4}$ , indicating a variable range hopping model.



linear dependence. This has been observed previously by Huiberts *et al.* [36]. It is believed that this is attributable to one of two mechanisms. Kondo scattering is one possibility. Hydrogen vacancies introduce magnetic moments due to the H<sup>-</sup> nature of hydrogen in yttrium [23]. These act as scatterers inducing a spin-scattering resistivity term that depends logarithmically on temperature. The implications of Kondo scattering are that local magnetic moments appear as one approaches the metal-insulator transition. Hall effect measurements by Huiberts *et al.* [36], reveal a quadratic, negative magnetoresistance consistent with the presence of the Kondo effect. Another suggestion for the logarithmic temperature dependence is in terms of 2D weak electron localization. In this model, the film is stratified into layers of conducting YH<sub>2</sub> and insulating YH<sub>3</sub>. The spacing between layers is comparable to the *c*-axis lattice spacing. Since the slope of the logarithmic dependence will depend on spin scattering and disorder effects of electron interactions, the observed behavior would not be inconsistent with 2D localization. In the reference by Huiberts, one can extract the trihydride deficiency from,

$$R^{\square}(50\text{K}) = \frac{788}{\delta}(0.32 - 2.1\delta). \quad (4.4)$$

In this equation,  $R^{\square} = \rho/d$ , where  $d$  is the film thickness. The choice of 50 K comes from the minimum temperature of the logarithmic dependence. We find  $\delta = 0.15$ , which is reasonable for the observed behavior.

The  $z = 0.10$  and  $0.20$  alloys are poorly fit by the  $\rho \propto \ln(T)$  over the 50–150 K range; however, at lower temperatures (4–20 K), all measured alloys can be fit to  $\ln(\rho) \propto T^{-1/4}$ . This is indicative of variable range hopping (VRH) seen in many

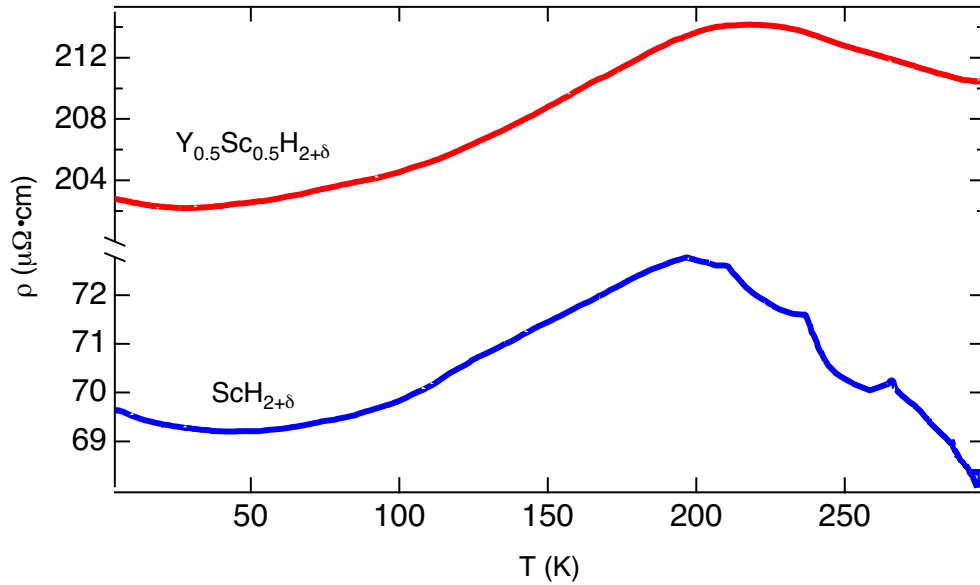


Figure 4.17: Temperature dependence of alloys with  $z > 0.20$ . Qualitatively the data is similar for all alloys with  $z \geq 0.20$ . The low temperature up-turn is best modeled with a Mott transition ( $T^{-1/4}$ ).

insulators. The  $T^{-1/4}$  power law implies a Mott insulator where the insulating gap is governed by thermally activated hopping processes. Electrons are able to hop to nearby states of slightly different energies by absorption of phonons, or the electrons may hop to more distant sites provided the energy is very close to the original energy state. The hopping distance is, therefore, related to the difference in energy between the initial and final states.

Qualitatively, all alloys with  $z \geq 0.20$  have similar temperature dependent resistivities. They are distinguished mainly by the alloy disorder discussed in the previous section. The resistivity is largely metallic below the localization peak near 200 K. A small impurity-like tail at low temperatures is observed. The deviation

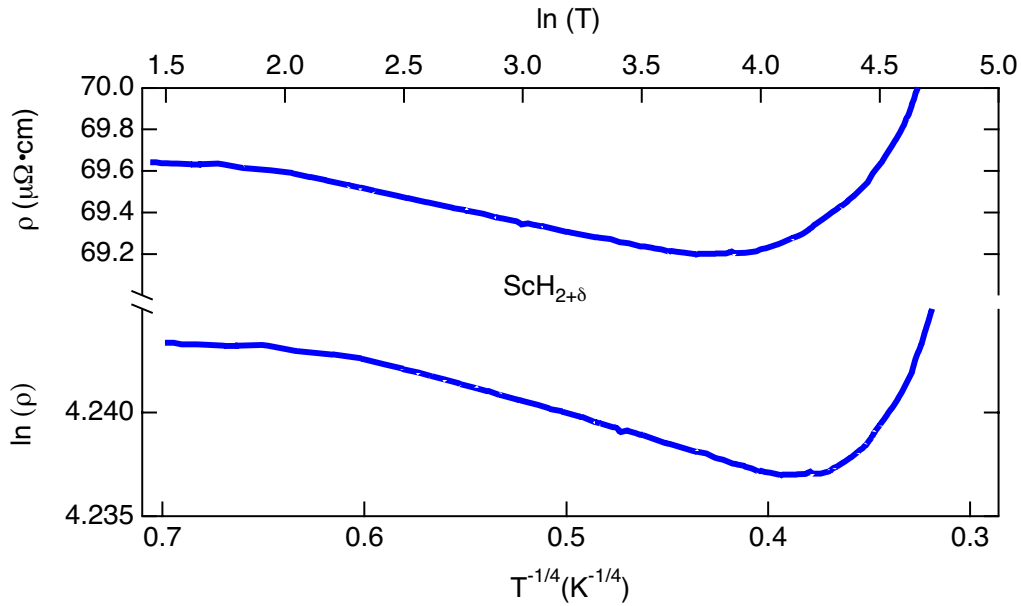


Figure 4.18: Scandium resistivity for 4–50 K. The data is plotted as  $\rho \propto \ln(T)$  on top and  $\ln(\rho) \propto T^{-1/4}$  on bottom. The best agreement is with the Mott model.

from monotonic behavior in the  $z = 1.00$  data around 250 K is due to a temporary fluctuation in hydrogen pressure. The resistivity of scandium is plotted in Fig. 4.18, which shows the temperature dependence below 8 K can be fit to  $\ln(\rho) \propto T^{-1/4}$ .

Several hydrogen concentrations near the fully loaded state were measured for most alloys in order to observe transitions between the metallic dihydride and insulating trihydride. It was observed that trihydride-forming films left in an overpressure ( $\approx 1$  psi) of hydrogen for more than 24 hours would shunt the active layer, and effectively, one would simply measure the palladium capping layer. This can be seen in both  $\text{YH}_{3-\delta}$  plots of Fig. 4.19. The upper curve is data for a film soaked in an overpressure of hydrogen over 2 days. The behavior is metallic below the localization temperature, and the low-temperature resistivity is equivalent to the lower

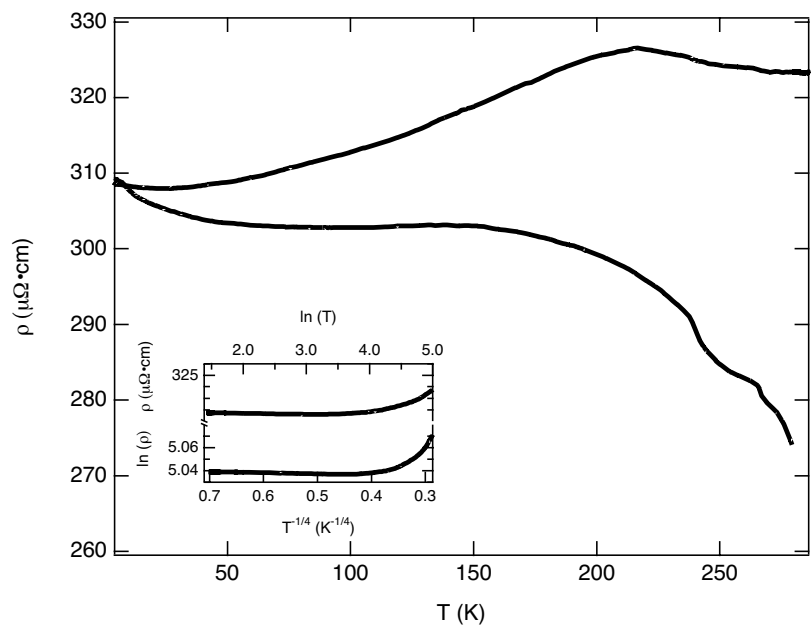


Figure 4.19: Films of  $\text{YH}_{3-\delta}$  showing a temperature induced shunt and a hydrogen content induced shunt. These resistivities are calculated assuming a film thickness of 110 nm. The resistivity near 4 K is equivalent to that of palladium when calculated for a 10 nm film.

curve, where the yttrium resistance becomes so large at low temperatures that the resistivity saturates at a value that is, for a 10 nm Pd film, consistent with measured palladium resistivities ( $\rho_{PdH_x} \approx 29 \mu\Omega\cdot\text{cm}$ ). The inset is the same data as the upper curve plotted to show that for the metallic behavior of palladium, neither insulating scheme discussed above ( $\ln(T)$  or  $T^{-1/4}$ ) addresses the temperature dependence appropriately. Similar behavior was observed in the  $z = 0.10$  alloys.

#### 4.4 Discussion

The loss of octahedral site occupancy as a function of Sc concentration in  $Y_{1-z}Sc_zH_x$  causes the suppression of the optical switching properties seen in metal trihydrides. Substitution of Sc for Y indicates that there is a minimum cell volume for trihydride forming rare-earth metals around  $177 \text{ \AA}^3$ . For an hcp (or fcc) structure, the combinatorics can be easily calculated to determine the fraction of hydrogen that have a specific number of nearest neighbor scandium atoms. For our samples, we have a lattice with  $N$  octahedral sites each having  $X = 6$  nearest-neighbor lattice sites. For a homogeneous alloy, where the atomic distribution is essentially random, the fraction of octahedrals,  $N_n/N$ , with  $X - n$  yttrium and  $n$  scandium nearest neighbors is

$$\frac{N_n}{N} = \frac{X!}{(X-n)!n!} (1-z)^{X-n} z^n, \quad (4.5)$$

where  $z$  is the scandium concentration as it has been denoted previously. Figure 4.20 plots  $N_n/N$  for scandium concentrations  $0.00 \leq z \leq 1.00$ , in increments of 0.05. The first thing that jumps out is the sharp drop of the fraction of octahedral sites with  $n = 0$  nearest neighbor scandiums. In addition, the fraction with  $n = 1$  becomes

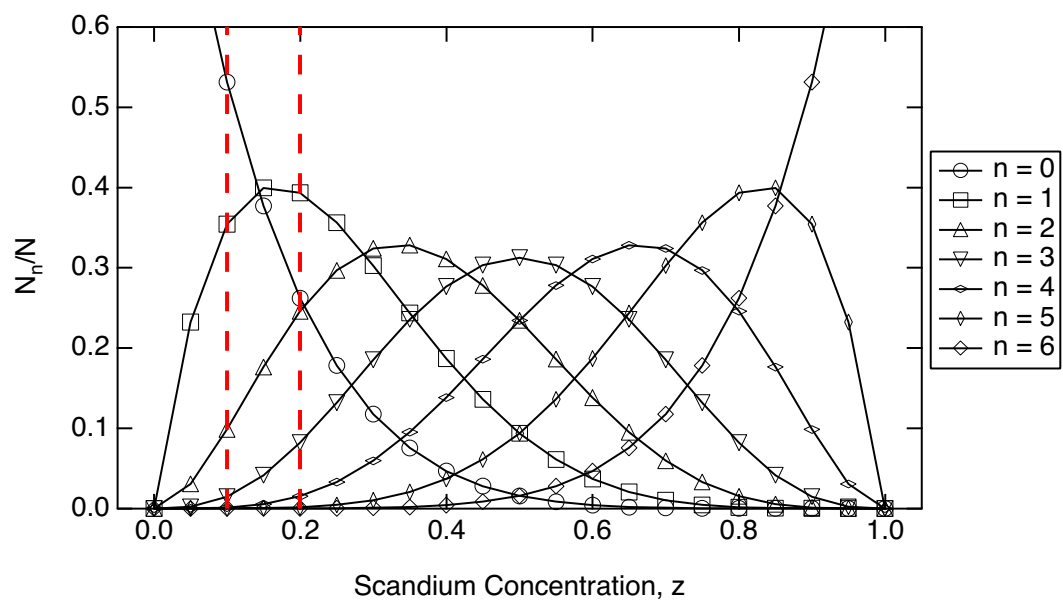


Figure 4.20: A plot of the fraction of octahedral sites that have  $n$  scandium nearest neighbors as a function of scandium concentration. The dashed lines indicate the region where the metallic-mirror to transparent-insulator transition is largely quenched.

significantly smaller for  $z > 0.20$ . If one assumes that it is necessary to have no nearest-neighbor scandium atoms in order to permit octahedral site occupancy, then the expected total hydrogen content for each alloy might be calculated as  $x = 2 + (1-z)N_o/N$ , where  $N_o/N$  is the fraction of octahedral sites with all yttrium nearest-neighbors. A similar calculation can be made if  $n = 0$  and 1 want to be considered. These maximal hydrogen contents are plotted as a function of scandium content in Fig. 4.21. If one assumes that transmittance is directly proportional to the number of hydrogen incorporated beyond the dihydride, equivalent to an assumption that the effective medium has a volume-averaged transmittance, then Eqn. 4.5 can be used to fit the data of Fig. 4.8. Figure 4.22 replots this data with the functional fits described here. As can be seen the result is a reasonable fit, especially for  $n = 0$ . The scatter of the  $z = 0.10$  and  $0.60$  points have been discussed previously.

Studies of pressure-composition isotherms for bulk Y-Sc hydrides support our stoichiometry conclusions. In bulk powders, Lieberman and Wahlbeck find hydrogen deficient trihydrides for  $0.00 \leq z \leq 0.40$  similar to our calculated concentrations. The values for bulk are approximately 10% less due to the difficulty to fully hydrogenate bulk powders [7]. In addition, the immiscibility of the dihydrides has been observed in the same work. This was attributed to the large differences in atomic radii. Thermodynamically,  $YH_2$  is more stable than  $ScH_2$ . The hydrogen tend to reside near yttrium atoms, creating a  $YH_2/ScH$  mixture until the dihydride filling is completed. In alloys with near equal proportions of each metal, phase separation would be expected due to stresses induced from lattice expansion in  $YH_2$  before formation of  $ScH_2$ . The phase diagrams of Fig. 4.23 are obtained from results

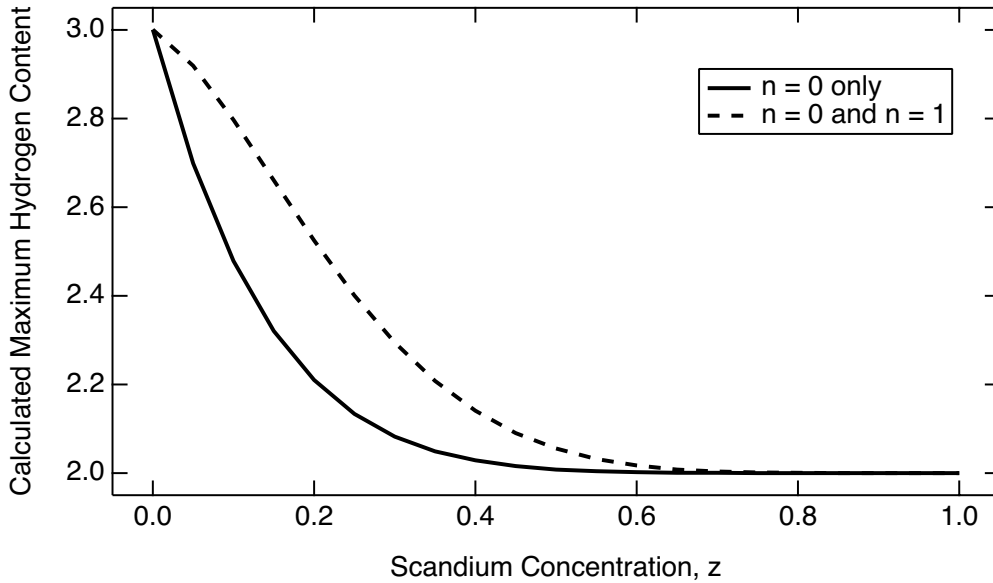


Figure 4.21: Expected maximum hydrogen content as calculated from data observations and the combinatorics of Fig. 4.20.

of this study and using the maximal hydrogen concentration calculated as discussed above. The shaded region is the region where a solid-solution phase exists. The region between the two dashed lines indicate possible phase separation observed after hydriding the alloys.

It is not surprising that we observe the suppression of optical switching at the scandium concentration of  $z = 0.20$ . Unlike the Y-Mg system with the optical shutter effect, the Y-Sc system does not have enhanced transmittance in regions of phase separation. This is to be expected since  $\text{ScH}_2$  is metallic, in contrast to  $\text{MgH}_2$ , which is insulating. It is the insulating character of  $\text{MgH}_2$  that enhances the optical band gap. What is not clearly understood is the apparent metal-insulator transition that occurs for the unloaded, presumed dihydride  $\text{Y}_{0.90}\text{Sc}_{0.10}$  composition.



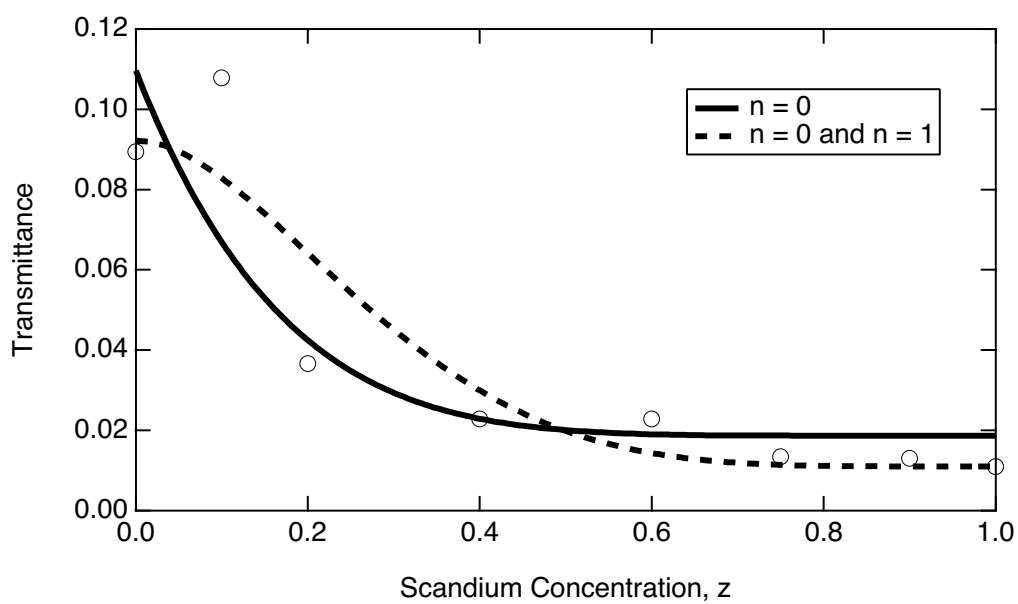


Figure 4.22: Revisiting the data of Fig. 4.8, the fully loaded transmittance as a function of scandium content has been fit in proportion to the hydrogen content predicted by restricting octahedral occupancy to sites with  $n = 0$  or  $n = 0$  and 1 nearest-neighbor scandiums.

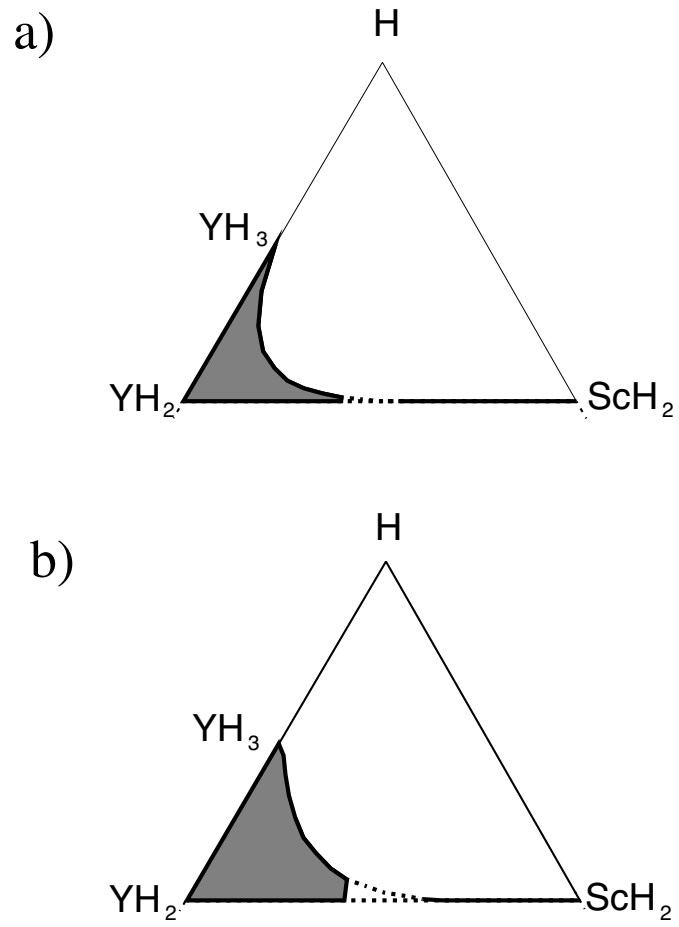


Figure 4.23: Phase diagrams for the 3-element system with the maximal hydrogen contents calculated from the model discussed in the text. a) assumes  $n = 0$  and b)  $n = 0$  and 1.

It may be that this composition forms a trihydride phase that is more stable than other alloy compositions studied. This is in accord with our lack of observation of a dihydride transmittance peak. The possibility of an unusually stable trihydride phase may be useful for applications such as pixel-switching in flat-panel displays, where remaining closer to the phase transition might reduce switching speeds, which are currently an order of magnitude too large.

## Chapter 5

### Summary and Future Investigations

*“That rug really tied the room together... did it not?... did it not?”*

*- Walter in The Big Lebowski*

The change in optical properties of the  $Y_{1-z}Sc_zH_x$  system is due to reduction of the unit cell volume of approximately 30%. Up to the dihydride phase, hydrogen in yttrium primarily fills the tetrahedral sites. Typically up to  $x = 2$ , only a few atomic percent of hydrogen occupy octahedral sites, which have higher mobility than tetrahedral sites [15]. Because the transition occurs beyond the dihydride phase, when octahedral sites become significantly occupied, it is assumed that this filling is responsible for the optical transition. Therefore, in the yttrium-scandium alloys, the quenching of the optical transmittance is most likely due to the loss of available octahedral sites caused by the reduction of lattice dimensions. In the  $Y_{1-z}Sc_zH_x$  we have studied, the optical and metal to insulator transitions are largely suppressed for scandium concentrations above  $z = 0.20$ . It is interesting to note that the unit cell volume we measure for  $Y_{0.80}Sc_{0.20}$  ( $176.63 \text{ \AA}^3$ ) is equal to the unit cell volume of lutetium ( $V_{Lu} = 176.64 \text{ \AA}^3$ ), the largest known rare-earth element that does not form a trihydride. This suggests that studies on the  $Y_{1-z}Lu_zH_x$  alloy system would be very interesting, and the lutetium  $5d^16s^2$  electronic structure make it simple

to correlate results to these studies. We have also identified a metal to insulator transition between Y and  $Y_{0.90}Sc_{0.10}$ , apparently in the middle of the the transition from an optically switchable material to a non-switchable material.

From statistical modeling it was found that  $z = 0.20$  is not an unexpected concentration beyond which to observe the optical switching to be quenched. Further study of the alloy phase diagram for the transition region  $0.00 < z < 0.20$  is underway. It is important that the phase separation be better identified. Two possible directions for this study have been planned. The first is to use substrate heating, which will increase the crystallinity of the films. This would provide better XRD for analysis. Another regime for the study of phase separation is to investigate epitaxial films. Epitaxial materials provide an extremely simple way to identify phase separation, as well as additional effects, for example, epitaxial strain from a substrate or buffer-layer. Design, construction, and installation of the equipment to enable these two capabilities have been initiated by the author. In addition, x-ray diffraction capabilities for fully hydrided films should also be developed along with electrochemistry for hydrogen loading. Electrochemical loading enables the determination of hydrogen concentration. Finally, modifications of an AFM and/or STM head to permit topographical and spectroscopic studies during hydrogen loading would provide complementary microscopic information.

## Appendices

## Appendix A

### Vacuum and Film Deposition

Much of the following material was written in my Master's thesis, however, at that time I still had not grown a single film [74]. I have since had much experience with the chamber. This is an updated user's guide to growing thin films using e-beam evaporation. I will avoid discussions of the evaporators, power supplies, pumps, substrate stage, and leak detection because I feel my past thesis is adequate for these topics.

#### A.1 Growing a Film

The vacuum chamber is designed such that it is able to sustain vacuum pressures of  $10^{-10}$  torr or better. However, to date, ultimate pressures on the order of  $10^{-8}$  have been achieved. The current mode of operation is to break vacuum about once a week to change evaporant material for a new set of films. This is partly why the chamber pressure is not optimal. There is also likely a leak in this range that should be sealed. The metal-hydrides did not require lower pressures, and I therefore forewent further leak detection.

Since my Master's thesis, we have purchased a new dry pumping station which requires only a flick of a switch (once the chamber is sealed). The station will bring the chamber to  $\approx 10^{-5}$  torr within one hour and  $10^{-7}$  torr overnight. At  $10^{-5}$

torr, the ion gauge can be turned on (making sure it is on the lowest,  $10^{-4}$ , scale). When the chamber reaches  $10^{-6}$  torr, the ion pump should be turned on in “start” mode until the chamber reaches  $10^{-7}$  torr. I generally leave it in “start” mode because the beginning of evaporations can create lots of vapor pressure, and it gets frustrating to turn the ion pump on over and over. I have always left the valve open so that both the turbo pump and ion pump are actively pumping the chamber at all times. The pressure during evaporation will rise too much if both pumps are not active. Once the chamber is in the  $10^{-7}$  torr range, gettering due to the evaporation will reduce the pressure to  $10^{-8}$  torr. To achieve this, simply turn on the evaporator filaments to 14 amps. This should be done slowly, as long as several hours, such that the pressure doesn't get above  $10^{-6}$  torr. When the current is 14 amps, turn on the voltage to the first evaporant. Slowly increase the voltage keeping the pressure as low as possible. Typically, 300–700 V is enough. As a rule of thumb, I switch to the emission current setting rather than the accelerating voltage. If the evaporant is properly located within a couple of millimeters of the filament loop, the emission current will rise to the first mark (10 mA). This is enough emission current and voltage to cause evaporation. It may take some tweaking of the evaporant position with respect to the filament. If this amount of emission current is not obtained with less than 1000 V, something is wrong. When the metal is heated sufficiently, it will begin to reduce the chamber pressure. Wait until the pressure has dropped to  $10^{-8}$  torr and the growth monitor is measuring 0.1–0.8 Å/sec before moving the substrates into the beam. A growth rate of more than 0.8 Å/sec will melt the evaporant. The growth rate should be kept as constant as possible by feeding the



evaporant toward the filament and adjusting the voltage/emission current.

## A.2 Some Suggested Modifications

Hopefully, the reader realizes that film crystallization is very low for room temperature substrate growth. This has a few adverse effects on material characterization. It is therefore recommended that the vacuum chamber be rearranged to allow for substrate heating. As mentioned in my Master's thesis, there is a machined substrate holder and heater spool for this purpose. However, the e-beam evaporators need to be moved to the port  $90^\circ$  from where they are currently mounted without the 14" extension tube. This would put them directly across from the 6" viewport, which has the advantage of seeing the evaporators. There were many failed attempts to incorporate mirrors in the current configuration. In order to make this change, the growth monitors will require re-routing. The top flange has already been adapted with rotary, push/pull, thermocouple, and heater feedthroughs. By rearranging in this manner, one is able to maintain the highest growth rates of 0.3–0.8 Å/sec and the growth monitors stay close to the substrate for more accurate film thickness measurement. Finally, substrate shuttering is optimized with the use of the rotary feedthrough.

## Appendix B

### LabVIEW VIs

Historically, the Markert lab has included Appendices about LabVIEW VIs which run experiments applicable to the dissertation. It seems that many have simply inserted the images of the front panel and the diagrams of the wiring without any explanation. These are easily viewed by simply opening the VI. So, why were they included? Maybe their dissertation needed a few more pages in length. Maybe it is simply to baffle new students who have never before seen LabVIEW. So, hopefully, this Appendix will be not only a review of the metal-hydride VIs, but a decent primer on LabVIEW programming. First, I should state that the acronym VI stands for virtual instrument. For simplicity, I will continue to use VI.

#### B.1 Room Temperature VI

The first of two VIs used is the room temperature measurement application, *Metal Hydride TxR.vi*. This was designed to measure resistance and transmittance simultaneously while loading hydrogen into the sample. Originally, resistance would be read directly from the Linear Research ac resistance bridge (LR-400). For some unidentified reason, the IEEE interface was causing an older Macintosh to freeze-up. Before switching to a newer computer, we abandoned reading the LR-400 directly, and set up the program to read two Keithley 195(A) DMMs set to GPIB addresses

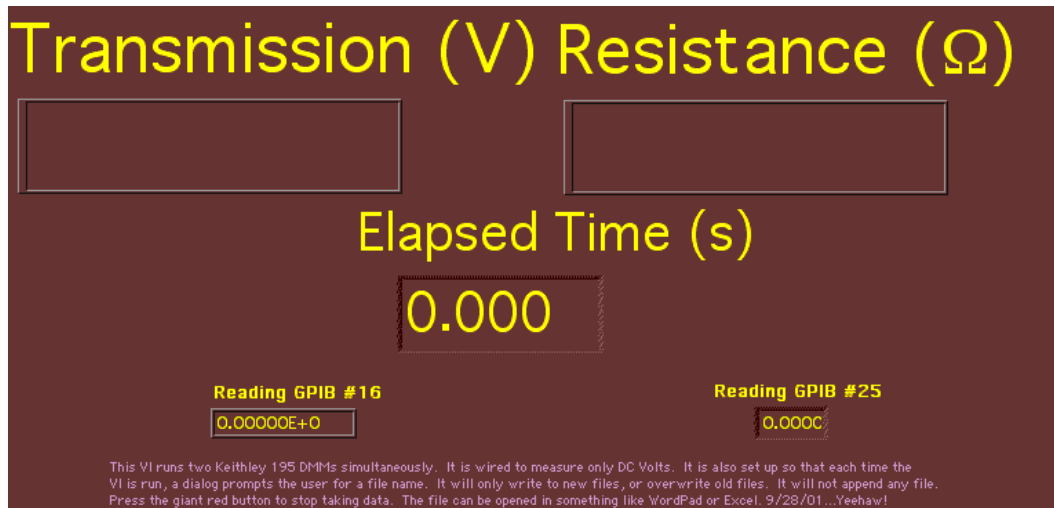


Figure B.1: Room temperature spectrometry and resistivity LabVIEW VI front panel.

16 (for the transmission) and 25 (for the resistance). The front panel, shown in Fig. B.1, displays the output voltage of the photodiode circuit, the resistance of the sample, and elapsed time. The “Reading GPIB...” readouts are the values read from the DMMs before formatting and displaying in the larger upper readouts.

To start the VI, click the continuous run button on the top left of the LabVIEW window. A prompt will appear to enter the title of the file to write. The user can also select the path of the file at this time. Inside the VI, the program has started the opening sequence, Fig. B.2. Here, the VI initializes the timer by taking the current time and date and converting into a  $t = 0$  start reference. Once the filename has been entered, the VI opens the file for writing, adds column headers to the file, and will run continuously until the user clicks the pause or stop button. The file identification information is wired into a *while* loop which runs “while” the stop button has not been pressed. Inside of the while loop, there are three sequen-

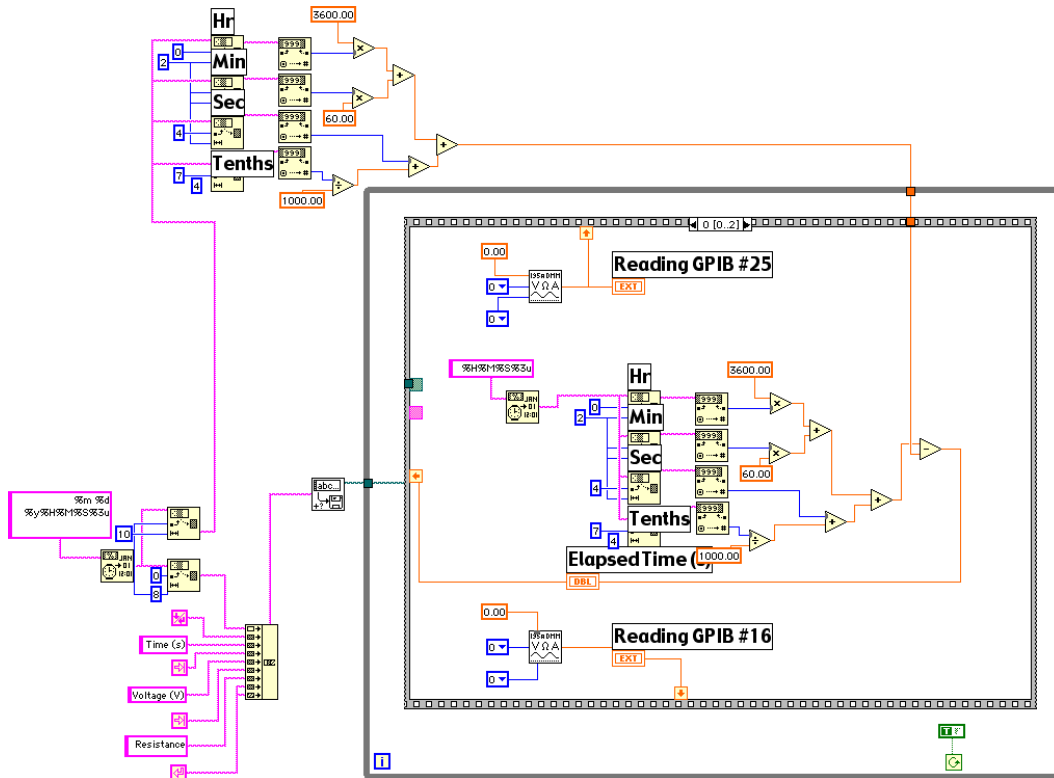


Figure B.2: The opening sequence of the room temperature VI. This sequence sets up the timer and opens a file with column headers for writing data. The time and file information are sent into a while loop that runs until the *stop* button is clicked. The while loop contains sequential frames which do all of the other operations.

tial frames. The first frame is where the DMMs are read using GPIB commands embedded in sub-VIs designed by Keithley. These sub-VIs are set to read voltage on autorange with no filtering (the 3 wired zeroes). Even resistance is set to read voltage because it is measuring the  $\pm 2$  V output of the LR-400. The two values from the DMMs and the current time are sent out of this frame and into the next.

The second frame inside the while loop (Fig. B.3) takes the measured voltages and converts them into strings with specific number formatting. The number formatting (`%e\t`) sets the file output to exponential with a tab afterwards. The tab creates a space between each measured value. The data that has been converted to string is then concatenated with a carriage return at the end to start a new line for the next data set of time, transmission, and resistance.

Finally, after concatenation, the data string is written to the file. The file is closed after each new set of data is written. The next event of writing to the file automatically goes to the end of file (EOF) to write. This works as an appendage to the existing file.

## B.2 Temperature Dependent VI

The temperature dependent VI (*MHx-lowTrho-graph.vi*) is very similar to the room temperature VI. Refer to Fig. B.5. This VI still reads two Keithley 195(A) DMMs with addresses 16 (RuO thermometer) and 25 (sample resistance). The RuO thermometer has calibration tables in Excel spreadsheets (RuOtestT and RuOtestR). The user should guard these with their life. (I accidentally altered one by mistake and spent a week figuring out why LabVIEW would not read them prop-

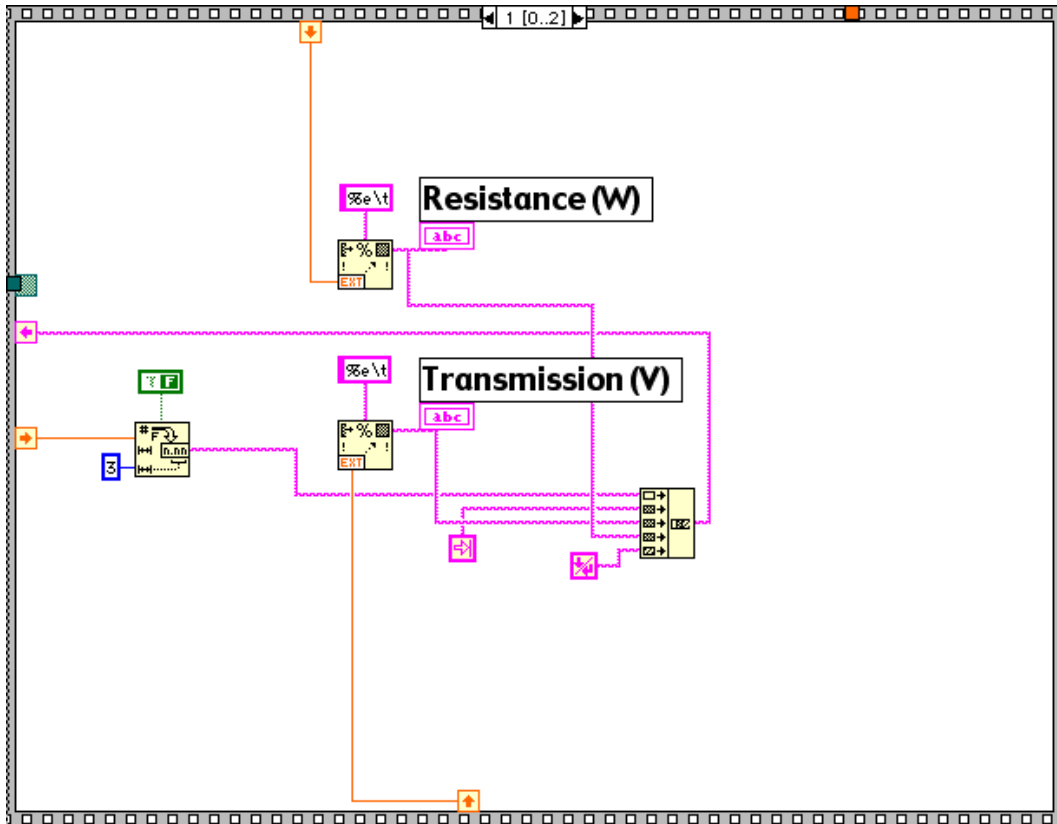


Figure B.3: The second frame of the room temperature VI. The values for resistance and transmittance voltages are formatted and converted to strings.

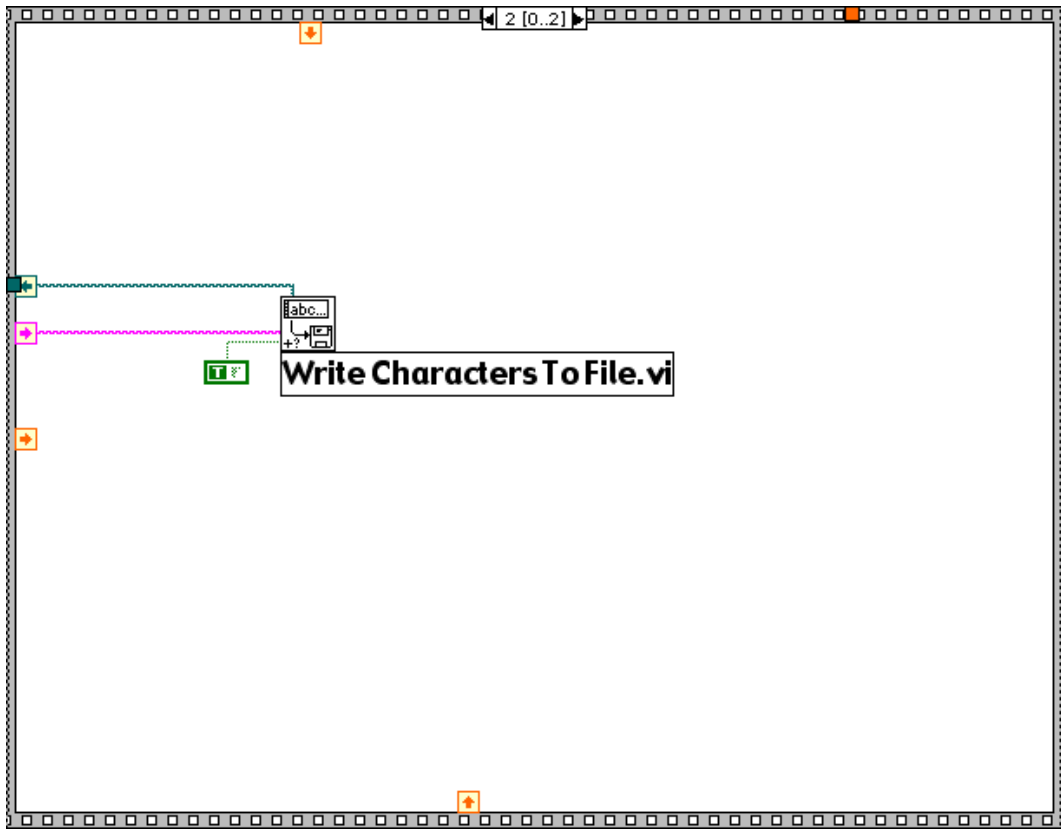


Figure B.4: Final frame of the VI. The characters for the time, transmittance (GPIB 16 voltage) and resistance (GPIB 25 voltage) are written to the file.

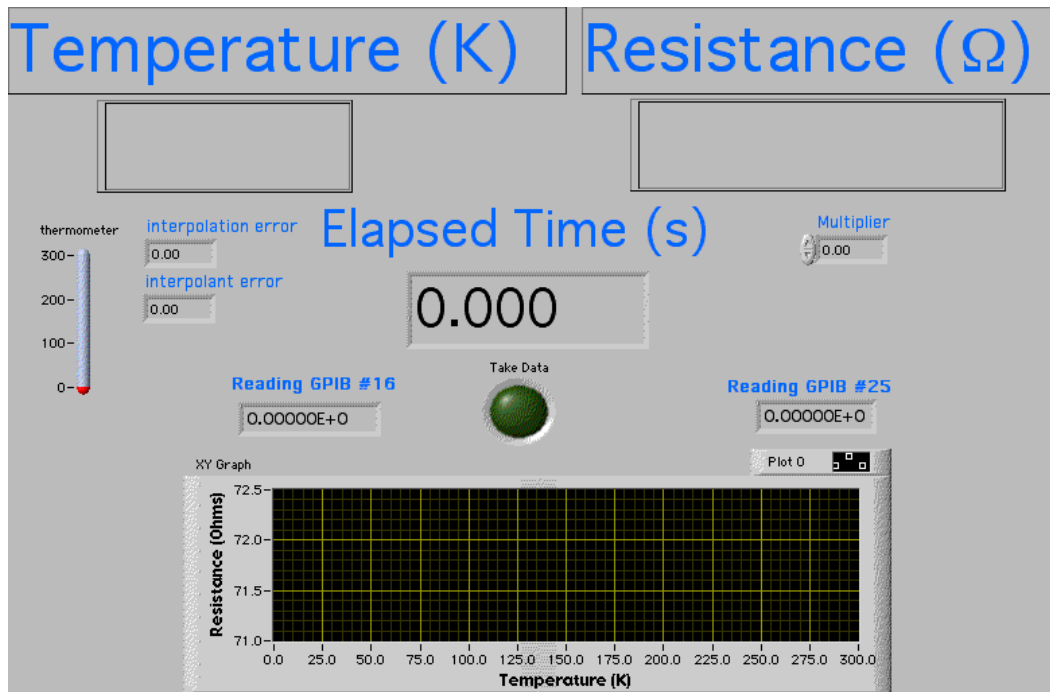


Figure B.5: Temperature dependent resistivity LabVIEW VI front panel.

erly.) The calibration tables are read into LabVIEW on each use of the program and fed to a spline interpolation (*Spline Interpolant*) which creates matrices for calculating the temperature of the probe. After the calibration files are read, a file is opened for writing, and the time is initialized, the program enters two while loops – one for the canonical stop button and one for the data collection button. Figure B.6 shows the initialization, while loops, and the final frame which writes data to the file. Error output was also added to this VI and wired to the front panel.

Another difference in this program from the room temperature one is that it has a button on the front panel which starts and stops data collection (mentioned above). This was implemented so that data could be collected only when the tem-



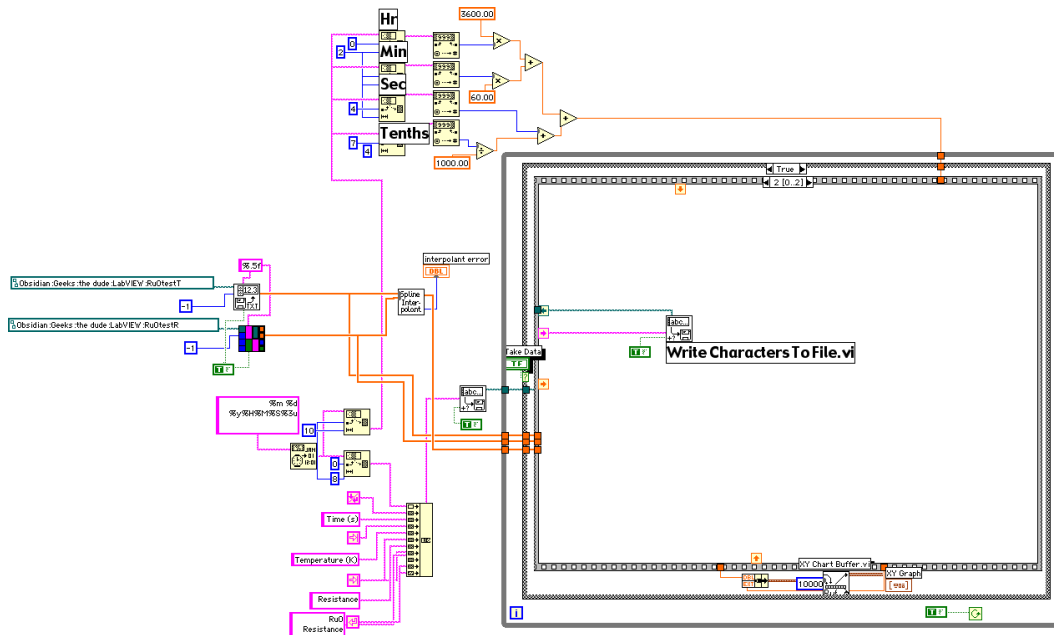


Figure B.6: A similar startup algorithm to initialize the time and start the file with column headers. This VI also opens thermometer calibration files and creates interpolation matrices to convert RuO resistance to a temperature.

perature or resistance had changed. The data collection for temperature dependence can take 3–4 hours, and therefore, would create extremely large files if left running continuously. A second major difference is the graph which plots each data point as it is being collected. There is a buffer in the diagram (Fig. B.6) set to 10000. This is the number of bits which can be stored. It may be changed if necessary, but 10000 seems to be plenty.

A requirement for these experiments was that the DMM for the RuO thermometer act as a 4-point probe. It sends current to the thermometer and measures the resistance of the thermometer. Therefore, GPIB 16 has a numeric “2” wired into it to select “ohms” instead of “volts”. This is shown in Fig. B.7. The multiplier on

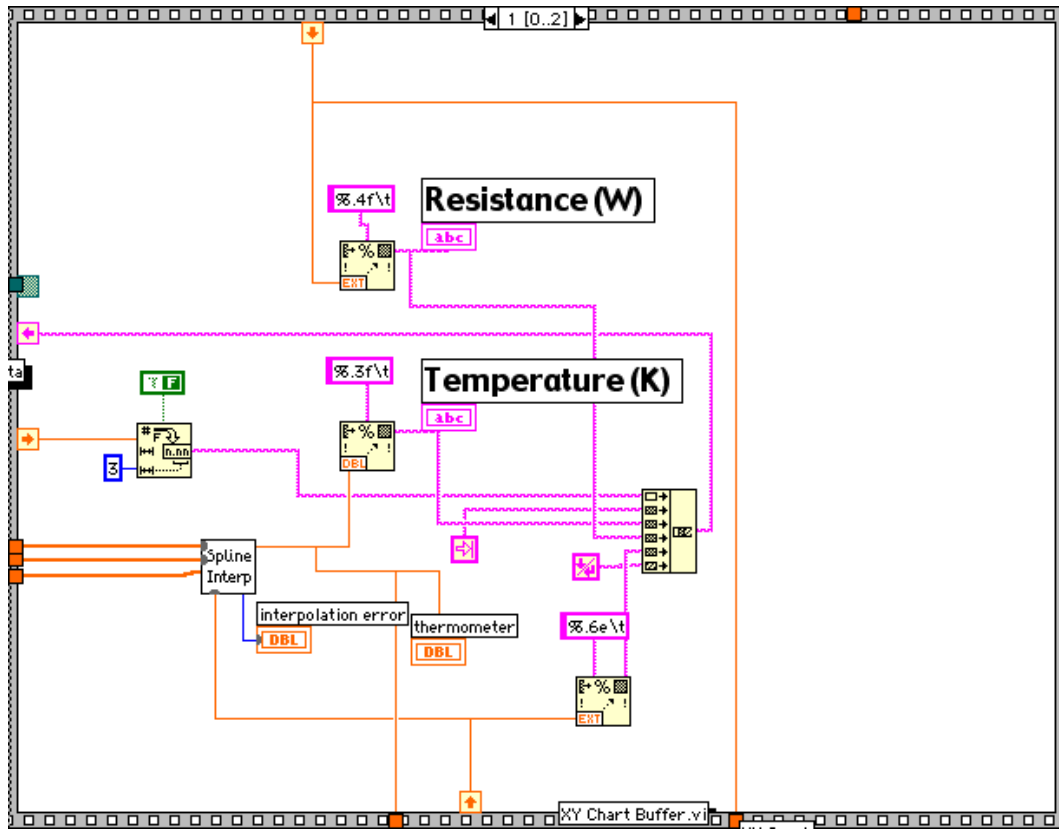


Figure B.7: The RuO resistance is interpolated, and the temperature and sample resistance are formatted and converted to strings.

the front panel is shown in the diagram in Fig. B.7. The LR-400  $\pm 2$  V output scales with the range selection on the LR-400 front panel. The multiplier, then rescales the values from the GPIB 25 DMM so that the file does not have to be corrected later.

The frame shown in Fig. B.8 is only different from the room temperature VI in that it contains the *Spline Interp* sub-VI. This takes the matrices created from *Spline Interpolant* and the thermometer resistance value to calculate the temper-

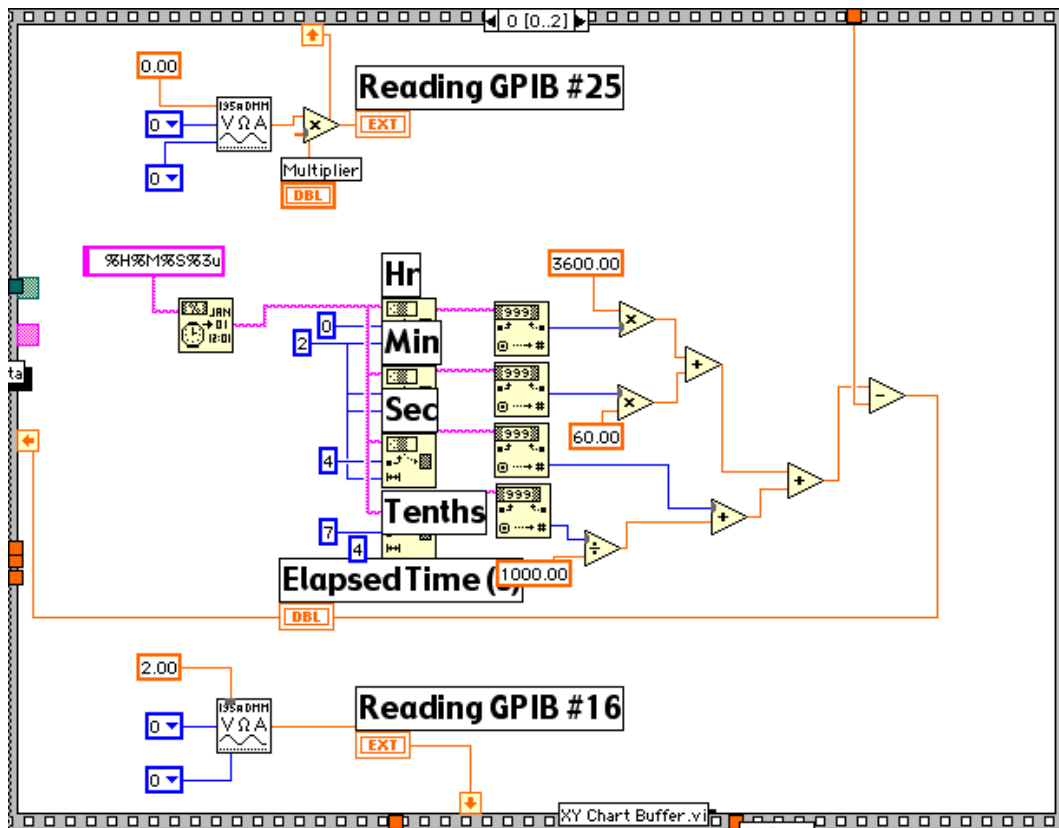


Figure B.8: This frame reads the two DMMs almost identical to the previous VI.

ature, which is then sent to the front panel and to the file along with the time, sample resistance, and actual thermometer resistance. The thermometer resistance is written to the file in the event that the interpolation goes wrong.

These VIs are about as simple as they can be written. If something should go wrong with them, hopefully, the information and images here can help reconstruct them or even better programs. It was originally my intent to make the temperature dependent VI be automated such that it would take data on its own. This was done in Boem-Hoan O's old version by checking the temperature and sample resistance and taking a data point if a significant change in either had occurred. In any event, good luck, we are all counting on you.

## Appendix C

### Nuclear Magnetic Resonance Force Microscopy

Nuclear Magnetic Resonance Force Microscopy (NMRFM) designs are aimed towards measurements with resolution of a single nuclear spin. In relation to work on hydrogen in metal systems, this will make very local measurements of hydrogen concentration and diffusion possible such that one can examine the dynamics behind the metal–insulator transition in specific metal–hydrides. In fact, simply improving force microscopy resolution to sub–micron scales ( $\approx 100$  nm) creates the capability to study the thin films of interest in this work.

#### C.1 NMR–FM Overview

The technique of NMRFM, as implied by the name, combines nuclear magnetic resonance and force microscopy techniques. Our experimental design is outlined in Fig. C.1 [67, 68]. The idea is to couple the magnetic moment of a sample to a mechanical oscillator through a field gradient produced by a permanent magnet. For the eventual practical use of NMRFM in solid state and biological applications, it will be necessary to convert to a magnet-on-oscillator geometry. The study reported here was the first attempt at such a configuration in our lab. In Fig. C.1, the permanent magnet is located on the surface of a mechanical oscillator. The force

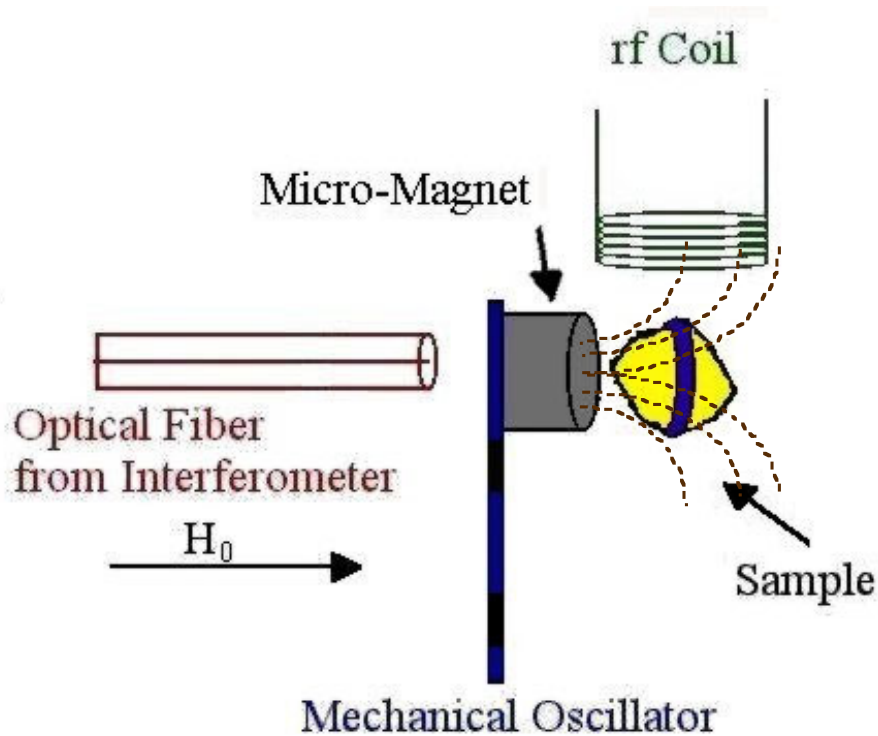


Figure C.1: Nuclear Magnetic Resonance Force Microscope (NMRFM) schematic shown in the magnet-on-oscillator geometry.

produced due to this coupling is

$$\vec{F}(t) = \vec{M}(t) \cdot \frac{d\vec{B}}{dz} \quad (\text{C.1})$$

The moment is shown to have time dependence because we adiabatically invert the spins of the sample using an rf coil [64]. Using frequency modulated rf fields, it is possible to cyclically invert the sample moment at the resonant frequency of the mechanical oscillator. This makes the force described by Eqn. C.1 drive the oscillator at resonance. Detection of the motion of the driven oscillator is performed using fiber optic interferometry with an optical laser operating at 660 nm. As seen in

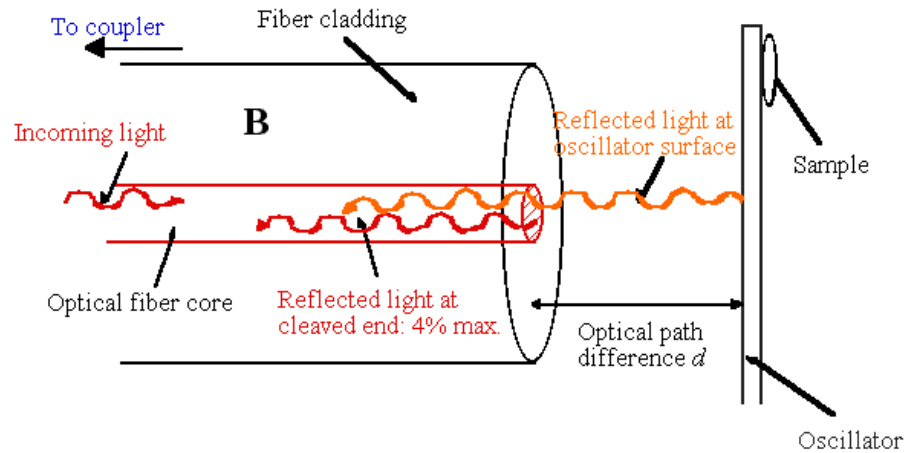


Figure C.2: Interferometry of a diode laser reflecting from a fiber optic cleave and a mechanical oscillator surface.

Fig. C.2, for a smoothly cleaved optical fiber, light reflects from the cleaved surface back into the fiber. When the optical fiber is aligned to the oscillator (see Fig. C.1 for the more realistic positioning), light reflects from the surface of the oscillator back through the fiber. As the oscillator shakes, the optical path of the reflected light changes by a factor of 2 times the amplitude of oscillation. This reflected light then interferes with light reflected from the cleaved fiber end.

Measurement stability is provided by locking onto a specific interference fringe. This is done using an op-amp feedback circuit developed by Tobias Graf [69] and improved upon by Michelle Chabot [68]. The steep slope portion of the interference pattern gives great stability because of easily detectable, large changes in signal over small ranges of position. Amplitude measurement is accurate to  $0.002 \text{ nm}/\sqrt{\text{Hz}}$  using this stabilization circuitry.

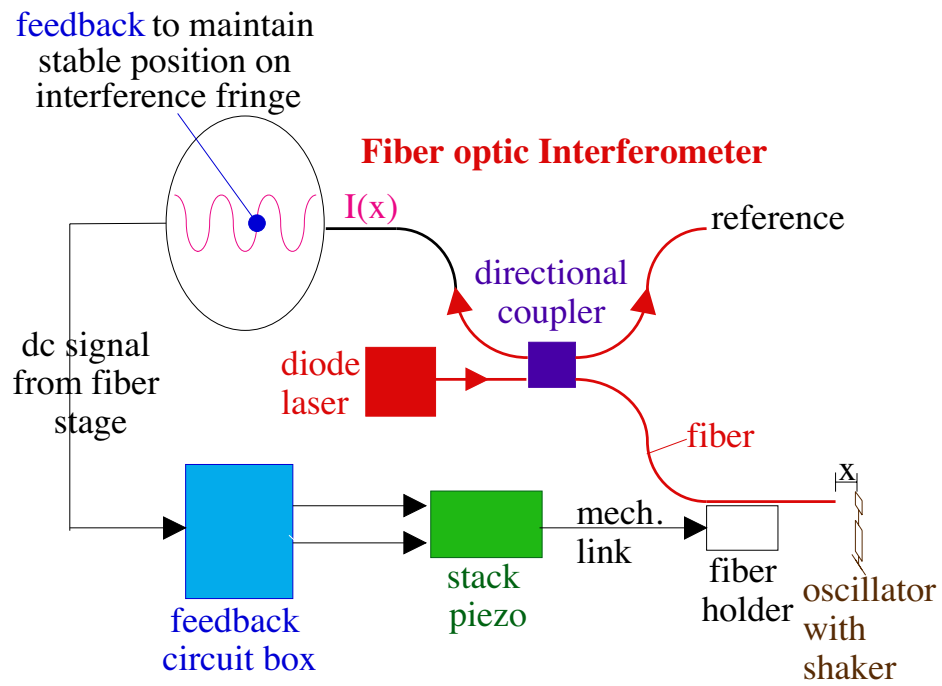


Figure C.3: Fiber optic interferometry circuit developed by Tobias Graf and Michelle Chabot.



As derived by Nyquist, the minimum force which can be measured is

$$F_{min}\left(\frac{N}{\sqrt{Hz}}\right) = \sqrt{\frac{4k_B T k_{osc}}{Q\omega}} \quad (C.2)$$

Therefore, the sensitivity of this type of force detection relies solely on the thermodynamic and mechanical properties of the oscillators used [63]. Looking at Eqn. C.1 and C.2, one can see that there are several considerations to be made. One, which is extremely important, is that of the field gradient in Eqn. C.1. However, there exists a trade-off between the field gradient magnitude and number of contributing spins which will lie within a “resonant slice” of appropriate field gradient. If the field gradient becomes too small, the force created may not be large enough to be measured above thermal noise of the oscillator. When the field gradient becomes too large, the resonant slice becomes thin, reducing the number of contributing spins. In this case,  $\vec{M}(t)$  becomes small, and again, the force is too small to be detected.

Since the metal-hydride films are on the order of  $0.1 \mu m$  thick and have a surface area of  $1cm \times 1cm$ , One obtains a necessary field gradient of

$$\frac{dB}{dz} \approx \frac{10G}{0.1\mu m} = 100 \frac{G}{\mu m} \quad (C.3)$$

resulting from the use of a pulsed rf field of 10 Gauss. Eventually, it will be interesting to increase this field gradient to see the hydrogen behavior on an atomic scale. However, even observation of hydrogen behavior within the entire film is a vast improvement to bulk interstitial hydrogen studies. For this purpose, characterization studies have been made of micron sized magnets on oscillators.

The magnitude of the field gradient is directly related to the aspect ratio of the permanent magnet. Magnetic field gradients have been modeled using

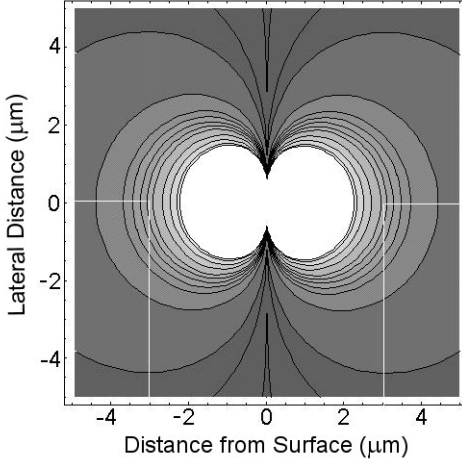


Figure C.4: Contour plot of magnetic field gradient for a micron-sized magnet with  $1 \mu\text{m}$  diameter and  $0.1 \mu\text{m}$  thickness. The lines are drawn to indicate a  $3 \mu\text{m}$  distance from the magnet face where the field gradient for this magnet aspect ratio is  $100 \text{ G}/\mu\text{m}$ , as desired.

Mathematica<sup>TM</sup>. For cylindrically shaped magnets of cobalt (Co), with an aspect ratio of  $1 \mu\text{m}$  diameter and  $0.1 \mu\text{m}$  thickness, a field gradient of  $100 \text{ G}/\mu\text{m}$  at approximately  $3 \mu\text{m}$  distance from the magnet surface was determined. Figure C.4 illustrates the field gradient contours, where the lines indicate a distance of  $3 \mu\text{m}$  from the surface directly in front of the magnet face. Figure C.5 plots the field gradient magnitude (for the contours shown in Fig. C.4) with respect to distance from the micro-magnet surface. The lines are to indicate a  $100 \text{ G}/\mu\text{m}$  field gradient at a distance of  $3 \mu\text{m}$  from the magnet surface.

Pictorially, one can think of the field gradient contours such that two contours defining the region around  $100 \frac{\text{G}}{\mu\text{m}}$  encase the film thickness. In addition, the curvature of the gradient contours, ideally, is low enough to span  $1\text{--}4 \mu\text{m}^2$  of the film sample lateral surface as shown in Fig. C.6.

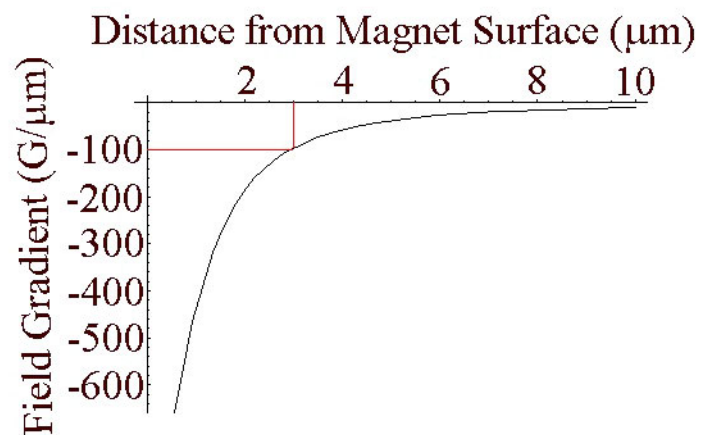


Figure C.5: Magnetic field gradient as a function of distance from the surface of a micron-sized magnet with 1  $\mu\text{m}$  diameter and 0.1  $\mu\text{m}$  thickness. The lines indicate that a distance of 3  $\mu\text{m}$  from the surface provides a field gradient of 100  $\text{G}/\mu\text{m}$ .

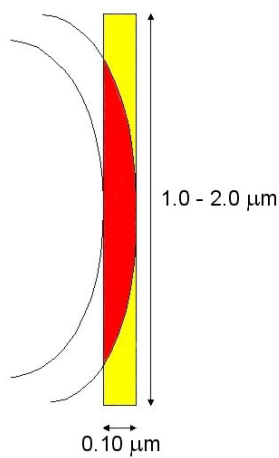


Figure C.6: Ideal spatial relationship between magnetic field gradient contours and sample film being measured.

**Commercial and Micro-Machined Oscillators**

Type	Q	k ( $\frac{N}{m}$ )	$F_{min}$ ( $\frac{N}{\sqrt{Hz}}$ )
Nanoprobe	10–100	10–100	$0.7\text{--}2.3 \times 10^{-13}$
Ultralever	10–100	0.01–0.05	$1.5\text{--}5.7 \times 10^{-14}$
Torsional	1–10k	0.005	$1.5\text{--}5.0 \times 10^{-16}$

Table C.1: Quality factors, spring constants, and minimal detectable forces for oscillators prior to magnet deposition.

## C.2 Oscillators

Availability of commercial cantilever-type oscillators and their characteristic data made these types of oscillators desirable for initial magnet-on-oscillator characterization. Two types of commercial cantilevers have been used.

The first type is a high resonant frequency (300 kHz) cantilever produced by Digital Instruments for use in their Nanoprobe atomic force microscope (AFM). The second type is a Park Scientific Ultralever AFM cantilever with resonance frequencies in the 1–22 kHz range. In addition, using silicon micro-machining techniques, torsional oscillators have been developed by our group with much higher force sensitivity and Q factor for force measurement on the order of  $10^{-16} N/\sqrt{Hz}$ . Figure C.7 shows the approximate dimensions of these cantilevers, and Table C.1 lists quality factors (Q), spring constants (k) and minimal detectable forces ( $F_{min}$  – Eqn. C.2) for the oscillators. Free-standing torsional oscillators as shown in Fig. C.7 have only recently been developed, and thus, magnet-on-oscillator characterization is still in progress. All measurements were taken at room temperature.

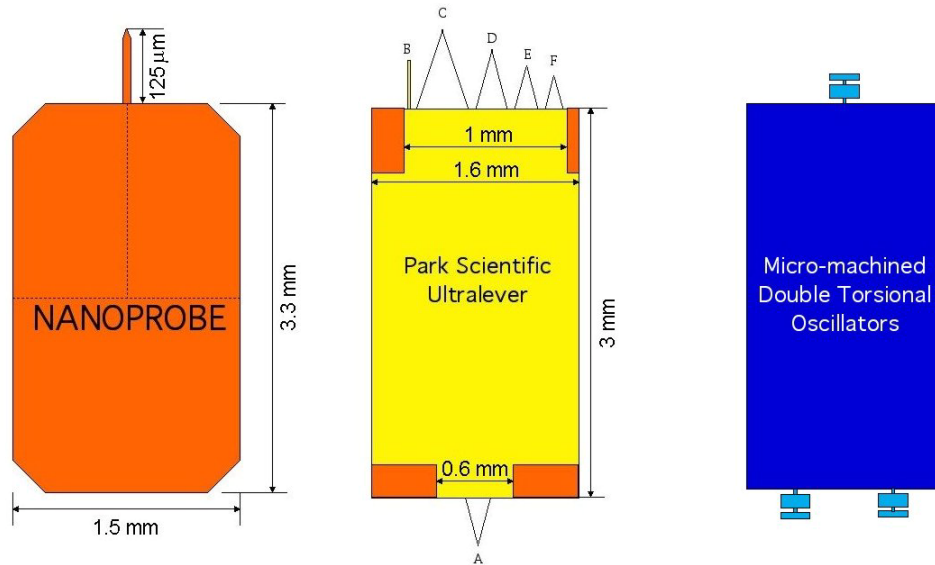


Figure C.7: Commercial and micro-machined oscillators used for magnet characterization.

### C.3 Micro-Magnets

The vacuum and film deposition system described in Chapter 2 was used to deposit cobalt magnets capped with an anti-oxidation layer of gold. Accurate monitoring of film thickness was possible using Inficon crystal growth monitors. Cobalt layers were measured to be between  $0.06 - 0.10 \mu\text{m}$ . Due to their lower sensitivity, Nanoprobe cantilevers were shadow masked with aluminum foil such that a section of the tip was coated. Micron-sized pinholes in aluminum foil were used to shadow mask the Ultralevers. Figures C.8 – C.10 are scanning electron microscope (SEM) images of some typical magnets obtained.

Typically, magnetic films of this thickness have an easy magnetic axis in the plane of the film, however, this shape anisotropy was overcome by applying a large

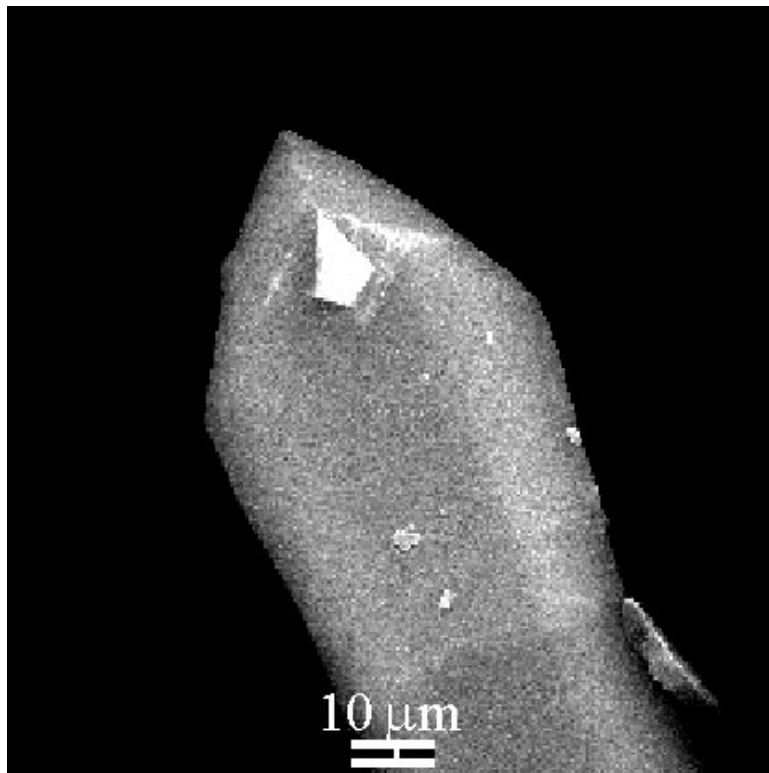


Figure C.8: SEM image of Nanoprobe cantilever with an approximately  $(30 \mu\text{m})^2$  magnet of 83 nm cobalt capped with 12 nm gold.

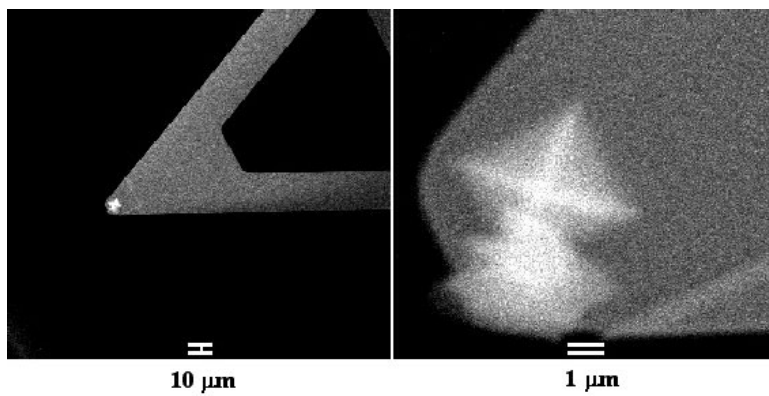


Figure C.9: SEM image of Ultralever cantilever with a cobalt magnet 4  $\mu\text{m}$  in diameter, 60 nm thick capped with 8 nm of gold.

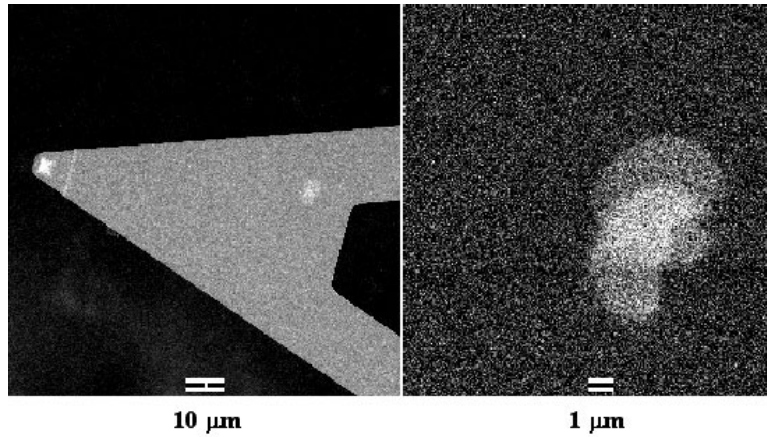


Figure C.10: SEM image of Ultralever cantilever with a cobalt magnet a  $2\ \mu\text{m}$  in diameter, 60 nm thick capped with 12 nm of gold.

static field of approximately 1 tesla. Figure C.11 shows magnetization data taken previously on larger area films ( $\approx 1\ \text{mm}^2$ ) where 1 tesla was large enough to reach saturation of the magnetic moment. Thus, for these micron-sized magnet areas, we assume a fully saturated magnetic moment perpendicular to the plane of the film.

It is important to note the interest in this study is in flat pancake geometry magnets for their well-understood field gradient geometry. This is different from applications such as magnetic force microscopy (MFM) where a sharp magnetic tip is needed for high resolution. It is, therefore, desirable to deposit the magnet on flat regions of the oscillator and as close to the tip end as possible for the greatest induced vibration amplitude.

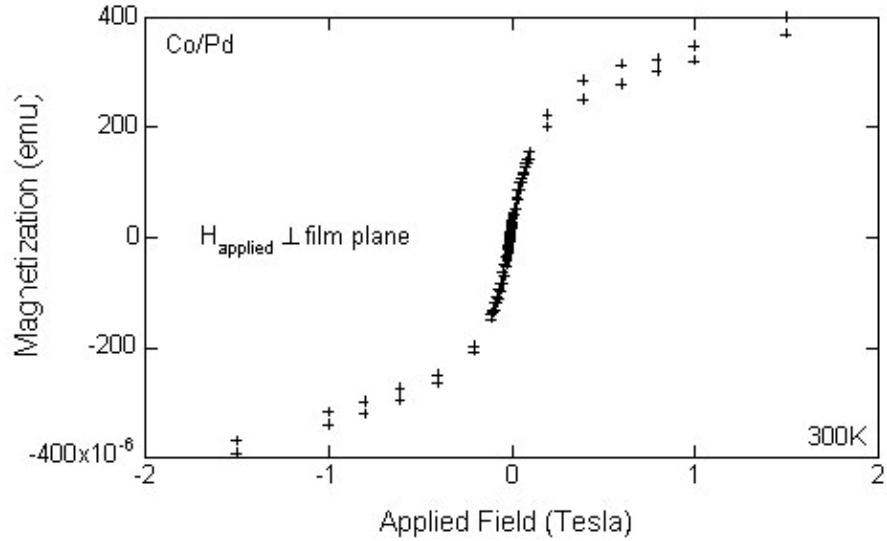


Figure C.11: Measurement of magnetic saturation perpendicular to the plane of a  $0.06 \mu\text{m}$  cobalt film.

#### C.4 Magnet-on-Oscillator Characterization

In order to measure the magnetic moment produced, a wire coil with radius 1.4 mm was placed in the NMR-FM probe with the optical fiber through its center 5 mm from the oscillator surface. The well defined field gradient of the coil interacts with the Co magnetic moment to produce a force on the oscillator. The experimental arrangement is shown in Fig. C.12. The oscillator is driven by operating the coil with a sinusoidal current at the resonant frequency of the oscillator. The magnetic field gradient produced is approximately  $10^{-2}$  T/m. Assuming the micro-magnet geometries are truly flat, one can calculate by volume the moment produced by the cobalt to get the expected force from Eqn. C.1. These values are compared with the



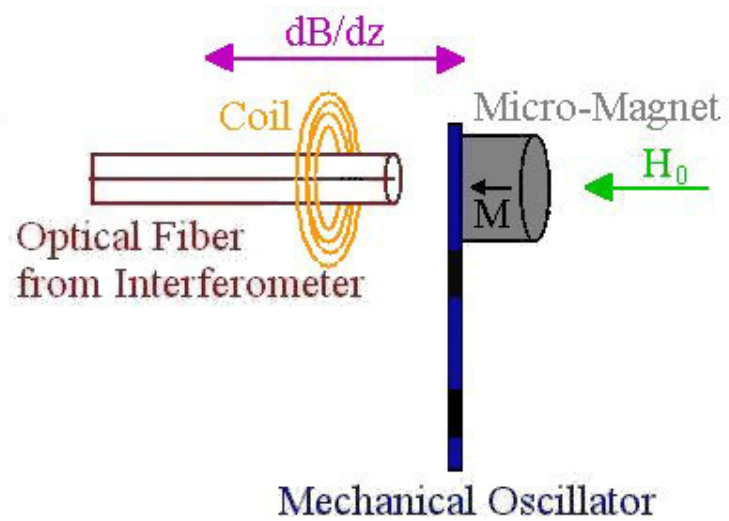


Figure C.12: NMR-FM probe modified with a coil around the optical fiber to measure micro-magnets on oscillators.

### Commercial and Micro-Machined Oscillators

Micromagnet (Figure #)	Calculated Cobalt Moment ( $\frac{J}{T}$ )	Expected Force (N)	Measured Force in air (N)
Nanoprobe (5.8)	$1.1 \times 10^{-10}$	$3 \times 10^{-12}$	$7 \times 10^{-12}$
Ultralever (5.9)	$1.1 \times 10^{-12}$	$8.6 \times 10^{-14}$	$9 \times 10^{-14}$
Ultralever (5.10)	$7 \times 10^{-13}$	$4.3 \times 10^{-14}$	$3 \times 10^{-14}$

Table C.2: Comparison of calculated and measured forces from micro-magnets on cantilevers.

force detected on the oscillator by rewriting Eqn. C.2 as

$$F = \frac{Ak_{osc}}{Q}. \quad (C.4)$$

The values for  $Q$  and  $\omega_0$  are determined from frequency scans, and  $k_{osc}$  is the oscillator spring constant, estimated to be 0.01N/m. Table 5.2 summarizes these comparisons. The agreement is reasonable between the expected and measured forces, indicating a successful demonstration of the magnetic excitation of micro-oscillators. The Nanoprobe expected forces were smaller than measured due to the faceted edges of the cantilever leading to an underestimation of the total moment.

More details may be extracted by continuing this research using a probe geometry where the excitation coil is perpendicular to the oscillator surface. Then, the torque on the oscillator is

$$\vec{\tau} = \vec{\mu} \times \vec{H} \quad (C.5)$$

which is the torque applied to the micro-magnet moment,  $\mu$ , by the applied magnetic field,  $H$ . Recently, studies were made to see the effects of external magnetic field on the oscillator characteristics [72]. These results combined with probe and micro-

magnet improvements indicate readiness of our NMR force microscopy for solid-state applications.

## Appendix D

### Some Pictures

I have absolutely no reason for adding these pictures. They are just a few of the things that kept me going or gave me a good laugh during graduate school. Hopefully, the students who supercede me have as good a time as I did living in Austin, knowing John and his family, and studying condensed matter physics. Adios, Amigos.



Figure D.1: Troy speaking at the Metal Hydrides conference (MH2002) in Annecy, France.



Figure D.2: Troy marrying Jodi at his parents' house in Rockwall, Texas, April 7, 2001.

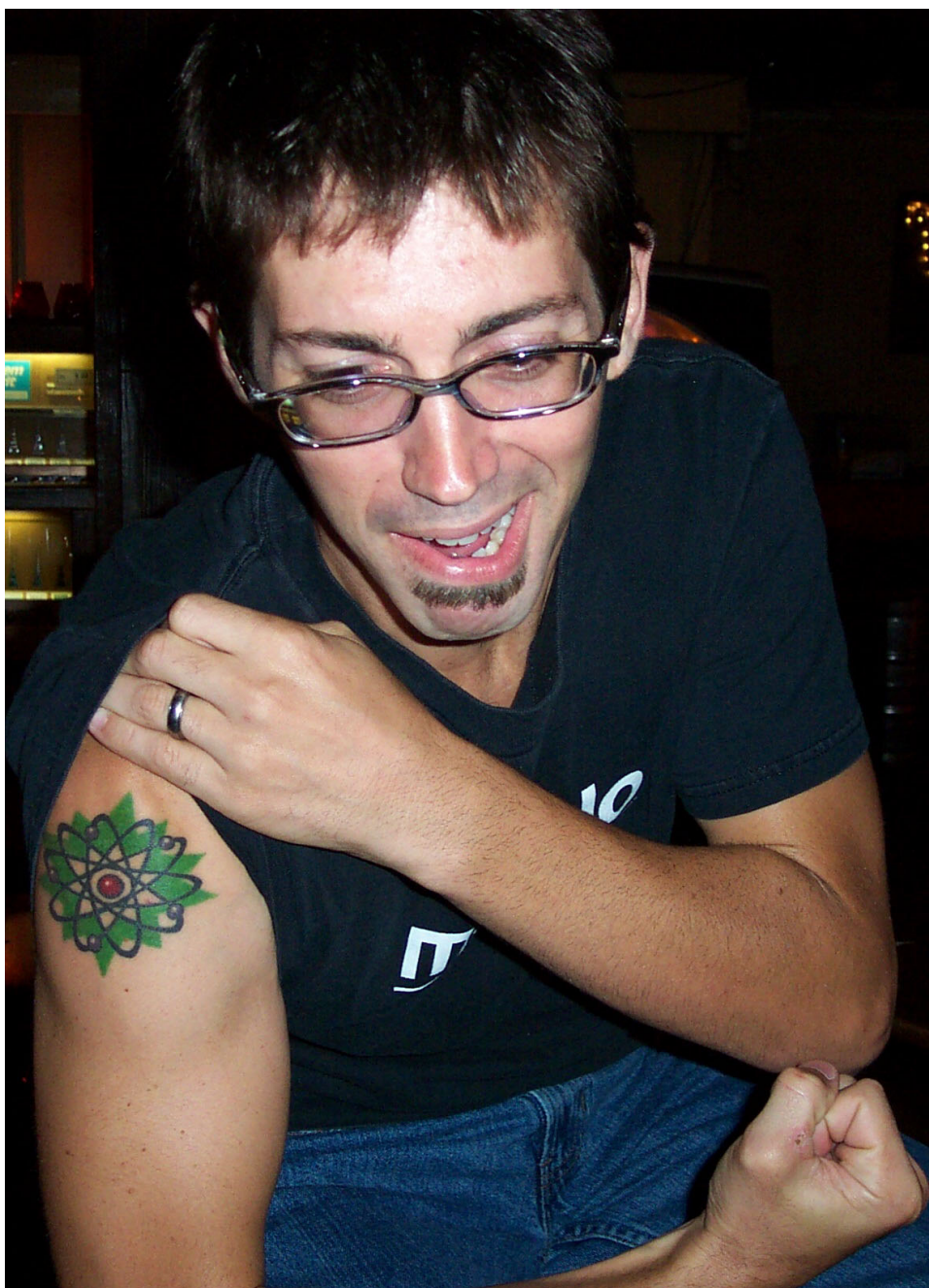


Figure D.3: Troy showing off his super-cool boron tattoo.




Figure D.4: Troy bangin' the skins at Steamboat with former band Megalo.

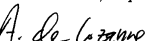


The Dissertation Committee for Troy Christopher Messina  
certifies that this is the approved version of the following dissertation:

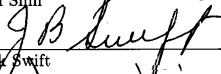
**Steric Effects in the Metallic-Mirror to  
Transparent-Insulator Transition in  $\text{YH}_x$**

Committee:

  
\_\_\_\_\_  
John T. Markert, Supervisor

  
\_\_\_\_\_  
Alex de Lozanne

  
\_\_\_\_\_  
Ken Shih

  
\_\_\_\_\_  
Jack Swift

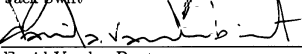
  
\_\_\_\_\_  
David Vanden Bout

Figure D.5: Signature page for this dissertation.

## Bibliography

- [1] T. Graham, *Philos. Trans. Roy. Soc. London* 156, 399 (1866).
- [2] J.N. Huiberts, R. Griessen, J.H. Rector, R.J. Wijngaarden, D.G. de Groot, and N.J. Koeman, *Nature* 380, 231 (1996).
- [3] M. Ouwerkerk, *Electrochemical Hydrogen Storage Properties of Magnesium-Scandium Hydride Thin Films and Powders*, Philips Research presentation, Gordon Conference (2001).
- [4] R. Griessen *et al.*, *J. Alloys Comp.* 253-254 44, (1997).
- [5] S.J. van der Molen, M.S. Welling, and R. Griessen, *Phys. Rev. Lett.* 85, 3882 (2000).
- [6] A. T. M. van Gogh, Doctoral dissertation *Probing the Metal-Insulator Transition in Rare-Earth Based Switchable Mirrors*, (Vrije Universiteit, Amsterdam, 2001).
- [7] M. L. Lieberman and P. G. Wahlbeck, *J. Phys. Chem.* 69, 3973 (1965).
- [8] M. L. Lieberman and P. G. Wahlbeck, *J. Phys. Chem.* 69, 3514 (1965).
- [9] M. L. Lieberman and P. G. Wahlbeck, *J. Phys. Chem.* 69, 2510 (1965).
- [10] M. Kremers *et al.*, *Phys. Rev. B* 57, 4943 (1998).

- [11] J. N. Huiberts *et al.*, *J. Alloys Comp.* 239, 158 (1996).
- [12] S. J. van der Molen *et al.*, *J. Appl. Phys.* 86, 6107 (1999).
- [13] A. F. Th. Hoekstra *et al.*, *Phys. Rev. Lett.* 86, 5349 (2001).
- [14] L. Schlapbach, ed., *Hydrogen in Intermetallic Compounds* (Springer, Berlin, 1988).
- [15] P. Vajda, "Hydrogen in Rare-Earth Metals, Including  $\text{RH}_{2+x}$  Phases" in *Handbook on the Physics and Chemistry of Rare Earths*, Vol. 1 (Elsevier, 1995).
- [16] *Ibid*, Vol. 8, p.1-161.
- [17] *Ibid*, Vol. 20, p.105-291.
- [18] *Ibid*, Vol. 27, p.339-533.
- [19] R. M. Cotts, in *Hydrogen in Metals I*, G. Alefeld and J. Volkl, eds. (Springer, 1978), p.227.
- [20] B. Y. Kotur and E. Gratz "Scandium Alloy Systems and Intermetallics" in *Handbook on the Physics and Chemistry of Rare Earths*, K. A. Gschneidner, Jr. and L. Eyring, eds. vol. 27 (North-Holland, 1999), p.339-533.
- [21] P. J. Kelly, J. P. Dekker, R. Stumpf, *Phys. Rev. Lett.* 78, 1315 (1997).
- [22] Y. Wang, M. Y. Chou, *Phys. Rev. B* 51, 7500 (1995).
- [23] K. K. Ng, F. C. Zhang, V. I. Anisimov, T. M. Rice, *Phys. Rev. Lett.* 78, 1311 (1997).

- [24] A. T. M. van Gogh and R. Griessen, *J. Alloys Comp.*, 330-332, 338 (2002).
- [25] A. T. M. van Gogh, D. G. Nagengast, E. S. Kooij, N. J. Koeman, J. H. Rector, and R. Griessen, *Phys. Rev. B* 63, 195105 (2001).
- [26] MDI Jade software package for pattern analysis and phase identification, Materials Data Inc., Livermore, CA, USA.
- [27] P. van Gelderen and P. J. Kelly and G. Brocks, and R. Stumpf, *Phys. Rev. B*, 63, 100301 (2001).
- [28] M. Rode *et al.*, *Phys. Rev. Lett.* 78, 1315 (1997).
- [29] D. G. Nagengast *et al.*, *Appl. Phys. Lett.* 75, 2050 (1999).
- [30] I. A. M. E. Geibels *et al.*, *J. Alloys Comp.* 330, 875 (2002).
- [31] J. Isidorsson *et al.*, *Electrochimica Acta* 46, 2179 (2001).
- [32] J. W. J. Kerssemakers *et al.*, *Nature* 406, 489 (2000).
- [33] F. J. A. den Broeder *et al.*, *Nature* 394, 656 (1998).
- [34] A. T. M. van Gogh *et al.*, *Appl. Phys. Lett.* 77, 815 (2000).
- [35] A. T. M. van Gogh, E. S. Kooij, and R. Griessen, *Phys. Rev. Lett.* 83, 4614 (1999).
- [36] J. N. Huibertset *et al.*, *Phys. Rev. Lett.* 79, 3724 (1997).
- [37] P. L. Notten, M. Kremers, and R. Griessen, *J. Electrochem. Soc.* 143, 3348 (1996).

- [38] E. S. Kooij, A. T. M. van Gogh, and R. Griessen, *J. Electrochem. Soc.* 146, 2990 (1999).
- [39] T. C. Messina, C. W. Miller, and J. T. Markert", *J. Alloys Comp.*, in press (2003).
- [40] H. Kierey *et al.*, *Phys. Rev. B* 63, 134109 (2001).
- [41] A. C. Switendick, *J. of Less Common Metals* 74, 199 (1980).
- [42] J. H. Weaver and D. T. Peterson, *J. of Less Common Metals* 74, 207 (1980).
- [43] C. L. Jensen and M. P. Zalesky, *J. of Less Common Metals* 75, 197 (1980).
- [44] J. W. Ross and L. L. Isaacs, *J. Phys. Chem. Solids* 31, 747 (1970).
- [45] Z. Fisk and D. C. Johnston, *Phys. Lett.* 53A, 39 (1975).
- [46] M. Jerosch-Herold *et al.*, *Z. Naturforsch* 40a, 222 (1984).
- [47] R. B. McLellan and R. Kirchheim, *J. Phys. Chem. Solids* 41, 1241 (1980).
- [48] A. E. Curzon and O. Singh, *J. Phys. F: Metal Phys.* 8, 1619 (1978).
- [49] A. E. Curzon and O. Singh, *Thin Solid Films* 57, 157 (1979).
- [50] S. J. van der Molen, M. S. Welling, and R. Griessen, *Phys. Rev. Lett.* 85, 3882 (2000).
- [51] A. T. M. van Gogh *et al.*, *Phys. Rev. Lett.* 85, 2156 (2000).
- [52] J. Shinar, B. Dehner, B. J. Beaudry, and D. T. Peterson, *Phys. Rev. B* 37, 2066 (1988).

- [53] J. Shinar, B. Dehner, R. G. Barnes, and B. J. Beaudry, *Phys. Rev. Lett.* 64, 563 (1990).
- [54] *CRC Handbook of Chemistry and Physics* (CRC, Boca Raton, 1987-88), 68th edition.
- [55] S. L. Altmann and C. J. Bradley, *Proc. Phys. Soc.* 92, 764 (1967).
- [56] G. S. Fleming and T. L. Loucks, *Phys. Rev.* 173, 685 (1968).
- [57] S. Mahmoud and Z. S. El Mandouh, *J. of Materials Science* 22, 651 (1987).
- [58] M. Sigrist *et al.*, *Phys. Rev. B* 35, 3760 (1987).
- [59] D. A. Gorodetskii and A. A. Yask'ko, *Soviet Physics-Solid State* 11, 2028 (1970).
- [60] R. Ahuja, B. Johansson, J. M. Wills, and O. Eriksson, *Appl. Phys. Lett.* 71, 3498 (1997).
- [61] E. J. Johnson in *Semiconductors and Semimetals*, eds. R. K. Willardson and C. Beer (Academic Press, New York, 1967), v. 3.
- [62] D. Rugar, O. Zugar, S. Hoen, C.S. Yannoni, H.-M. Vieth, and R.D. Kendrick, *Science* 264, 1560 (1994).
- [63] J. A. Sidles, *Appl. Phys. Lett.* 58, 2854 (1991).
- [64] K. Wago, D. Botkin, C. S. Yannoni, and D. Rugar, *Phys. Rev. B* 57, 1108, (1998).

- [65] J. A. Sidles, *et al.*, *Rev. Mod. Phys.* 67, 249 (1995).
- [66] D. Rugar, C. S. Yannoni, and J. A. Sidles, *Nature* 360, 563 (1992).
- [67] T. A. Barrett, *Experimental Considerations for the Development of a Nuclear Magnetic Resonance Force Microscope*, Ph.D. Dissertation, University of Texas at Austin, Department of Physics, (1999).
- [68] M. D. Chabot, *Force Detection of Nuclear Magnetic Resonance using Double-Torsional Micro-Oscillators*, Ph.D. Dissertation, University of Texas at Austin, Department of Physics, (2001).
- [69] T. Graf, *Interferometry on High-Q Double-Torsional Oscillators for the Study of Vortices in in Type-II Superconductors*, Master of Science Thesis, University of Texas at Austin, Department of Physics, (1998).
- [70] M. D. Chabot and J. T. Markert, *Proc. SPIE* 3875, 104 (1999).
- [71] M. D. Chabot, T. C. Messina, V. Mancevski, C. W. Miller, and J. T. Markert, *Proc. SPIE* 4559, 24 (2001).
- [72] C. W. Miller, U. M. Mirsaidov, T. C. Messina, Y. J. Lee, and J. T. Markert, *47<sup>th</sup> Annual Conference on Magnetism and Magnetic Materials*, Tampa, Florida, USA, 2002, to be published in *J. Appl. Phys.* May 2003.
- [73] E. Hecht, “The Diffraction Grating” in *Optics*, 3<sup>rd</sup> ed. (Addison-Wesley, Massachusetts, 1998), p.465–72.

- [74] T. C. Messina, *Design, Construction, and Characterization of an Ultra-High Vacuum System for Synthesis of Magnetic Thin Films*, Master of Arts Thesis, University of Texas at Austin, Department of Physics, (1999).
- [75] C. Kittel, *Introduction to Solid State Physics*, 6<sup>th</sup> ed. (John Wiley and Sons, Inc., New York, 1998), p.49.
- [76] T. B. Massalski *et al.*, *Binary alloy phase diagrams*, (American Society for Metals, Ohio, 1986), CD-ROM.



## Publications

### Invited Talks

- T. C. Messina, C. W. Miller, J. T. Markert, “Steric Effects in the Metal-Insulator (Mirror-Transparent) Transition in  $\text{YH}_x$ ,” University of Texas at Austin, Graduate Student Lecture Series, September 17, 2002.

### Talks, Posters, and Presentations

- T. C. Messina, C. W. Miller, J. T. Markert, “Optical Switching, Structure, and Transport in Y-Sc Hydride Thin Films,” American Physical Society March Meeting 2002, Indianapolis, IN, USA, 18-22 March 2002.
- J. T. Markert, G. I. Drandova, T. C. Messina, “NMR of  $^{89}\text{Y}$  in the Copper-Oxide Spin-Chain Compound  $\text{Ca}_{2+x}\text{Y}_{2-x}\text{Cu}_5\text{O}_{10}$ ,” American Physical Society March Meeting 2002, Indianapolis, IN, USA, 18-22 March 2002.
- C. W. Miller, M.D. Chabot, T. C. Messina, Y.J. Lee, J.T. Markert, “Nuclear Magnetic Resonance Force Microscopy Using Single-Crystal Silicon Double-Torsional Micro-Oscillators,” American Physical Society March Meeting 2002, Indianapolis, IN, USA, 18-22 March 2002.
- T. C. Messina, M. D. Chabot, K. T. Tatebe, U. Mirsaidov, A. Badinski, and J. T. Markert, “Magnet-on-Oscillator Characterization for Nuclear Magnetic Resonance Force Microscopy,” American Physical Society March Meeting

2001, Seattle, WA, USA, 12-16 March 2001.

- P. S. Lysaght, R. Bergmann, J. Chen, T. Messina, R. Murto, D. Sing, and H. R. Huff, “Experimental Observations of the Thermal Stability of High- $\kappa$  Gate Dielectric Materials on Silicon,” Abstract for the 2001 meeting of the Materials Research Society (E-MRS).
- J. T. Markert, K. Mochizuki, T. C. Messina, E. E. Judge, (University of Texas at Austin), B. Dam, J. Huijbregste, J. H. Rector, M. Vreeken, R. Griessen (Institute COMPAS, Faculty of Physics and Astronomy, Vrije University, Amsterdam, the Netherlands), “Thin Films of Infinite-Layer  $\text{Sr}_{1-x}\text{La}_x\text{CuO}_2$  Grown by Laser Ablation,” Abstracts of the 1998 March Meeting of the American Physical Society, Los Angeles, CA (1998)
- E. E. Judge, K. Mochizuki, T. C. Messina, J. T. Markert (University of Texas at Austin), B. Dam, J. Huijbregste, J. H. Rector, M. Vreeken, R. Griessen (Institute COMPAS, Faculty of Physics and Astronomy, Vrije University, Amsterdam, the Netherlands), “Hall Effect and Post-Annealing of Thin Films of Infinite-Layer  $\text{Sr}_{1-x}\text{La}_x\text{CuO}_2$ ,” American Physical Society March Meeting 1998, Los Angeles, CA (1998)
- J.T. Markert, B.C. Dunn, T.C. Messina, M.M. Maedgen, “Magnetism, Structure, and Resistivity of the Lithium-Doped T'-Phase:  $\text{Gd}_2\text{Cu}_{1-x}\text{Li}_x\text{O}_{4-d}$  and  $\text{Nd}_{2-y}\text{Ce}_y\text{Cu}_{1-x}\text{Li}_x\text{O}_{4-d}$ ,” Abstracts of the 5th International Conference on Materials and Mechanisms of Superconductivity - High Temperature Superconductivity (M<sup>2</sup>S-HTSC-V), Beijing, China, 28 February - 4 March 1997.

- J.T. Markert, K. Mochizuki, T.C. Messina, “Extreme Low Amplitude Vortex Dissipation Study of Single Crystal  $\text{YBa}_2\text{Cu}_3\text{O}_{7-d}$  Using High-Q Mechanical Oscillators,” Abstracts of the 5th International Conference on Materials and Mechanisms of Superconductivity - High Temperature Superconductivity ( $\text{M}^2\text{S-HTSC-V}$ ), Beijing, China, 28 February–4 March 1997.

## Articles

- C.W. Miller, U. Mirsaidov, T.C. Messina, J.T. Markert, “External Field Effects on Characteristics of Magnetically-Capped Oscillators for Magnetic Resonance Force Microscopy,” 47th Annual Conference on Magnetism and Magnetic Materials, Tampa, Florida, USA, 2002, to be published in Journal of Applied Physics May 2003.
- T. C. Messina, C. W. Miller, J. T. Markert, “Steric Effects in the Metal-Insulator (Mirror-Transparent) Transition in  $\text{YH}_x$ ,” J. Alloys and Compounds - Proceedings for MH2002, Annecy, France, 2002 (in press).
- J.T. Markert, T.C. Messina, B. Dam, J. Huijbregste, J.H. Rector, and R. Griessen, “Infinite-Layer Copper-Oxide Laser-Ablated Thin Films: Substrate, Buffer-Layer, and Processing Effects,” Applied Superconductivity Conference, Houston, Texas, USA, 2002, to be published in IEEE Transactions on Applied Superconductivity 2003.
- G. I. Drandova, T. C. Messina, J. T. Markert, “NMR of  $^{89}\text{Y}$  in the Copper-Oxide Spin-Chain Compound  $\text{Ca}_{2+x}\text{Y}_{2-x}\text{Cu}_5\text{O}_{10}$ ,” Proceedings of the 2002

International Conference on Metal and Oxide Superconductors, Hsinchu, Taiwan, 2002 (in press).

- K. Mochizuki, J.-H. Choi, T. C. Messina, Y. Ando, K. Nakamura, J. T. Markert, “Extreme Smallness of the Transverse Force on Moving Vortices,” LT23 Proceedings, Japan, 2002 (in press).
- J. Barnett, D. Riley, T. Messina, P. Lysaght, “Wet Etch Enhancement of HfO<sub>2</sub> Films by Implant Processing,” UCPSS-2002, Proceedings of the Sixth International Symposium on Ultra-Clean Silicon Surfaces (Scitec Publications Ltd, Zurich, Switzerland, 2002), special edition of Solid State Phenomena (in press).
- P. S. Lysaght, P. J. Chen, R. Bergmann, T. Messina, R. W. Murto and H. R. Huff, “Experimental Observations of the Thermal Stability of High- $\kappa$  Gate Dielectric Materials on Silicon,” Journal of Non-Crystalline Solids, vol. 303, no. 1, 54-63 (2002).
- M. D. Chabot, T.C. Messina, V. Manicevski, C. W. Miller, J. T. Markert, “Single-Crystal Silicon Triple-Torsional Micro-Oscillators for Use in Magnetic Resonance Force Microscopy,” Proceedings of SPIE, San Jose, CA, USA, October 2001.
- J. T. Markert, T. C. Messina, B. Dam, J. Huijbregste, J. Rector, R. Griessen, “Observation of Step-Flow Growth in Laser-Ablated thin films of the T'-Phase compound Pr<sub>2</sub>CuO<sub>4</sub>,” Physica C, 341-348, 2355-56 (2000).

- J. T. Markert, T. C. Messina, B. Dam, J. Huijbregste, J. H. Rector, R. Griessen, “Laser-Ablated Thin Films of Infinite-Layer Compounds and Related Materials,” Proceedings of SPIE, Orlando, FL, USA, 24-28 April 2000, p.141.
- T. Ono, G. A. Rozgonyi, C. Au, T. C. Messina, R. Goodall, H. R. Huff, “Oxygen Precipitation Behavior in 300mm Polished Czochralski Silicon Wafers,” J. Electrochem. Soc. 146, 3807 (1999).
- H. R. Huff, D. McCormack Jr., C. Au, T. C. Messina, K. Chan, R. Goodall, “Current Status of 200mm and 300mm Silicon Wafers,” Proceedings of the Intl. Solid State Devices and Materials (ISSDM '97), Japan, p. 456 and Conference Abstracts p.575, (1997) also published in Jpn J. Appl Phys, 37, (1998) Pt.1, No.3B.
- C. Au, T. C. Messina, R. Goodall, H. R. Huff, “Characterization of 300mm Polished Silicon Wafers,” Proceedings of the 8th International Symposium on Silicon Materials and Technology, v.1, p.641, (1998).
- T. C. Messina, C. Au, S. Shih, Z. Yang, R. Goodall, H. R. Huff, “Current Status of 300mm Wafer Characterization,” Proceedings of the International Mechanical Engineering Conference and Exposition (IMECE '98), p.825, (1998).
- S. Shih, C. Au, Z. Yang, T. C. Messina, R. Goodall, H. R. Huff, “Characterization of 300mm Silicon-Polished and Epi Wafers,” Proceedings of the E-MRS, (1998).

- J. T. Markert, K. Mochizuki, T. C. Messina, B. C. Dunn, A. V. Elliott, “Studies of Infinite-Layer, T'-Phase, and 1-D Ladder Copper-Oxide Compounds,” Proceedings of the NATO Advanced Research Workshop: Physics and Materials Science in High Temperature Superconductivity IV, Strbske Pleso, Slovak Republic, 21-27 July 1996.

## Vita

Troy Christopher Messina was born in Dallas, Texas on August 30, 1973, the son of Darlene Joy Messina and Robert Logan Messina. After graduating from Rockwall High School, Rockwall, Texas, in 1991, he attended the University of Texas at Austin for one year. Then, he relocated to Dallas and attended Richland Community College for a year and a half before returning to UT Austin in January of 1994. He graduated from UT in May, 1996, with a Bachelor of Science degree in physics. In January of 1997, he entered The Graduate School of The University of Texas at Austin, receiving a Master of Arts in physics in December of 1999. Two years after meeting, Troy married Jodi Moore, the woman of his dreams, on April 7, 2001. He has also been a professional drummer/percussionist for Half Street, Speer, the Neal Kassanoff Trio, 3 Penny Opera, Megalo, and Chester.

Permanent address: 1414 Larkwood Drive  
Austin, Texas 78723

This dissertation was typeset with L<sup>A</sup>T<sub>E</sub>X<sup>†</sup> by the author.

---

<sup>†</sup>L<sup>A</sup>T<sub>E</sub>X is a document preparation system developed by Leslie Lamport as a special version of Donald Knuth's T<sub>E</sub>X Program.